

REPORT DOCUMENTATION PAGE

OMB No. 0704-0188

Public reporting burden for this collection of information is estimated to average 1 hour per response, including the time for reviewing instructions, searching existing data sources, gathering and maintaining the data needed, and completing and reviewing the collection of information. Send comments regarding this burden estimate or any other aspect of this collection of information, including suggestions for reducing this burden, to Washington Headquarters Services, Directorate for Information Operations and Reports, 1215 Jefferson Davis Highway, Suite 1204, Arlington, VA 22202-4302, and to the Office of Management and Budget, Paperwork Reduction Project (0704-0188), Washington, DC 20503.

1. AGENCY USE ONLY (Leave blank)		2. REPORT DATE 1 AUGUST 1995		3. REPORT TYPE AND DATES COVERED FINAL 10/1/90 - 9/30/94	
4. TITLE AND SUBTITLE Selected Topics in Coastal and Ocean Technology				5. FUNDING NUMBERS N00014-89J-117	
6. AUTHOR(S) SCOTT A. JENKINS					
7. PERFORMING ORGANIZATION NAME(S) AND ADDRESS(ES) Scripps Institution of Oceanography University of California, San Diego La Jolla, CA 92093-0209				8. PERFORMING ORGANIZATION REPORT NUMBER	
9. SPONSORING/MONITORING AGENCY NAME(S) AND ADDRESS(ES) Office of Naval Research, Code 1121-OT Department of the Navy 800 North Quincy Arlington, VA 22217-5500				10. SPONSORING/MONITORING AGENCY REPORT NUMBER	
11. SUPPLEMENTARY NOTES					
12a. DISTRIBUTION/AVAILABILITY STATEMENT NO LIMITATION					
DTIC SELECTED AUG 29 1995 G DISTRIBUTION STATEMENT A Approved for public release; Distribution Unlimited					
13. ABSTRACT (Maximum 200 words) This final report details research in three major areas: 1) sedimentation control in harbors and waterways, 2) wave structure interaction for a novel tetrahedron sandbag structural concept and 3) tactical oceanography involving development of an optimum glide theory for low speed submarine operations. The sedimentation control research focused on understanding the mechanics of bed shear strength and explored new methods to elevate the bottom shear stress to induce erosion of the bed and prevent deposition. The bed shear strength was found to be monotonic functions of concentration, organic content and salinity. Means for enhancing the shear stress on the bed were studied in both a laboratory flume and in field installations. Both active and passive measures were evaluated. Active measures for enhancing bed shear stress included arrays of bottom mounted jets powered by a centrally located pump and ducted propellers powered by remote hydraulic power supplies. Passive measures invoked arrays of near bottom moored wings whose vortex wakes in tidal flow eroded and resuspended bed sediments. The wave structure interaction research involved development of a tactical break water concept constructed of tetrahedron sandbags filled <i>in situ</i> by pumping sand slurries into the bags using the available sea floor sediments. The bags were not placed individually, but dropped to the sea floor to form talus piles. Arrangements of talus piles in parallel and V-shaped bars were developed to produce Bragg scattering patterns that could be made to either constructively or destructively interfere with incoming waves. Constructive interference patterns were studied as a means for focusing wave energy on energy collection devices. The tactical oceanography effort resulted from participation in Navy sponsored tactical oceanography symposium and workshops, and produced a theory for passive gliding of submarines using lift from sail and stern planes.					
14. SUBJECT TERMS DTIC QUALITY INSPECTED 5				15. NUMBER OF PAGES 4 + Appendices	
				16. PRICE CODE	
17. SECURITY CLASSIFICATION OF REPORT Unclassified	18. SECURITY CLASSIFICATION OF THIS PAGE Unclassified	19. SECURITY CLASSIFICATION OF ABSTRACT Unclassified	20. LIMITATION OF ABSTRACT SAR		

FINAL REPORT: SELECTED TOPICS IN COASTAL AND OCEAN TECHNOLOGY

GRANT # N00014-89J-117

by

SCOTT A. JENKINS

This report covers work in three distinct areas of research: 1) sedimentation control, 2) wave-structure interaction and 3) tactical oceanography. These will be considered separately below.

I. SEDIMENTATION CONTROL

Dredging of Navy harbors represents an escalating cost of ownership, 0 (\$25 million/year), due to environmental restrictions imposed by the NEPA Act and the dwindling dredge spoils pond capabilities of remaining naval facilities. This work sought to develop alternative measures to dredging that would prevent or control sedimentation. Both passive and active measures were studied. The mechanics of either approach involve elevating fluid stresses on the bed above the ambient levels of the natural circulation systems. Elevated shear stresses are shown in Appendices A and B to cause resuspension of the unconsolidated bed and erosion of the consolidated bed.

A) Passive Methods

Shear stresses are found to become elevated passively in tidal flow by the vortex wake of a wing in ground effect with the bed. In Appendix A, a theory and companion experiment are given which describe the resuspension of fine sediments by the action of wings moored near the bottom of an estuary. Calculations by matched inner and outer image expansions indicate that the vortex system of a wing can exert two distinct effects on estuarial sedimentation: (1) it can elevate the shear stresses in the neighborhood of the wing by a sufficient amount to induce erosion of partially consolidated layers of the bottom; and, (2) it can promote vertical transport to either enhance or inhibit downstream deposition. Deposition in the wake trail is found to be dependent upon the direction of the lift force generated by the wing. Wings which produce a downward lift force deplete the region adjacent to the bottom of suspended sediment and thereby diminish downstream deposition. Conversely, wings generating an upward lift force increase the density of suspended sediment near the bottom, thus increasing the rate of downstream deposition. Density measurements behind prototype wings are consistent with these theoretical expectations. Short term changes in bottom contours are in general agreement with predicted erosion in the inner domain, and with diminished accretion in the outer domain.

Short term wing induced perturbations to the bottom appear to be qualitatively explained by entrainment and diminished deposition in the far wake

and by erosion in the near wake. Wings which generate a downward lift force induce erosion in both the near and far wakes. Wings which generate an upward lift force give rise to erosion in the near wake followed by accretion in the far wake.

Long term wing induced perturbations to the bottom are qualitatively explicable only in terms of erosion.

Both erosion and entrainment are maximized by maximizing wing section lift coefficients while in ground effect at low wing Reynolds numbers.

There exists no unique selection of mooring elevation and wing aspect ratio which simultaneously maximizes erosion and minimizes downstream deposition. Erosion is maximized by maximizing wing aspect ratio for a mooring elevation, b , equal to one quarter the wings semi span, S . Deposition is minimized by minimizing wing aspect ratio with $b = 0.8S$.

Wings which generate a downward lift force are more effective in causing local erosion and retarding downstream deposition than wings generating an upward lift force. Because either effect is limited to a wake trail whose cross-stream dimension is of the order of a wing span, large areas of channel bottom will require mass arrays of wings with overlapping wakes (like a flock of birds), in order to control shoaling.

B) Active Methods

The research also considered the intervention of Man-made horsepower to elevate bottom shear stresses to induce resuspension and erosion. The results in Appendix B indicate that deposition of fine grain sediments may be controlled through the semi-diurnal application of hydrostatic jets producing applied shear stresses in excess of the cohesive yield stress of the fluid mud layer. This may be accomplished by either of two means: (1) application of high velocity jets or (2) application of large diameter jets. By either approach the effect of controlling deposition through jet entrainment in the far field is maximized by maximizing the total jet flow rate. This suggests that the total eddy momentum content of the jet discharge is progressively diluted with increasing distance from the jet discharge point. At some maximum range, the eddy momentum of the jet discharge is diluted to such an extent that it is incapable of entraining sediment from the fluid mud layer across the lutocline interface. The unexpected persistence of this entrainment in the far field of low salinity jets also suggests that the jet salinity may exert a modifying effect on the cohesive yield stress of the fluid mud, rendering it more susceptible to eddy transport across the lutocline. These results are directly applicable to the problem of bottom resuspensions by ship thrust wakes.

One of the new technologies to result from this work was a novel method for generating a near bottom jet flow. This new method is the turbine-chimney and is described in the U.S. Patent contained in Appendix C. The turbine chimney consists of a propeller mounted inside a vertically oriented 90° elbow with a horizontal discharge at the bottom. This configuration protects the propeller from bottom debris or slumping mud bands, as commonly found beneath piers and docks. The elbow may be hinged to a frame and articulated with a



Dist	Avail and/or Special
A-1	

hydraulic ram to allow the jet to scan through 180° arcs, thereby increasing the area of influence of the jet discharge. Whereas the pump based systems generally produce a high velocity low flow rate jet through a small convergent nozzle, the propeller based system produces a relatively low velocity jet at a very high flow rate.

Another concept to emerge from this work is the crater-sink fluidization dam bypassing concept described in Appendix D. This system is intended to recover sediments trapped behind inland dams, and to bypass them to eroding sections of coastline.

II. WAVE STRUCTURE INTERACTION:

THE TETRAHEDRON SANDBAG BREAKWATER

This study produced a new approach to development of mobile breakwater systems and is detailed in Appendix E. Rather than floating structures, a gravity inertia structure is developed which rests on a broad footprint on the sea floor. Hence no connectors or moorings are required. The structure is modular, consisting of a pair of staggered piles of tetrahedron sandbags arranged obliquely to the incident waves as shown in Appendix E. Each tetrahedron in the array consists of a triangular shaped sandbag constructed of geotextile fabric and filled with sand.

During transport to the LOTS site the sandbags are readily stored aboard LOTS ships in a flat, folded and unfilled condition. Hence many such sandbags can be stored on a single LOTS ship without the need for occupying significant shipboard space. Upon arrival at the LOTS site and prior to unloading of supplies and material, each LOTS ship can deploy its own array of protective tetrahedron sandbag arrays using available shipboard firepumps and crane support. This is accomplished by attaching a small jet pump to pump sand slurries from under the ship into each sandbag. The tetrahedron sandbags are positioned around the anchorage using crane support aboard the LOTS ships. The geotextile fabric construction of each tetrahedron sandbag is strong, compliant and allows the water to ventilate out of the bag during filling with the sand slurry. If necessary, the bag might later be emptied by means of a Velcro sealed outlet door near the base of the tetrahedron sandbag, or by crane and clamshell.

The theory of attenuating incident waves by means of an array of tetrahedron sandbags is based on the principle of partial Bragg reflection, or Bragg scattering, see Appendix E. Whereas a contiguous saw-toothed geometry can achieve complete quarter wavelength cancellation, the tetrahedron array has a certain amount of leakage between adjacent corner reflectors. However, it was found that this leakage can be minimized for particular dimensioning and spacing of the tetrahedrons based on the incident frequency and direction. This can be readily shown for monochromatic waves using the classical expansion in solid harmonics for multiple scattering centers (in this case tetrahedrons). Such monochromatic multiple scattering solutions are not new for plane, shallow water waves, except for the triangular geometry which apparently does not yet have a published calculation.

The new aspect of this theoretical approach for the multiple scattering problem is to include the effects of wave groups incident on finite arrays. This approach was based on a multiple scales perturbation method in which the predominant carrier swell waves are scaled in

terms of fast variables while their groups are scaled in terms of slow variables which are order $1/\epsilon$ times those of the fast variables, where ϵ is the wave steepness. This scheme yields analytical solutions which differ from those of the monochromatic case by the presence of a second order low frequency oscillation among the elements of the tetrahedron array. Because the modulations induced by this second order low frequency oscillation are locked with the wave groups and propagate at the speed of the group velocity, they appear seaward of the array as locked long waves in the reflected wave group, but not in the radiated waves shoreward of the array. Inside the array these locked long waves introduce a discontinuity which forces a second order free long wave propagating at a speed of \sqrt{gh} . The free long waves appear shoreward of the array and may be resonant in a low frequency range which can be exploited for wave energy collection as described in Appendix E.

The same discontinuities arising from the locked long waves among the tetrahedrons within the array will also effect the diffraction around the flanks of the array. This diffraction is controlled by a second order evanescent mode decaying rapidly with distance away from the array. The evanescent mode leads to various patterns of shadows and bright spots on the flanks of the array depending upon the direction of the incident wave groups.

III. TACTICAL OCEANOGRAPHY: DEVELOPMENT OF THE GLIDING SUBMARINE TACTIC

This effort was an offshoot of participation in the Tactical Oceanography Symposium, 1990, 1991 sponsored by OP-96. The results were outlined in a report to COMSUBDEVRON-12 contained in Appendix F, and were published in unclassified form in the reviewed literature as contained in Appendix G. The basic concept is one of a means for submarines to make low speed translation between any two points *without turning the screw*. It is believed that this would be possible by ballasting in a slightly positive or negative state and then gliding on sail-plane lift in the manner of an airplane or bird. The notion here is that passive acoustic detectability can be reduced by trading the continual emittance of hydrodynamic noise from propeller swirl for an occasional "burp" of ballast pump noise as the buoyancy is alternately adjusted between positive and negative states during a dolphin style glide path. Tactical advantages would likely arise following high speed transits to some patrol area, whence low speed dolphin glides could be invoked to quietly slip away from suspected contact.

**APPENDIX A: RESUSPENSIONS OF ESTUARIAL FINE
SEDIMENTS BY TETHERED WINGS**

by

SCOTT A JENKINS & JOSEPH WASYL

Resuspension of Estuarial Fine Sediments by Tethered Wings

Scott A. Jenkins and Joseph Wasyl

Scripps Institution of
Oceanography, A-009
La Jolla, CA 92093, USA



ABSTRACT

JENKINS, S.A. and WASYL, J., 1990. Resuspension of estuarial fine sediments by tethered wings. *Journal of Coastal Research*, 6(4), 961-980. Fort Lauderdale (Florida). ISSN 0749-0208.

A theory and companion experiment are given which describe the resuspension of fine sediments by the action of wings moored near the bottom of an estuary. Calculations by matched inner and outer image expansions indicate that the vortex system of a wing can exert two distinct effects on estuarial sedimentation: (1) it can elevate the shear stresses in the neighborhood of the wing by a sufficient amount to induce erosion of partially consolidated layers of the bottom; and, (2) it can promote vertical transport to either enhance or inhibit downstream deposition. Deposition in the wake trail is found to be dependent upon the direction of the lift force generated by the wing. Wings which produce a downward lift force deplete the region adjacent to the bottom of suspended sediment and thereby diminish downstream deposition. Conversely, wings generating an upward lift force increase the density of suspended sediment near the bottom, thus increasing the rate of downstream deposition. Optimal wing configurations are formulated which maximize erosion and minimize deposition. Density measurements behind prototype wings are consistent with these theoretical expectations. Short term changes in bottom contours are in general agreement with predicted erosion in the inner domain, and with diminished accretion in the outer domain.

ADDITIONAL INDEX WORDS: Cohesive sediment, silt, clay, flocculation, erosion, deposition, consolidation, accretion, fluid mud, entrainment, lutocline, Bingham fluid, diffusivity, scour, lifting line, image method, circulation, horseshoe-vortices.

INTRODUCTION

The phenomenon of current scour due to vortical wakes shed from the support piles of bridges and other waterfront structures is well known, (COLLINS, 1980, and CHIEW and MELVILLE, 1987). Transport of suspended particles by near-wake vortices behind bluff bodies has been found to be especially vigorous in air, (MacLENNAN and VINCENT, 1982). Vortices from boat traffic have been observed to scour and resuspend fine sediments, (GARRAD and HEY, 1987). The work herein begins with the hypothesis that the vortex system of a moored wing might perturb sediment transport and cause similar scour features in the muddy bottom under steady or slowly varying estuarine flow. If wing induced scour is found to be sufficiently vigorous, it could emerge as a new concept among the paucity of passive technologies to maintain dredged harbors and waterways.

Presently, active technologies amass a \$2 billion worldwide annual maintenance dredging bill, (MARINE BOARD, 1983). Those costs are largely driven by dredge spoils disposal problems which would otherwise not exist with passive methods.

The wing vortex system appears to be especially well suited to influence sediment transport because it imparts a net vertical advection to the flow in reaction to the lift force, (LANCHESTER, 1908, PRANDTL and BETZ, 1927, and PRANDTL, 1931). This vertical advection (induced velocity) might be employed to either reduce or increase the net settling rates of silts and clays, depending upon the direction of the lift force, (JENKINS and SPARKS, 1985, and JENKINS, 1987). Because the preponderance of transport of these fine-grained sediments occurs near the bottom, (EINSTEIN and KRONE, 1961, and MEHTA, *et al.*, 1989), we are particularly interested in the case of a wing

in proximity to the immobile bed, *i.e.*, in ground effect, (LAGALLY, 1929, PRESMAK, 1977, and McCORMICK, 1979). Ground effect is generally considered to be the condition in which the wing is within one semi-span length of a solid plane boundary.

We seek analytic solutions to the wing induced perturbations on sediment transport and the bed response so that cause and effect relations might be readily established. Therefore it shall be necessary to make a number of idealizations with respect to both the sediment transport physics as well as the flow field produced by the wing. We employ a Fickian-based advection-diffusion transport model to provide a deterministic approach with sufficient kinematic detail to allow analytic progress on the problem at hand. These are the most widely adopted fine-sediment transport models in the published literature and have been validated by both laboratory data, (APMAN and RUMER, 1970), and field data, (KERSSENS *et al.*, 1979). They have been employed to account for transport over eroding or accreting beds, (LAMBERMONT and LEBON, 1978, and CHENG, 1985), and for the vertical and streamwise variability in transport, (MEI, 1969). The latter was constrained by the assumption that the settling velocity of the sediment, w_s , is of the same order as the mean flow velocity, u_m . This rather unrealistic assumption for the case of fine-sediment transport has been circumvented herein by coordinate stretching based on the strength of the wing perturbation.

With regard to specifying the flow field around a wing moored near an estuarine bottom, there are two major difficulties: (1) viscosity; and (2) density stratification due to the abundance of suspended sediment near the bottom. Unfortunately, the recent wing theories which explicitly account for the effects of either viscosity or density stratification are numerical, *e.g.*, MOORE (1974), MATTEI and SANTORO (1974), STAUFENBIEL and KLEINERDAM (1980), PULLIN and PHILLIPS (1981) or SAFFMAN (1972), HILL (1975) and GREEN (1985), respectively. Analytic solutions for the flow field induced by a wing of finite span present one of the most intractable problems in aerodynamic theory, (VAN DYKE, 1975). Therefore we shall neglect stratification and approximate the local flow field as an inviscid singular perturbation in the wing aspect ratio,

A_w , after VAN DYKE (1964). This is based on the premise that the wing circulation is large compared to ambient levels and that the rotational and irrotational parts of the flow do not interact. Difficulties associated with the no-slip condition at the bottom do not explicitly arise herein because the sediment-transport equations developed in the following sections rely on inviscid wing-theory only to specify the vertical component of the flow field. Details of the trailing vortex roll-up in the near wake of the wing provided by the analytic results of BATCHELOR (1964), SQUIRE (1965), GOVINDARAJU and SAFFMAN (1972), SAFFMAN (1973) and PHILLIPS (1981) do not appear at the order of approximation taken in the formulation of the sediment-transport equations below.

Formulation

Consider a fluid of density, ρ_f , transporting a suspension of uniform particles, each with a settling velocity relative to the fluid, w_s , and a solid density, $\rho_s = 2.65 \text{ g cm}^{-3}$. The density of the fluid-sediment mixture, ρ_m , may be written:

$$\rho_m = \rho_s N + (1-N)\rho_f \quad (1)$$

where N is the volume concentration equal to the volume of sediment per volume of the fluid-sediment mixture. The density of the sediment component of this mixture, ρ_s , is sometimes referred to as the excess or bulk density and is defined:

$$\rho = \rho_s N \quad (2)$$

Assume a uniform channel flow with a characteristic velocity u_m which varies slowly at angular frequency Ω_m over a flat cohesive surface on the plane $z = 0$, see Figure 1. At or below $z = 0$, the fluid-sediment mixture exhibits a non-zero cohesive yield stress, τ_c , and behaves as a viscoplastic. Above $z = 0$, the cohesive yield stress vanishes and the fluid-sediment mixture behaves as a fluid, *i.e.*, unable to support shear stress at equilibrium. The sediment component density at $z = 0$ where the mixture first begins to exhibit a cohesive yield stress is, $\rho = \rho_c$.

The upper regions of the fluid, $z > h$, are relatively deficient of suspended sediment and may be characterized by some small ambient value, $\rho = \rho_a$. Because of settling under the

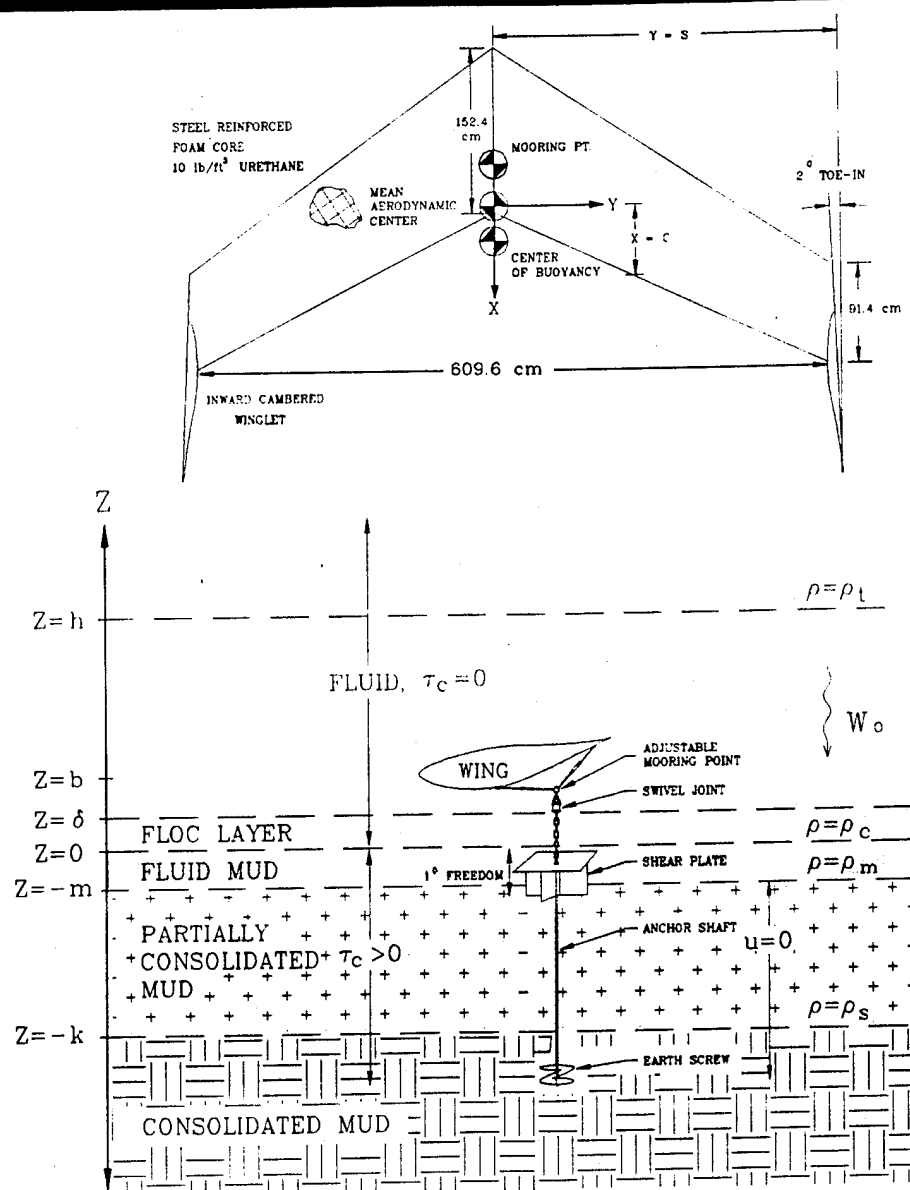


Figure 1. Conceptual diagram of the fluid bed interface with the wing and its mooring details.

influence of gravity, the abundance of suspended sediment begins to increase below $z = \delta$, forming a non-cohesive floc layer as shown in Figure 1, (MEHTA and PARTHENIADES, 1975, and KRONE, 1978). The surface $z = 0$ may thus be considered a "lutocline", (DYER, 1985, and MEHTA, 1989).

Immediately below the lutocline, there is a

rather thin layer of cohesive fluid mud between, $0 \leq z < -m$, which has a non-zero velocity, (KIRBY and PARKER, 1974, PARKER and KIRBY, 1982 and NICHOLS, 1985). Thus the lutocline at $z = 0$ between the fluid and the viscoplastic material is not a no-slip boundary. The dynamics of the fluid mud layer are still poorly understood when subjected to a moving

fluid. For analytic purposes, we shall assume that the lutocline at $z = 0$ is a stress free boundary much like a free surface, with the shear stresses resulting from the fluid motion appearing in the stress field of the fluid mud layer. This assumption relieves the wing induced velocity field on the fluid side of the lutocline interface from having to satisfy the no-slip condition at $z = 0$. The no-slip boundary thus appears at $z = -m$ where the immobile, partially consolidated bottom begins.

Below the fluid mud layer, $z < -m$, the sediment is at rest and there is a progressive build up in sediment component density to some ultimate saturation value, $\rho = \rho_s$. This is due to consolidation and compaction under the weight of the overburden which proceeds at a rate characterized by $\rho_s K_s g$, where g is the acceleration of gravity and K_s is the sedimentation coefficient in seconds, (FUJITA, 1962). The portion of the cohesive bottom below the fluid mud layer for which $\rho_c \leq \rho < \rho_s$ shall be referred to as partially consolidated mud, while the fully consolidated mud in Figure 1 represents the oldest deposition which has reached final saturation density $\rho = \rho_s$.

Now superimpose a wing on the river flow at a distance $z = b$ above the lutocline. Take the wing semi-span to be S . Assume the wing to be in ground effect so that $b < S$. Let the mean semi-cord be c so that the wing aspect ratio is $A_w = S/c$. We shall prescribe the sediment transport and the wing induced velocity field in an Eulerian frame with respect to Cartesian coordinates (x, y, z) . The origin of this system is located at the intersection between the lutocline plane and a vertical projection from the mean aerodynamic center of the wing, see Figure 1. The axis $o-z$ shall be positive vertically upward; the axis $o-x$ is positive in the direction of the river channel flow; while the axis $o-y$ is transverse to the mean channel flow in a right hand system.

With the problem posed in this way, the only horizontal variability will be that imposed by the wing over length scales the size of a wing semi-span. On the other hand, the density field is structured vertically, with strong variability near the lutocline over length scales of the order of the floc layer thickness. Therefore, we prescribe the following scalings for the dimensional variables:

$$\begin{aligned} x &= \hat{x}S \\ y &= \hat{y}S \\ z &= \hat{z}\delta = \hat{z}S/A_F \\ t &= \hat{t}/\Omega_0 \\ (u, v, w) &= (\hat{u}, \hat{v}, \hat{w})u_0 \\ \rho &= \rho_s \hat{\rho} \end{aligned} \quad (3)$$

where carets denote dimensionless variables and $A_F = S/\delta$ is the density field aspect ratio.

Sediment transport by the fluid velocity field, (u, v, w) , can then be expressed by the non-dimensional Fickian-based advection-diffusion equation as follows:

$$\begin{aligned} \frac{\Omega_0 \delta^2}{\epsilon} \frac{\partial \hat{\rho}}{\partial \hat{t}} &= \frac{\partial^2 \hat{\rho}}{\partial \hat{z}^2} - R_F \left[\left(\hat{w} + \frac{\omega_0}{u_0} \right) \frac{\partial \hat{\rho}}{\partial \hat{z}} + \hat{\rho} \frac{\partial \hat{w}}{\partial \hat{z}} \right] \\ &- \frac{R_F}{A_F} \left(\hat{\rho} \frac{\partial \hat{u}}{\partial \hat{x}} + \hat{u} \frac{\partial \hat{\rho}}{\partial \hat{x}} + \hat{\rho} \frac{\partial \hat{v}}{\partial \hat{y}} + \hat{v} \frac{\partial \hat{\rho}}{\partial \hat{y}} \right) \\ &+ \frac{1}{A_F^2} \left(\frac{\partial^2 \hat{\rho}}{\partial \hat{x}^2} + \frac{\partial^2 \hat{\rho}}{\partial \hat{y}^2} \right) \end{aligned} \quad (4)$$

where $R_F = u_0 \delta / \epsilon$ is the mass flux Reynolds number equal to a ratio of advective to diffusive mass fluxes and ϵ is the mass diffusivity. Under the prototype conditions typical of the lower depths of estuaries along the U.S. west coast as encountered in Section 7, we take:

$$\begin{aligned} u_0 &= O(10 \text{ cm/sec}) \\ \omega_0 &= O(10^{-2} \text{ cm/sec}) \\ \Omega &= O(10^{-4} \text{ sec}^{-1}) \\ h &= O(10^2 \text{ cm} - 10^3 \text{ cm}) \\ \delta &= O(10 \text{ cm}) \\ \epsilon &= O(1 \text{ cm}^2/\text{sec}) \\ c &\gg O(\delta) \end{aligned} \quad (5)$$

The final order of magnitude argument in (5) sets a minimum size restriction on the wing. This is necessary to avert Hele-Shaw flow, (WERLE, 1973 and McMASTERS, 1974) and to assure that the wing circulation is large compared to that of the ambient near-bottom flow.

OUTER SOLUTION

In the outer domain, $\hat{x} \gg O(1)$, the lowest order solution follows from (4) when the channel flow is subjected to an $O(1/A_w)$ perturbation from a wing at a small angle of attack β . The perturbation from a wing in ground effect at a distance $z = b$ above a plane surface was first represented by an image pair of lifting lines by

BETZ (1912). The velocity potential of this familiar vortex system is written in terms of outer variables (3) as:

$$\begin{aligned} \phi = \hat{x} + \beta \left(\frac{\hat{z}}{A_F} - \frac{b}{S} \right) &+ \frac{\beta f(x)}{2A_w} \int_{-1}^1 \frac{\left(\frac{\hat{z}}{A_F} - \frac{b}{S} \right) T(\zeta)}{\left(\frac{\hat{z}}{A_F} - \frac{b}{S} \right)^2 + (\hat{y} - \zeta)^2} \\ &\left\{ 1 + \frac{\hat{x}}{\sqrt{\hat{x}^2 + \left(\frac{\hat{z}}{A_F} - \frac{b}{S} \right)^2 + (\hat{y} - \zeta)^2}} \right\} d\zeta \\ &- \beta \left(\frac{\hat{z}}{A_F} + \frac{b}{S} \right) \\ &- \frac{\beta f(x)}{2A_w} \int_{-1}^1 \frac{\left(\frac{\hat{z}}{A_F} + \frac{b}{S} \right) T(\zeta)}{\left(\frac{\hat{z}}{A_F} + \frac{b}{S} \right)^2 + (\hat{y} - \zeta)^2} \\ &\left\{ 1 + \frac{\hat{x}}{\sqrt{\hat{x}^2 + \left(\frac{\hat{z}}{A_F} + \frac{b}{S} \right)^2 + (\hat{y} - \zeta)^2}} \right\} d\zeta \end{aligned} \quad (6)$$

where $T(\zeta)$ is a unit function defining the spanwise distribution of circulation; $f(x)$ is a unit function defining the rate of downstream decay of circulation in the trailing vortices and ζ is a dummy variable. Terms containing $(z+b)$ correspond to the image vortex system at $z = -b$. We have adopted herein the convention that the lift force due to the real vortex acts upward in the positive z direction for $\beta > 0$.

Equations (5) and (6) require a large, high aspect ratio wing, whence $A_F \gg A_w \gg 1$. Consequently, the advection-diffusion equation (4) may be written at lowest order:

$$\frac{\partial \hat{p}^{(0)}}{\partial \hat{z}^2} - \frac{R_F}{A_w} \left(\hat{w}^{(1)} \frac{\partial \hat{p}^{(0)}}{\partial \hat{z}} + \hat{p}^{(0)} \frac{\partial \hat{w}^{(1)}}{\partial \hat{z}} \right) = 0 \quad (7)$$

where $\hat{w}^{(1)} = A_F \partial \phi / \partial \hat{z}$ is the $O(1/A_w)$ induced velocity. Equation (7) is subject to boundary conditions which require:

$$\hat{p}^{(0)} = 1 \text{ at } \hat{z} = 0 \quad (8)$$

$$\hat{p}^{(0)} = \rho_i / \rho_c \text{ at } \hat{z} = h/\delta \quad (9)$$

With (6) a solution to equation (7) can be obtained by successive integrations, evaluating

the integration constants according to the boundary conditions (8) and (9) to yield the following result in dimensional form:

$$\rho = \rho_c \exp \left\{ \frac{2}{\epsilon A_w} [I_1(x, y, z) - I_1(0)] \right. \\ \left. + \frac{z}{h} I_1(0) - \frac{z}{h} I_1(h) + \frac{z}{h} \log \frac{\rho_i}{\rho_c} \right\} \quad (10)$$

where $I_1(0) = I_1(x, y, z = 0)$; $I_1(h) = I_1(x, y, z = h)$ and (see equation 11).

Here Γ_0 is the circulation of the bound vortex of the wing and Γ is the circulation of the trailing vortices such that,

$$\Gamma_0 = u_0 C_l c \quad (12)$$

$$\Gamma = \Gamma_0 f(x) \quad (13)$$

C_l in equation (12) is the lift coefficient which shall be positive for a wing above the bottom which generates lift upward in the positive z -direction. This case shall be referred to herein as a "downwashing" wing. When $C_l < 0$, the lift is directed downward toward the bottom and these shall be referred to as "upwashing" wings. The decay rate, $f(x)$, for the circulation of the trailing vortices in (13) is due to the ground effect calculations of PEACE and RILEY (1983) for the case of a stress free boundary at $z = 0$. Their results by numerical integration give:

$$\begin{aligned} f(x) = 1 - \int_0^x \left\{ u^{(0)} + \left(\frac{x C_l \sigma}{u_0 S^2} \right)^{1/2} u^{(1)} \right. \\ \left. + \left(\frac{x C_l \sigma}{u_0 S^2} \right) \left(u^{(2)} + \frac{\partial^2 u^{(0)}}{\partial x^2} \right) \right\} dx \\ = 1 + (5.410 \times 10^{-3}) \left(\frac{x C_l}{A_w S} \right)^2 \\ - (6.670 \times 10^{-4}) \left(\frac{x C_l}{A_w S} \right)^3 \\ + (1.173 \times 10^{-5}) \left(\frac{x C_l}{A_w S} \right)^4 \\ - (9.241 \times 10^{-8}) \left(\frac{x C_l}{A_w S} \right)^5 \\ + (2.729 \times 10^{-10}) \left(\frac{x C_l}{A_w S} \right)^6 \end{aligned} \quad (14)$$

where σ is the diffusivity of momentum.

INNER SOLUTION

The outer solution (10) develops singular behavior as $\hat{x} \rightarrow 0$ due to the line singularity of

$$\begin{aligned}
I_1(x,y,z) = & \frac{\Gamma_0}{4\pi} \left\{ \tan^{-1} \left[\frac{(z-b)(y+S)}{x\sqrt{x^2 + (y+S)^2 + (z-b)^2}} \right] - \tan^{-1} \left[\frac{(z+b)(y+S)}{x\sqrt{x^2 + (y+S)^2 + (z+b)^2}} \right] \right\} \\
& - \frac{\Gamma_0}{4\pi} \left\{ \tan^{-1} \left[\frac{(z+b)(y-S)}{x\sqrt{x^2 + (y-S)^2 + (z+b)^2}} \right] - \tan^{-1} \left[\frac{(z-b)(y-S)}{x\sqrt{x^2 + (y-S)^2 + (z-b)^2}} \right] \right\} \\
& - \frac{\Gamma}{4\pi} \left\{ \tan^{-1} \left[\frac{(z+b)}{(y-S)} \right] - \tan^{-1} \left[\frac{(z-b)}{(y-S)} \right] \right\} \\
& - \frac{\Gamma}{4\pi} \left\{ \tan^{-1} \left[\frac{x(z+b)}{(y-S)\sqrt{x^2 + (y-S)^2 + (z+b)^2}} \right] - \tan^{-1} \left[\frac{x(z-b)}{(y-S)\sqrt{x^2 + (y-S)^2 + (z-b)^2}} \right] \right\} \\
& - \frac{\Gamma}{4\pi} \left\{ \tan^{-1} \left[\frac{(z-b)}{(y+S)} \right] - \tan^{-1} \left[\frac{(z+b)}{(y+S)} \right] \right\} \\
& - \frac{\Gamma}{4\pi} \left\{ \tan^{-1} \left[\frac{x(z-b)}{(y+S)\sqrt{x^2 + (y+S)^2 + (z-b)^2}} \right] \right\} + \frac{\Gamma}{4\pi} \left\{ \tan^{-1} \left[\frac{x(z+b)}{(y+S)\sqrt{x^2 + (y+S)^2 + (z+b)^2}} \right] \right\}
\end{aligned}$$

Equation 11.

the bound vortex which approximates the wing itself in the outer domain. This non-uniformity in the lifting line approximation is well known, (VAN DYKE, 1964), and can be remedied as in aerodynamic theory by introducing magnified dimensionless inner variables (X, Y, Z) such that:

$$\begin{aligned}
\hat{X} &= A_w \hat{x} \\
\hat{Y} &= \hat{y} \\
\hat{Z} &= A_w \hat{z}
\end{aligned} \quad (15)$$

The local flow field in terms of (15) then reduces to plane flow past an image pair of flat plates at angle of attack β as defined by equation 16, where $\hat{\phi} = A_w^{-1}\phi$ and I_m is the imaginary part operator. The non-dimensional form of the advection-diffusion equation in the inner domain can now be expressed in terms of inner variables as:

$$\begin{aligned}
0 = & \frac{\partial^2 \hat{\rho}}{\partial \hat{Z}^2} - \frac{R_F}{A_w} \left[\left(\hat{W} + \frac{\omega_0}{u_0} \right) \frac{\partial \hat{\rho}}{\partial \hat{Z}} + \hat{\rho} \frac{\partial \hat{W}}{\partial \hat{Z}} \right] \\
& - \frac{R_F}{A_w A_F} \left(\hat{U} \frac{\partial \hat{\rho}}{\partial \hat{X}} + \hat{\rho} \frac{\partial \hat{U}}{\partial \hat{X}} \right) \\
& - \frac{R_F}{A_w^2 A_F} \left(\hat{V} \frac{\partial \hat{\rho}}{\partial \hat{Y}} + \hat{\rho} \frac{\partial \hat{V}}{\partial \hat{Y}} \right) \\
& - \frac{1}{A_F^2} \frac{\partial^2 \hat{\rho}}{\partial \hat{X}^2} + \frac{1}{A_F^2 A_w^2} \frac{\partial^2 \hat{\rho}}{\partial \hat{Y}^2}
\end{aligned} \quad (17)$$

Inserting (16) in (17), the leading order transport equation in the inner domain becomes,

$$\frac{\partial^2 \hat{\rho}^{(0)}}{\partial \hat{Z}^2} - \frac{R_F}{A_w} \left(\hat{W}^{(0)} \frac{\partial \hat{\rho}^{(0)}}{\partial \hat{Z}} + \hat{\rho}^{(0)} \frac{\partial \hat{W}^{(0)}}{\partial \hat{Z}} \right) = 0 \quad (18)$$

where $\hat{W}^{(0)} = A_F/A_w \partial \hat{\phi} / \partial \hat{Z}$ is the $O(1)$ induced velocity. On (18) the following boundary conditions are imposed:

$$\hat{\rho}^{(0)} = 1 @ \hat{Z} = 0 \quad (19)$$

$$\hat{\rho}^{(0)} = \rho_c / \rho_c @ \hat{Z} = A_w h / \delta \quad (20)$$

Upon successive integrations the solution to (18) subject to (19) and (20) is found in dimensional form to be:

$$\begin{aligned}
\rho = \rho_c \exp \left\{ \frac{2}{\epsilon A_w} [I_2(x,y,z) - I_2(0)] \right. \\
\left. + \frac{z}{h} I_2(0) - \frac{z}{h} I_2(h) \right\} + \frac{z}{h} \log \frac{\rho_c}{\rho_c} \quad (21)
\end{aligned}$$

where $I_2(0) = I_2(x,y,z=0)$; $I_2(h) = I_2(x,y,z=h)$ and (see equation 22).

It can be demonstrated at $O(R_F/A_w)$ that the inner solution by (21) and (22) matches asymptotically with the outer solution given by (10) and (11) as $A_w \rightarrow \infty$ in the overlap domain where $\hat{x} \sim O(1)$. Even for relatively small aspect ratios the match is quite good as shown in Figure 2 for the cases of both downwashing and upwashing wings. The match remains satisfactory in as close as $x/S = 2/3$, at relatively high ambient velocities, $u_\infty = 50$ cm/sec.

We find in Figure 3a that the net effect in the

$$\begin{aligned}
\Phi = & \dot{X} \cos \beta + (\sin \beta) \cdot \text{Im} \left\{ \sqrt{\left[\dot{X} + i \left(\frac{\dot{Z}}{A_F} - \frac{b}{c} \right) \right]^2 - T^2(\dot{Y})} \right. \\
& - T(\dot{Y}) \log \left[\dot{X} + i \left(\frac{\dot{Z}}{A_F} - \frac{b}{c} \right) + \sqrt{\left[\dot{X} + i \left(\frac{\dot{Z}}{A_F} - \frac{b}{c} \right) \right]^2 - T^2(\dot{Y})} \right] \Big\} \\
& + \dot{X} \cos(-\beta) + (\sin(-\beta)) \cdot \text{Im} \left\{ \sqrt{\left[\dot{X} + i \left(\frac{\dot{Z}}{A_F} + \frac{b}{c} \right) \right]^2 - T^2(\dot{Y})} \right. \\
& - T(\dot{Y}) \log \left[\dot{X} + i \left(\frac{\dot{Z}}{A_F} + \frac{b}{c} \right) + \sqrt{\left[\dot{X} + i \left(\frac{\dot{Z}}{A_F} + \frac{b}{c} \right) \right]^2 - T^2(\dot{Y})} \right] \Big\}
\end{aligned} \quad (16)$$

Equation 16.

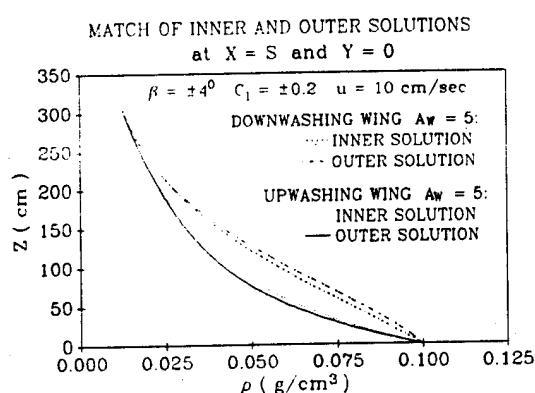


Figure 2. Match of the inner and outer solutions for prototype conditions. Calculations are based on: $\epsilon = 4.951 \text{ cm}^2/\text{sec}$, $\rho_t = 0.0125 \text{ g/cm}^3$, and $\rho_c = 0.10 \text{ g/cm}^3$, and $h = S = 304.8 \text{ cm}$.

wake of an upwashing wing, $(C_b, \beta) < 0$, is to displace suspended sediment upward away from the bottom creating a density inversion layer above the wing. In consequence the density gradient at the lutocline becomes more strongly negative relative to the conditions far downstream. Conversely, the wake of the downwashing wing in Figure 3b is shown to drive the sediment downward, depleting the region above of the floc layer and elevating the suspended concentrations beneath the wing and directly adjacent to the lutocline. This results in an inversion layer under the wing which can reverse the sign of the density gradient at the lutocline. The calculations are for a wing moored 100 cm above the lutocline in a 10 cm/sec ambient cur-

rent. In either case the wing induced density perturbations die out in the outer solution with increasing distance downstream until $x = \infty$, where the density profile is equivalent to the exponential no-wing case. Figure 4 shows cross-stream variations in the wing induced density perturbations that are similar to those found in the stream-wise direction in Figure 3. The cross-stream variability is shown for a tapered wing whose spanwise circulation distribution varies according to VAN DYKE (1964) as:

$$T(y) = \text{Re}\{(1 - y^2/S^2)^{3/2}\} \quad (23)$$

where Re is the real part operator. We find that beyond the wing tips, $|y| > S$, the density profile of the inner solution again approaches the exponential no-wing profile of the undisturbed ambient flow.

EROSION AND DEPOSITION Shoaling of the bottom in a time-averaged sense is the net resultant of two processes, erosion and deposition. Therefore, shoaling can be retarded or prevented by either of two mechanisms: (1) by eroding immobile, partially consolidated mud below $z = -m$, and (2) by reducing or preventing the deposition of new mud above $z = -m$. The latter is accomplished by entraining suspended material from the fluid mud layer before it can become incorporated on the partially consolidated bottom at $z = -m$.

Generally erosion results when an applied stress exceeds the cohesive yield stress, τ_c , of the immobile bed below $z = -m$ (MEHTA, *et al.*, 1989). In our formulation of the bottom interface, this can only result from stress trans-

$$\begin{aligned}
I_2(x,y,z) = & \frac{u_0 \delta A_F}{A_w} \sin \beta \left\{ \left[\frac{x^2}{c^2} - \frac{(z-b)^2}{c^2} - T^2 \right]^2 + \left[\frac{2x(z-b)}{c^2} \right]^2 \right\}^{1/4} \sin \left\{ \tan^{-1} \left[\frac{2x(z-b)}{x^2 - (z-b)^2 - T^2} \right] \right\} \\
& + \frac{u_0 \delta A_F}{A_w} \sin(-\beta) \left\{ \left[\frac{x^2}{c^2} - \frac{(z+b)^2}{c^2} - T^2 \right]^2 + \left[\frac{2x(z+b)}{c^2} \right]^2 \right\}^{1/4} \sin \left\{ \tan^{-1} \left[\frac{2x(z+b)}{x^2 - (z+b)^2 - T^2} \right] \right\} \\
& - \frac{T u_0 \delta A_F}{A_w} \sin \beta \tan^{-1} \left[\left\{ \left[\frac{x^2}{c^2} - \frac{(z-b)^2}{c^2} - T^2 \right]^2 + \left[\frac{2x(z-b)}{c^2} \right]^2 \right\}^{1/4} \right. \\
& \quad \left. \sin \left\{ \frac{1}{2} \tan^{-1} \left[\frac{2x(z-b)}{x^2 - (z-b)^2 - T^2} \right] \right\} + \frac{(z-b)}{c} \right) \Bigg/ \\
& \quad \left(\left\{ \left[\frac{x^2}{c^2} - \frac{(z-b)^2}{c^2} - T^2 \right]^2 + \left[\frac{2x(z-b)}{c^2} \right]^2 \right\}^{1/4} \cos \left\{ \frac{1}{2} \tan^{-1} \left[\frac{2x(z-b)}{x^2 - (z-b)^2 - T^2} \right] \right\} + \frac{x}{c} \right) \\
& - \frac{T u_0 \delta A_F}{A_w} \sin(-\beta) \tan^{-1} \left[\left\{ \left[\frac{x^2}{c^2} - \frac{(z+b)^2}{c^2} - T^2 \right]^2 + \left[\frac{2x(z+b)}{c^2} \right]^2 \right\}^{1/4} \right. \\
& \quad \left. \sin \left\{ \frac{1}{2} \tan^{-1} \left[\frac{2x(z+b)}{x^2 - (z+b)^2 - T^2} \right] \right\} + \frac{(z+b)}{c} \right) \Bigg/ \\
& \quad \left(\left\{ \left[\frac{x^2}{c^2} - \frac{(z+b)^2}{c^2} - T^2 \right]^2 + \left[\frac{2x(z+b)}{c^2} \right]^2 \right\}^{1/4} \cos \left\{ \frac{1}{2} \tan^{-1} \left[\frac{2x(z+b)}{x^2 - (z+b)^2 - T^2} \right] \right\} + \frac{x}{c} \right) \Bigg] \quad (22)
\end{aligned}$$

Equation 22.

fer through the fluid mud layer. The velocity at the top of the fluid mud layer must match the fluid velocity along the stress free boundary at $z = 0$. However at the bottom of the fluid mud layer, $z = -m$, the velocity must vanish, giving rise to shear stresses within the fluid mud. Because the fluid mud is in motion these shear stresses, τ , must already be in excess of the cohesive yield stress of the fluid mud. Under the assumption that the fluid mud behaves as a thin Bingham fluid, (VANONI, 1975, FAAS, 1985, WRIGHT and KRONE, 1987), this excess shear stress, $\tau - \tau_c$, will vary with the wing disturbance as:

$$\tau - \tau_c = \frac{\mu}{m} \left[\left(\frac{\partial \Phi}{\partial X} \right)^2 + \left(\frac{\partial \Phi}{\partial Y} \right)^2 \right]_{z=0}^{1/2} \quad (24)$$

where μ is the apparent viscosity of the fluid mud.

There are a number of erosion theories which predict that the rate of erosion increases with increasing $\tau - \tau_c$. The exponential rate theories of PARTHENIADES (1965), CHRISTENSEN (1965), CHRISTENSEN and DAS (1973), RAUDKIVI and HUTCHISON (1974) and GULARTE (1978) were found to grossly underestimate the wing-induced erosion fluxes under the prototype conditions described in Section 7.0. This is consistent with the fact that these rate equations are based upon data from artificially placed beds which characteristically erode more slowly than naturally deposited beds, (MEHTA, *et al.*, 1982). The linear theories of KANDIAH (1974), ARULANANDAN (1975),

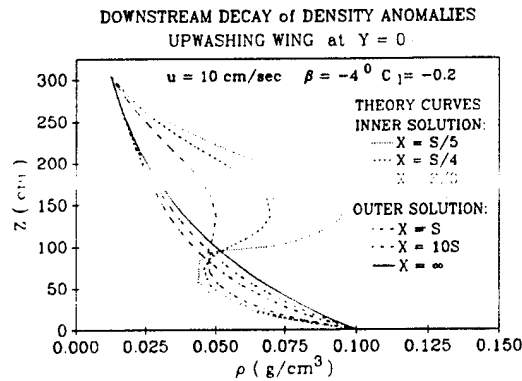


Figure 3 (A). Downstream decay of wing induced perturbations to the sediment component density as defined by equation (2). Calculations are based on: $\epsilon = 4.951 \text{ cm}^2/\text{sec}$, $\rho_1 = 0.0125 \text{ g/cm}^3$ and $\rho_c = 0.10 \text{ g/cm}^3$, and $h = S = 304.8 \text{ cm}$.

THORN and PARSONS (1980) and MEHTA (1981) can be calibrated from erosion rates observed over deposited beds because they are parameterized by a single empirically derived factor, α , according to:

$$E = \alpha \left(\frac{\tau - \tau_c}{\tau_c} \right) \quad (25)$$

Here $\alpha > 0$ and positive values of erosion flux, E , correspond to erosion.

A contour map of the wing induced erosion flux from (24) and (25) for $C_l = +0.2$ is calculated in Figure 5a for prototype conditions typ-

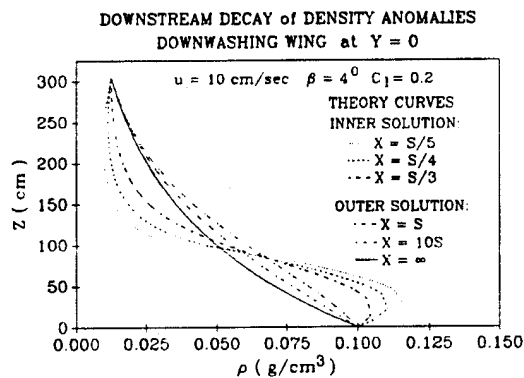


Figure 3 (B). Downstream decay of wing induced perturbations to the sediment component density as defined by equation (2). Calculations are based on: $\epsilon = 4.951 \text{ cm}^2/\text{sec}$, $\rho_1 = 0.0125 \text{ g/cm}^3$ and $\rho_c = 0.10 \text{ g/cm}^3$, and $h = S = 304.8 \text{ cm}$.

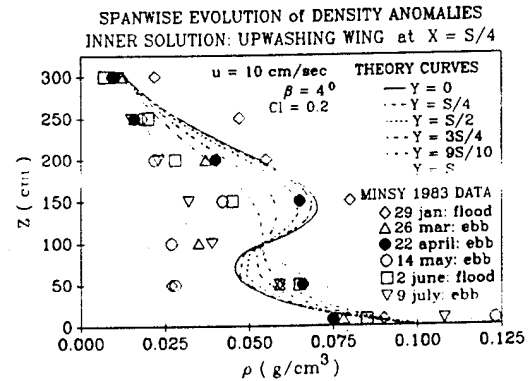


Figure 4 (A). Comparisons between theory and data for spanwise variations in the wing induced perturbations to the sediment component density in the near wake at $X = S/4$. Calculations are based on: $\epsilon = 4.951 \text{ cm}^2/\text{sec}$, $\rho_1 = 0.0125 \text{ g/cm}^3$ and $\rho_c = 0.10 \text{ g/cm}^3$, and $h = S = 304.8 \text{ cm}$.

ical of the experiment described in Section 7.0. Horseshoe-like erosion features are predicted in the near wake, due to the action of the horizontal induced velocity components. Such erosion is independent of the sign of the lift coefficient. However, erosion alone fails to account for shoaling details which might occur further downstream in response to an increased level of suspended sediment from mobilized bed material.

The deposition rate at $z = m$ is directly proportional to the abundance of suspended sedi-

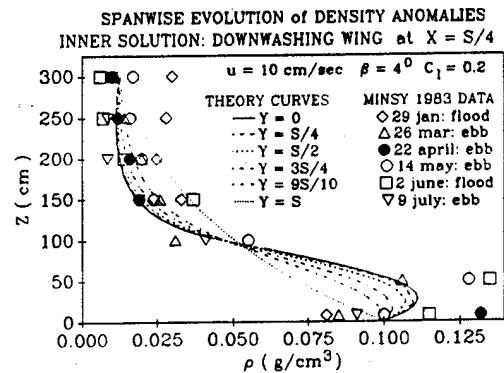


Figure 4 (B). Comparisons between theory and data for spanwise variations in the wing induced perturbations to the sediment component density in the near wake at $X = S/4$. Calculations are based on: $\epsilon = 4.951 \text{ cm}^2/\text{sec}$, $\rho_1 = 0.0125 \text{ g/cm}^3$ and $\rho_c = 0.10 \text{ g/cm}^3$, and $h = S = 304.8 \text{ cm}$.

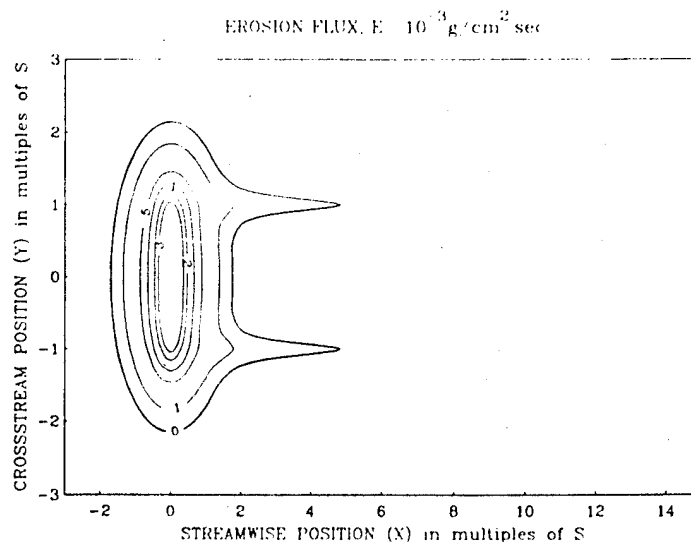


Figure 5. Contour maps of the erosion and deposition fluxes induced by a wing with $A_w = 5$ and $C_l = +0.2$ at a mooring elevation of $b = 100$ cm in a 10 cm/sec mean flow (A) Erosion flux for $\mu = 3.06 \times 10^{-2}$ gm/cm sec; $\tau_c = 0.5$ dynes/cm² and $\alpha = 2.356 \times 10^{-4}$ g/cm² sec.

ment near the bottom, (ARIATHURAI and KRONE, 1976, and COLE and MILES, 1983). This abundance is determined by the mass fluxes across the lutocline at $z = 0$. The flux of suspended sediment entering the fluid mud layer due to settling under gravity is $-\rho_c \omega_0$. These downward directed settling fluxes are the only mass fluxes considered by EINSTEIN and KRONE (1962), or MEHTA (1989) when accounting for deposition in the low turbulence environment of a settling column or laboratory flume. However in the high turbulence environment of a vortical wake in a natural estuary, vertical transport due to eddy diffusion must surely become important, especially along the strong density gradients in the neighborhood of the lutocline. The net of settling and diffusive fluxes across the lutocline determines the rate of change of suspended sediment in the fluid mud layer. However, there is only a finite probability, $p(0,1)$, that this suspended sediment will actually stick to the bed at $z = -m$ and consolidate to some ultimate saturation density ρ_* , (KRONE, 1962). Therefore the deposition flux, D , (including vertical diffusion and consolidation), may be written:

$$D = \frac{-K_s \rho_c g + p(0,1) \left\{ \rho_c \omega_0 - \epsilon \frac{\partial \rho}{\partial z} \Big|_{z=0} \right\}}{(1 - \rho_c / \rho_*)} \quad (26)$$

Here positive values for D correspond to deposition while negative values indicate entrainment.

With equations (10) and (21) in (26), wing induced deposition fluxes in the inner, D_i , and outer domains, D_o , become:

$$\left(\frac{D_o}{D_i} \right) = \frac{-K_s \rho_c g + p(0,1)}{(1 - \rho_c / \rho_*)} \left[\rho_c \omega_0 - \frac{\rho_c}{S} \left(\frac{2}{A_w} \frac{I_1(S) - I_1(0)}{I_2(S) - I_2(0)} \right) - \epsilon \log \frac{\rho_i}{\rho_c} \right] \quad (27)$$

A contour map of the deposition flux induced by a downwashing wing at $C_l = +0.2$ is given in Figure 5b for the prototype conditions described in Section 7.0. We find that the deposition is enhanced in the wake trail when C_l is positive. In this case, the downwash behind the wing has reduced or even reversed the density gradient at the lutocline, (see Figure 3b), so that upward diffusion from the fluid mud layer is either greatly diminished or turned around to augment settling. However, when C_l becomes negative (upwashing), downstream entrain-

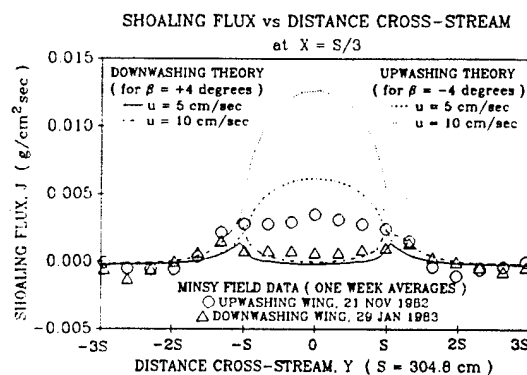


Figure 7. Comparison of shoaling flux theories and measurements across the wake trail at $X = S/3$. Theory curves based on a spanwise circulation distribution for a tapered wing according to (23) and parameterizations as in Figure 5.

venting deposition. In the case of erosion, the tangential velocities of the wing vortex system disturb the bottom directly by elevating the shear stresses in the fluid mud layer above the cohesive yield stress of the immobile bed. To prevent deposition the normal components of the induced velocities indirectly disturb future bottom profiles through their action on the density gradients above the lutocline. These normal induced velocities cannot directly cause advective fluxes of sediment across the lutocline because of vanishing normal flow along the stress free boundary at $z = 0$. By either mechanism shoaling is minimized by any given flow u_0 by maximizing the C_l which the wing can generate in ground effect. Thus the sensitivity of the wing's lift-drag polar to both boundary proximity and low Reynolds numbers is critical, with little existing airfoil research as such to support optimal design selections.

The question of an optimal mooring elevation and wing aspect ratio is dependent upon the relative importance of erosion vs deposition in determining future bottom profiles. Erosion, which prevails near the wing, is maximized by mooring elevations relatively close to the lutocline, $b = 0.25S$, and increases slightly with increasing wing aspect ratio as shown in Figure 8a. Very little improvement in maximum E occurs for $A_w > 5$. This behavior is dominated by the vortex sheet of the wing. Lower mooring elevations increase the near wake tangential velocities over the bed and hence the magnitude

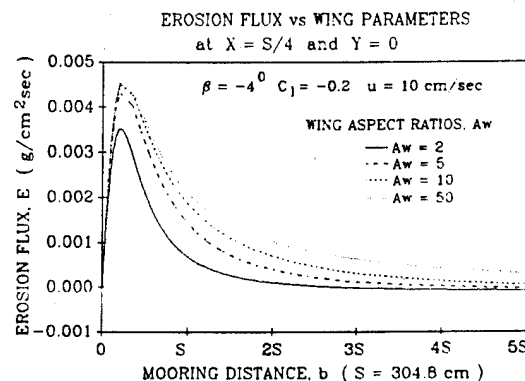


Figure 8. Variations of erosion and deposition fluxes with wing aspect ratio and mooring elevation. (A). Erosion flux at $X = S/4$.

of the shear stress within the fluid mud layer. Higher wing aspect ratios diminish tip loss effects near $Y = 0$. On the other hand, deposition is minimized at mooring elevations somewhat further above the lutocline, at $b = 0.8S$, and decreases rapidly with decreasing wing aspect ratio, as in Figure 8b. Since the deposition flux will be found to account for shoaled bottom profiles in the far wake, see Experiment section, such dependence on b and A_w is explicable in terms of the vertical velocities induced by the trailing vortices. Small mooring elevations and large wing aspect ratios tend to diminish the vertical induced velocities, with corresponding increases in the minimum attainable deposition flux.

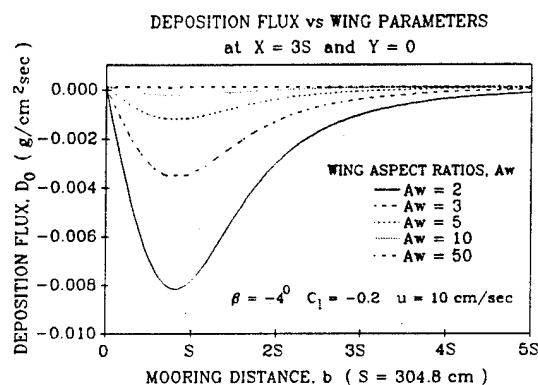


Figure 8 (B). Deposition flux at $X = 3S$. Parameterizations as in Figure 5, with $h = 5S$.

EXPERIMENT

Three buoyant wings were moored 100 cm above the initial bottom elevation of the Napa River at a mean depth of 10 meters. The configuration of the wings and their moorings is shown in Figure 1. Each wing was constructed of $1.6 \times 10^{-1} \text{ gm/cm}^3$ urethane foam reinforced by steel tendons and ribs. The semi-span was made large relative to the floc layer thickness, $S = 3.05$ meters, so that large density field aspect ratios are compatible with (5). A large wing aspect ratio was required to remain within the purview of the theory and to maximize erosion. However, the need for an adequate wing cord to satisfy (5) and subsequent ordering arguments dictated a compromise selection for the wing aspect ratio of $A_w = 5$, making the mean semi-cord $c = 0.61$ meters.

Because low wing Reynolds numbers were anticipated in the slow moving, highly viscous floc layer, a stall resistant model airplane airfoil, the HQ-3.5/12, was employed (QUABACK, 1983). This airfoil also had the advantage of a nearly constant pitching moment coefficient over a wide range in angle of attack, allowing the use of a single point mooring as diagrammed in Figure 1. The mooring point incorporated a swivel joint permitting complete rotational freedom to changes in current direction. The mooring point position and angle of attack were also fully adjustable by means of a pair of opposed turnbuckles under tension. The mooring attachment points were on the suction side of the upwashing wings with $\beta = -4^\circ$, corresponding to $C_l = -0.2$ acting downward against the buoyancy. The downwashing wings were moored from the pressure side with $\beta = +4^\circ$, so that $C_l = +0.2$ acting against the mooring tension. To maintain pitch, roll and yaw stability about this single point mooring, the wing plan form was configured with 30° of sweep back, 5° of dihedral, and small vertical stabilizers on each wing tip.

Two upwashing wings and one downwashing wing were installed in an 80×56 meter test area on November 11, 1982. The test area and a pair of 75×50 meter control areas were monitored by fathometer soundings, water sampling and diver inspection until November 6, 1983. The initial bottom topography in the test area was as shown in Figure 9a prior to wing installation. These contours were derived from

grid surveys using a 40 kHz fathometer. The test area was abreast of Dry Dock #1 at the Mare Island Naval Shipyard (MINSY) and was bordered by a sheet pile quay wall along the shoreward side. The two upwashing wings were moored at points A and B in Figures 9a and 9b while the downwashing wing was moored at point C.

Two Marsh-McBirney electromagnetic current meters were placed at the mooring elevation, $b = 100$ cm, above the bottom at the ebb and flood ends of the test area. Seven months of current records indicated that the near bottom currents were modulated by tidal action, consistent with assumptions of time variability made in (5). Peak current amplitudes were $O(20 \text{ cm/sec})$ while mean currents were $u_o \approx 10 \text{ cm/sec}$.

To measure the in situ values of (ρ_i, ρ_c, ρ_s) , bottom cores and water samples of the lower portion of the water column were collected throughout the experiment according to a schedule regulated by barge and ship movements along the river. Each sample volume, $O(500 \text{ ml})$, was determined to $O(0.5 \text{ ml})$ accuracy and subsequently suction filtered through #1 Whatman filter paper with an 11 micron pore size. After ashing and drying in an oven for 24 hours to remove organics and absorbed water, the mass of sediment retained by the filter paper was determined with a Mettler analytical balance to $O(10^{-5} \text{ g})$ accuracy. The ratio of sediment mass to total sample volume gave the sediment component densities equivalent to equation (2).

The test period coincided with the 1983 El Nino when regional rainfall and sediment abundance in the Napa River were at 100 year record levels, (USGS, 1983). During the high siltation period between November 1982 and July 1983, the shoaling rates in two distinctly different control areas were monitored. One of these control areas (Pier 21) was located in a quiet water cul-de-sac where there were no measurable bottom currents and hence no erosion. Here the mean shoaling flux was found to be:

$$\begin{aligned} \bar{J} &= -\bar{D} = \rho_s \frac{\partial \eta}{\partial t} \\ &= -1.185 \times 10^{-4} \text{ gm/cm}^2 \text{ sec} \quad (29) \end{aligned}$$

where η was the vertical position of the bed from 40 kHz fathometer soundings. From this

BOTTOM TOPOGRAPHY: BEGINNING OF EXPERIMENT 11 NOV 82

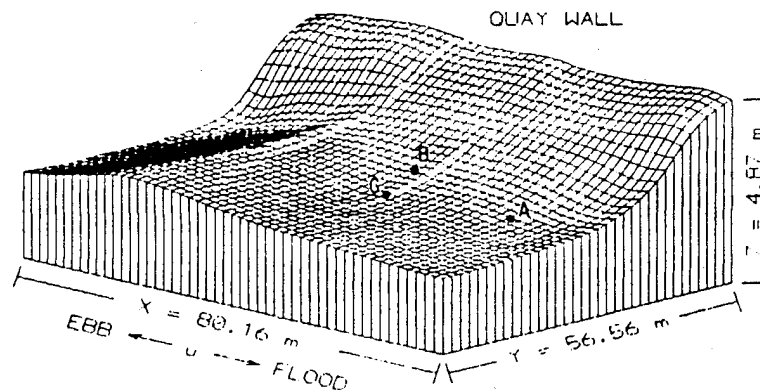


Figure 9 (A). Comparison of initial and final bottom configurations during the prototype wing test. Upwashing wings ($C_l < 0$) were moored at points A & B. A downwashing wing ($C_l > 0$) was moored at point C.

BOTTOM TOPOGRAPHY: END OF EXPERIMENT 6 NOV 83

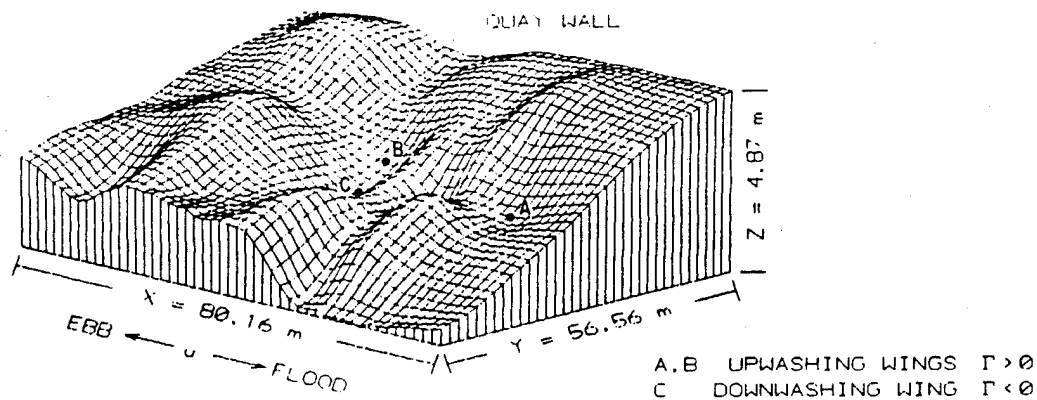


Figure 9 (B). Comparison of initial and final bottom configurations during the prototype wing test. Upwashing wings ($C_l < 0$) were moored at points A & B. A downwashing wing ($C_l > 0$) was moored at point C.

observed shoaling flux the mass diffusivity was calibrated by solving equation (27) for the case of no-wings, $I_1 = I_2 = 0$, to get:

$$\epsilon = \frac{\bar{J}(1 - \rho_c/\rho_s) - K_s \rho_c g + \rho_c \omega_0}{\frac{\rho_c}{S} \cdot \log\left(\frac{\rho_t}{\rho_c}\right)} \quad (30)$$

$$= 4.951 \text{ cm}^2/\text{sec}$$

Here, $\rho_t = 0.0125 \text{ g/cm}^3$, $\rho_c = 0.100 \text{ g/cm}^3$, and

$\rho_s = 1.2 \text{ g/cm}^3$ derived from averages of the in situ water samples collected in the control areas throughout the duration of the experiment. The sedimentation coefficient was taken as $K_s = 4 \times 10^{-13} \text{ sec}$ after the work of FUJITA (1962). A characteristic settling velocity in equation (30) of $\omega_0 = 0.035 \text{ cm/sec}$ was based upon a 25 micron median aggregate size determined by scanning electron microscopy size analysis of the suspended load in the Napa River water samples.

The fluid mud parameters (μ, m, τ_c) were derived from grab samples recovered by divers. These samples were placed immediately in a Brookfield Viscometer, giving average values of $\mu = 3.06 \times 10^{-2}$ gm/cm sec and $\tau_c = 0.5$ dynes/cm². The thickness of the fluid mud layer was estimated to be O(15 cm), based upon the band of abrasion appearing on the upper portions of the vertical steel members of the shear plate as shown in Figure 1. With these values and the calibrated mass diffusivity (30), we have invoked (27) and (28) to back out the erosion flux contribution to the observed mean shoaling flux at the remaining control area (Berth 7), and found that $\alpha = 2.356$ gm/cm² sec.

Sediment component densities measured approximately $x = S/4$ downstream of the upwashing wing-B are compared with the inner solution calculations (21) in Figure 4a. The majority of these measurements are found to lie in the envelope of the theory curves. This envelope is believed to be the correct standard for comparison because precise cross stream positioning during water sample collection was difficult while surface currents were running. In general the data show high levels of suspended sediments raised above the upwashing wing and locally smaller levels at the mooring elevations, $b = 100$ cm. Such a near bed density distribution is not typical of Nature. Thus an inversion layer has been created in the region above the floc layer by the upward advection of the near wake in reaction to downward lift.

Comparisons between theory and measured sediment component densities observed at $x = S/4$ downstream from downwashing wing-C are shown in Figure 4b. Samples yielding this data were gathered on the same days as those in Figure 4a and show comparable values above and at the bottom of the floc layer. However, in Figure 4b a high density toe of suspended sediment is found below the wing and above the presumed lutocline at $z = 0$. Some of the sediment component densities in this toe are actually in excess of those found at the lutocline. This, too, is an unnatural finding. Acoustic evidence of this near-bottom high density suspension is found downstream (LHS) of the echo return for wing-C in Figure 10a. The 40 kHz acoustic waves are known to back scatter from strong density gradients like those appearing above the bottom in Figure 4b, (KIRBY and PARKER, 1974). Hence, the downstream acoustic image

in Figure 10a is qualitatively consistent with the measured density anomalies near the bed in Figure 4b. Together, these observations support theoretical expectations that downwashing wings tend to drive suspended sediment down into the lower portions of the floc layer, causing an inversion layer below the wing.

Shoaling flux estimates derived from 40 kHz fathograms are compared with theory in Figures 6 and 7. One of these fathograms is shown in Figure 10b, taken along the centerline of the wake, ($y = 0$), behind an upwashing wing, B. The upwashing wings ($C_i < 0$) were found to diminish downstream shoaling while the downwashing wings ($C_i > 0$) were found to cause downstream accretion, although the outer solution for the shoaling flux tends to underestimate both. The momentum diffusivity was fixed at $\sigma = 3\epsilon$ in order to match the length of the scour trail with the data. The data were based upon one week averages shortly after the wing installations were completed, when the erosion fluxes were relatively large.

In the near wake of the wing, the inner solution of the shoaling flux was found in Figures 6 and 7 to overestimate the observed erosion due to an upwashing wing by a considerable amount. This is believed to be due to the assumption of a constant τ_c when posing the erosion flux according to (25). As erosion cuts into the bed, denser more consolidated mud is exposed which has a higher cohesive yield stress and is thus more resistant to erosion than predicted by the calculations in Figures 6 and 7. This argument is supported by the fact that the smaller positive shoaling fluxes which do not entail erosion cuts as deeply into the bed are predicted reasonably well in the near wake of a downwashing wing. Unfortunately, the calculation does not account for the unshoaled intermediate region between $2S < x < 8S$ behind a downwashing wing. This may again be due to cross stream positioning errors if the fathometer sweep was performed along one of the erosive tails of the horseshoe at $Y = S$ in Figure 5a rather than along the centerline of the wake, $Y = 0$.

The rate of erosion of naturally deposited beds typically decreases with increasing time and may eventually arrest altogether, (MEHTA *et al.*, 1982). Not only does erosion expose denser, more erosion-resistant material, it also increases the effective mooring elevation,

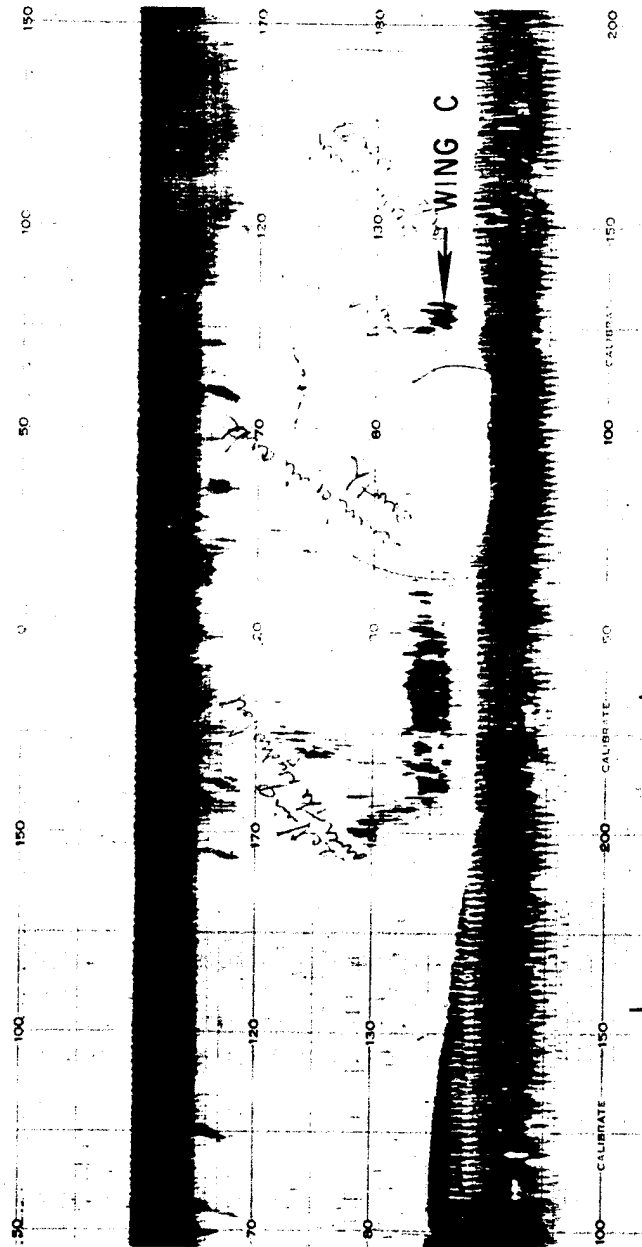


Figure 10. 40 kHz fathograms of the moored wings. (A). Shows acoustic reflection from a dense suspension of sediment behind downwashing wing C at a $C_L = +0.2$.

thereby reducing further erosion while increasing downstream deposition in accordance with the results of Figures 8a and 8b. The image method calculations also become increasingly inaccurate as the bottom deviates from a plane

configuration. Flow divergence over wing induced scour holes will surely reduce the circulation which the wing can generate. These factors all work together over time to slow or arrest erosion. A final steady state bottom con-

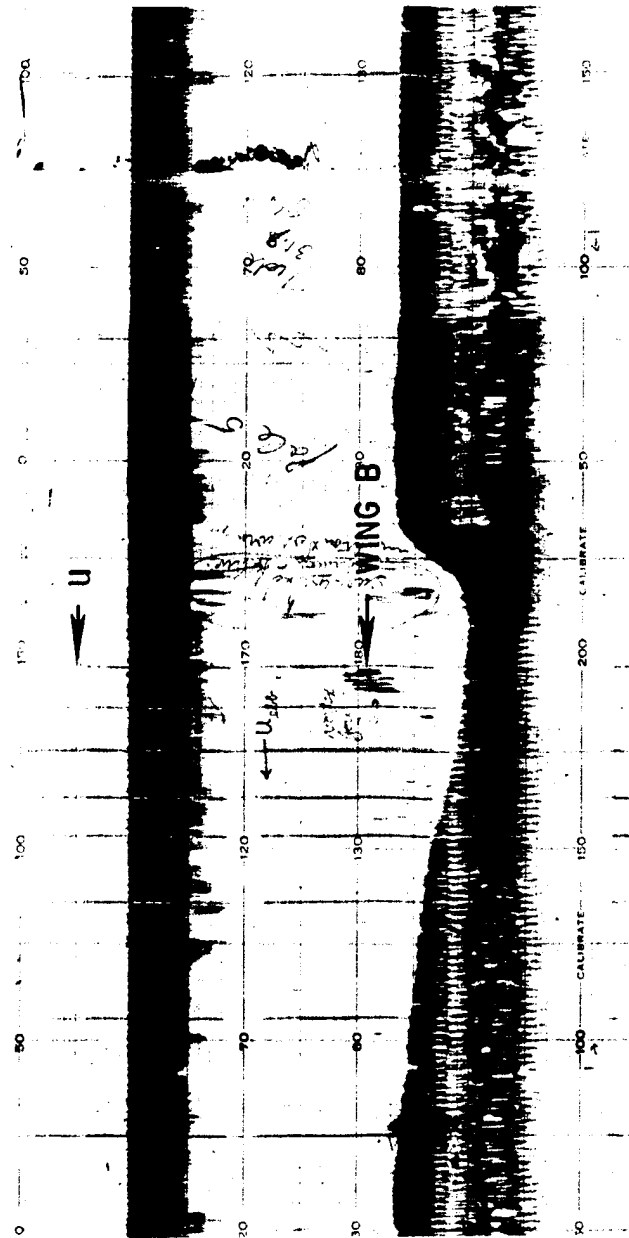


Figure 10. (B). Shows the scour trail plotted in Figure 6 induced by upwashing wing B.

figuration as shown in Figure 9b was found 12 months later. The long-term erosion process has produced local scour holes in the neighborhood of both downwashing and upwashing wings alike. Such features are qualitatively similar to the erosion simulation depicted in

Figure 5a. None of the long extended scour trails associated with entrainment and diminished deposition behind an upwashing wing are still in evidence in the final steady state bottom configuration. Thus deviations from a flat bottom in consequence of near-wake erosion

appears to greatly inhibit vertical mass transport in the wake. Even so, it is significant that none of the wings became buried after one year of continual submergence, in spite of the higher than normal siltation rates that persisted throughout the test period.

CONCLUSIONS

Wing induced perturbations to the density field of suspended sediment appear to be qualitatively accounted at $O(R_F/A_w)$. Wings in ground effect which generate a downward lift force give rise to density inversions above the wing. Wings producing an upward lift force cause density inversions to appear below the wing.

Short term wing induced perturbations to the bottom appear to be qualitatively explained by entrainment and diminished deposition in the far wake and by erosion in the near wake. Wings which generate a downward lift force induce erosion in both the near and far wakes. Wings which generate an upward lift force give rise to erosion in the near wake followed by accretion in the far wake.

Long term wing induced perturbations to the bottom are qualitatively explicable only in terms of erosion.

Both erosion and entrainment are maximized by maximizing wing section lift coefficients while in ground effect at low wing Reynolds numbers.

There exists no unique selection of mooring elevation and wing aspect ratio which simultaneously maximizes erosion and minimizes downstream deposition. Erosion is maximized by maximizing wing aspect ratio for a mooring elevation of $b = 0.25S$. Deposition is minimized by minimizing wing aspect ratio with $b = 0.8S$.

Wings which generate a downward lift force are more effective in causing local erosion and retarding downstream deposition than wings generating an upward lift force. Because either effect is limited to a wake trail whose cross-stream dimension is of the order of a wing span, large areas of channel bottom will require mass arrays of wings with overlapping wakes (like a flock of birds), in order to control shoaling.

ACKNOWLEDGEMENTS

The authors are indebted to Dr. Eugene Silva and Dr. Steven Ramberg of the Office of Naval

Research, Code 1121, for technical support and sponsorship of this research. We further wish to thank Mr. Joseph Sparks for diver support and a number of mechanical innovations throughout the wing test at Mare Island Naval Shipyard. Also, Dr. Darold (Jim) Palmer is specially credited for instrumentation and concrete mold technology used in wing construction.

LITERATURE CITED

- ARIATHURAI, R., and KRONE, R.B., 1976. Finite element model of cohesive sediment transport. *Journal of the Hydraulics Division*, ASCE, 102, HY3, 323-338.
- ARULANANDAN, K., 1975. Fundamental aspects of erosion of cohesive soils. *Journal of the Hydraulics Division*, ASCE, 101 (445), 635-639.
- APMAN, R.P., and RUMER, R.R., 1970. Diffusion of sediment in developing flow. *Journal of the Hydraulics Division*, ASCE, 96, HY1, 109-123.
- BATCHELOR, G.K., 1964. Axial flow in trailing line vortices. *Journal of Fluid Mechanics*, 20, 645-658.
- BETZ, A., 1912. *Zeitschrift fur Flugtechnik und Motorluftschiffahrt*, Germany, 13, 86p.
- CHENG, K.J., 1985. An integrated suspended load equation for non-equilibrium transport of nonuniform sediment. *Journal of Hydrology*, 79, 359-364.
- CHIEW, J.M., and MELVILLE, B.W., 1987. Local scour around bridge piers. *Journal of Hydraulic Research*, 25, 15-26.
- CHRISTENSEN, B.A., 1965. Discussion of erosion and deposition of cohesive soils (by E. Partheniades). *Journal of the Hydraulics Division*, ASCE, 91(HY5), 301-308.
- CHRISTENSEN, R.W., and DAS, B.M., 1973. Hydraulic erosion of remolded cohesive soils, pp. 8-19. In: National Research Council, (ed.), *Soil Erosion: Causes and Mechanisms, Prevention and Control*. Highway Res. Board Special Report 135, Washington, D.C.
- COLE, P., and MILES, G.V., 1983. Two-dimensional model of mud transport. *Journal of Hydraulic Engineering*, ASCE, 109, No. 1, 1-12.
- COLLINS, T.J., 1980. Investigating bridge scour. *Railway Track and Structure*, 76p.
- DYER, K.R., 1985. *Coastal and Estuarine Sediment Dynamics*, New York: Wiley, 342p.
- EINSTEIN, H.A., and KRONE, R.B., 1961. Estuarine sediment transport patterns. *Journal of the Hydraulics Division*, ASCE, 87, HY2, 1451-1461.
- EINSTEIN, H.A., and KRONE, R.B., 1962. Experiments to determine the models of cohesive sediment transport in salt water. *Journal of Geophysical Research*, 67, 4, 1451-1461.
- FAAS, R.W., 1985. Time and density-dependent properties of fluid mud suspensions, NE Brazilian continental shelf. *Geo-Marine Letters*, 4, 147-152, 184-185.
- FUJITA, H., 1962. *Mathematical Theory of Sedimentation Analysis*. York: Academic 315p.
- GARRAD, P.N., and HEY, R.D., 1987. Boat traffic,

- sediment resuspension and turbidity in a broadland river. *Journal of Hydrology*, 95, 289-297.
- GOVINDARAJU, S.P., and SAFFMAN, P.G., 1971. Flow in a turbulent trailing vortex. *Physics of Fluids*, 14, 2074-2080.
- GREEN, G.C., 1985. An approximate model of vortex decay in the atmosphere. *AIAA 12th Flight Mechanics Conference*, 85-1835.
- GULARTE, R.C., 1978. Erosion of cohesive marine sediment as a rate process. Ph.D. Thesis, University of Rhode Island, Kingston, RI, 190p.
- HILL, F.M., 1975. A numerical study of the descent of a vortex pair in a stably stratified atmosphere. *Journal of Fluid Mechanics*, 71, 1-13.
- JENKINS, S.A., and SPARKS, J.B., 1985. *Method and apparatus for impeding fine sediment deposition in harbor and navigation channels*. U.S. Patent #4,560,304.
- JENKINS, S.A., 1987. *Apparatus for impeding fine sediment deposition in harbor and navigation channels*. U.S. Patent #4,661,013.
- KANDIAH, A., 1974. Fundamental aspects of surface erosion of cohesive soils. Ph.D. Thesis, University of California, Davis, CA, 261p.
- KERSSENS, M.J.; PIRNS, A.D., and van Rijn, L.C., 1979. Model for suspended sediment transport. *Journal of the Hydraulics Division*, ASCE 105(HY5), 461-476.
- KIRBY, R., and PARKER, W.R., 1974. Sea-bed density measurements related to echo-sounder records. *Dock and Harbour Authority*, 54, 423-424.
- KRONE, R.B., 1962. *Flume Studies of the Transport of Sediment in Estuarial Shoaling Processes*. Final report, Hydraulics Engineering Laboratory and Sanitary Engineering Research Laboratory, University of California, Berkeley.
- KRONE, R.B., 1978. Aggregation of suspended particles in estuaries. In: *Estuarine Transport, Process*, B. Kjerfve, (ed.). University of South Carolina Press, Columbia, SC, pp. 177-190.
- LAGALLY, M., 1929. *Zeitschrift für Angewandte Wulshewatch und Mechanik*, 9, 299-305.
- LAMBERMONT, J., and LEBON, G., 1978. Erosion of fine soils. *Journal of Hydraulic Research*, 16, 27-33.
- LANCHESTER, F.W., 1908. *Aerodynamics*, New York: Van Nostrand, 442p.
- MacLENNAN, A.S.M., and VINCENT, J.H., 1982. Transport in the near aerodynamic wakes of flat plates. *Journal of Fluid Mechanics*, 20, 185-197.
- MARINE BOARD, (National Research Council). 1983. *Criteria for the depths of dredged navigational channels*. Washington, D.C., National Academy Press.
- MATTEI, A., and SANTORO, E., 1974. Numerical computations of wake vortices behind lifting surfaces. *International Conference of Aeronautical Science*, pp. 244-249.
- MCCORMICK, B.W., 1979. *Aerodynamics, Aeronautics, and Flight Mechanics*. New York: Wiley, 653p.
- McMASTERS, J.H., 1974. An analytic survey of low-speed flying devices—natural and man-made. *Journal of Technical Soaring*, 111 (4), 17-39.
- MEHTA, A.J., and PARTHENIADES, E., 1975. An investigation of the depositional properties of flocculated fine sediments. *Journal of Hydraulics Research*, 13, 4, 361-381.
- MEHTA, A.J., 1981. Review of erosion function for cohesive sediment beds. *Proceedings First Indian Conference on Ocean Engineering*, Indian Institute of Technology, Madras, India, I, pp. 122-130.
- MEHTA, A.J.; PARCHURE, T.M.; DIXIT, J.G., and ARIATHURAI, R., 1982. Resuspension Potential of Deposited Cohesive Sediment Beds. *Estuarine Comparisons*. New York: Academic, 709p.
- MEHTA, A.J., HAYTER, E.J.; PARKER, W.R.; KRONE, R.B., and TEETER, A.M., 1989. Cohesive sediment transport. I: Process description. *Journal of Hydraulic Engineering*, 115, (8), 1076-1093.
- MEHTA, A.J.; McANALLY, W.H., JR.; HAYTER, E.J.; TEETER, A.M.; SCHOLELLHAMER, D.; HELTZEL, S.B., and CAREY, W.P., 1989. Cohesive sediment transport. II: Application. *Journal of Hydraulic Engineering*, 115, (8), 1094-1112.
- MEHTA, A.J., 1989. On estuarine cohesive sediment suspension behavior. *Journal of Geophysical Research*, 94, (C10), 14,303-14,314.
- MEI, C.C., 1969. Nonuniform diffusion of suspended sediment. *Journal of the Hydraulics Division*, ASCE 95(HY1), 581-584.
- MOORE, D.W., 1974. A numerical study of the roll-up of a finite vortex sheet. *Journal of Fluid Mechanics*, 63, 225-235.
- NICHOLS, M.N., 1985. Fluid mud accumulation processes in an estuary. *Geo-Marine Letters*, 4, 171-176(1984-1985).
- PARKER, W.R., and KIRBY, R., 1982. *Estuarine Comparisons*. New York: Academic, pp. 573-589.
- PARTHENIADES, E., 1965. Erosion and deposition of cohesive soils. *Journal of the Hydraulics Division*. ASCE 91, (HY 1), Proc Paper 4204, pp. 105-139.
- PEACE, A.J., and RILEY, N., 1983. A viscous vortex pair in ground effect. *Journal of Fluid Mechanics*, 129, 409-426.
- PHILLIPS, W.R.C., 1981. The turbulent trailing vortex during roll-up. *Journal of Fluid Mechanics*, 105, 451-467.
- PRANDTL, L., 1931. *Abriss der Stromungslehre*. Braunschweig, Germany: Vieweg, 223p.
- PRANYTL, L., and BETZ, A., 1927. *Vier Abhandlungen zur Hydrodynamik und Aerodynamik*. Göttingen, Germany: Gelbster Verlag des Kaiser Wilhelm Institute für Stromungsforschung, 110p.
- PRESNAK, W.J., 1977. Some special cases of potential flow around multi connected airfoils. *Bulletin de l'Académie Polonaise des Sciences, Série des Sciences Technique*, XXV, 37-44.
- PULLIN, D.I., and PHILLIPS, W.R.C., 1981. On a generalization of Kaden's problem. *Journal of Fluid Mechanics*, 104, 45-53.
- QUABACK, H., 1983. "HQ-Profile," *Modell Technik Berater, MTB-7*. Verlag für Technik Und Handwerk GmDH., Baden-Baden, Germany, 70p.
- RAUDKIVI, A.J., and HUTCHINSON, D.L., 1974. Erosion of kaolinite clay by flowing water. *Proceedings of the Royal Society of London*. A337, 537-554.
- SAFFMAN, P.G., 1972. The motion of a vortex pair in a stratified field. *Studies in Applied Mathematics* LI, (2), 107-110.

- SAFFMAN, P.G., 1973. Structure of turbulent line vortices. *Physics of Fluids*, 16, 1181-1188.
- SQUIRE, H.B., 1965. The growth of a vortex in turbulent flow, *Aeronautical Quarterly*, 16, 302-306.
- STAUFENBIEL, R., and KLEINERDAM, G., 1980. Longitudinal motion of low-flying vehicles in non-linear flowfields. *International Conference of Aeronautical Science*, 293-308.
- THORN, M.F.C., and PARSONS, J.G., 1980. Erosion of cohesive sediments in estuaries: an engineering guide. *Proceedings 3rd International Symposium Dredging Technology*, pp. 349-358.
- USGS, 1983. *Water Resources Data for California*. U.S. Geological Survey, #CA-83-2.
- VAN DYKE, M., 1964. Lifting-line theory as a singular-perturbation problem. *Journal of Applied Mathematics and Mechanics*, 28, 90-101.
- VAN DYKE, M., 1975. *Perturbation Methods in Fluid Mechanics*. Stanford, California: Parabolic, 271p.
- VANONI, V.A., (ed.), 1975. *Sedimentation Engineering*. New York: American Society of Civil Engineers, 745p.
- WERLE, H., 1973. Hydrodynamic flow visualization. *Annual Review of Fluid Mechanics*, 5, 361-382.
- WRIGHT, V.G., and KRONE, R.B., 1977. Laboratory study of mud flows. *Proceedings of National Conference on Hydraulic Engineering*, 237-242, (American Society of Civil Engineers, New York).
- YALIN, M.S., 1977. *Mechanics of Sediment Transport*. Oxford: Pergamon, 290p.

□ RESUMEN □

Se muestra en este trabajo una teoría con correspondiente experimentación que describe la resuspensión de sedimentos finos debida a la acción de alerones anclados cerca del fondo de un estuario. Los cálculos mediante el método de las imágenes indican que el sistema de vórtices de un alerón puede ejercer dos efectos diferentes sobre la sedimentación del estuario: 1) Puede aumentar la tensión tangencial en las proximidades del alerón hasta una cantidad suficiente como para inducir la erosión de las capas de sedimento de fondo parcialmente consolidadas; y 2) puede promover transporte vertical que incremente o disminuya la sedimentación corriente abajo. Se ha encontrado que la sedimentación en la cola de la estela depende de la dirección de la fuerza de sustentación generada por el alerón. Los alerones que producen una fuerza de sustentación descendente limpian la región adyacente del fondo de sedimento suspendido y, por lo tanto, disminuye la sedimentación aguas abajo. Recíprocamente, los alerones que generan una fuerza de sustentación ascendente incrementan la concentración de sedimento suspendido cerca del fondo, incrementando por lo tanto la tasa de sedimentación aguas abajo. Se formulan las configuraciones de alerones óptimas que maximizan la erosión y minimizan la sedimentación. Las medidas de concentración detrás de prototipos de alerones son consistentes con las expectativas teóricas. Los cambios a corto plazo de la batimetría del fondo se ajustan en general con la erosión predicha en el dominio interior y con la menor acreción en el dominio exterior. *Department of Water Sciences, University of Cantabria, Santander, Spain.*

□ RÉSUMÉ □

Présente une expérimentation décrivant la resuspension des sédiments fins sous l'action d'ailes amarrées près du fond dans un estuaire. Les calculs réalisés par ajustement à des expansion d'images internes et externes indiquent que le vortex d'une aile peut exercer deux effets distincts sur la sédimentation estuarienne. 1) Il peut accroître par une quantité suffisante la force de cisaillement du voisinage et induire une érosion des couches partiellement consolidées du fond. 2) Il peut promouvoir un transport vertical qui soit augmente, soit diminue le dépôt aval. Dans la traînée du sillage, le dépôt est dépendant de la force d'élévation entraînée par l'aile. Les ailes qui produisent une force d'élévation en aval provoquent le départ des sédiments fins en suspension près du fond et diminuent le dépôt aval. A l'inverse, les ailes engendrant une force vers le haut accroissent la densité des sédiments en suspension près du fond et accroissent donc le dépôt en aval. Les mesures de densité derrière les ailes du prototype coïncident avec ce qui pouvait être déduit de la théorie. Les changements à court terme des formes de fond coïncident généralement avec l'érosion prédite dans le domaine interne et avec une accretion diminuée dans le domaine externe. —Catherine Bressolier, *Géomorphologie EPHE, Montrouge, France.*

□ ZUSAMMENFASSUNG □

Eine Theorie und ein begleitendes Experiment werden vorgestellt, die die Wiederaufnahme feinkörniger Sedimente als Suspensionsfracht aufgrund von Flügeln beschreiben, die am Grunde eines Ästuars verankert sind. Berechnungen zeigen, daß die Wirbelbildungen an einem solchen Flügel zwei verschiedene Auswirkungen auf die Sedimentation im Ästuar haben können: 1) Sie können die Schubspannungen in der Umgebung des Flügels um ein solches Ausmaß erhöhen, daß dadurch die Erosion von teilweise verfestigten Schichten am Ästuargrund ausgelöst wird; und 2) können sie den vertikalen Transport fördern, um eine stromabwärtige Ablagerung entweder zu steigern oder zu hemmen. Es ergab sich, daß die Sedimentation im Kielwasserbereich von der Richtung der Hubkraft abhängig ist, die von dem Flügel erzeugt wird. Flügel, die eine nach unten gerichtete Hubkraft bewirken, beseitigen Schwebgut in dem am Grunde angrenzenden Gebiet und vermindern dadurch die stromabwärtige Ablagerung. Umgekehrt vergrößern Flügel, die eine nach oben gerichtete Hubkraft bewirken, die Schwebgutdichte nahe dem Grunde und dadurch auch die stromabwärtige Ablagerungsrate. Bestmögliche Flügelgestaltungen werden vorgeschlagen, die die Erosion maximieren und die Ablagerung minimieren. Dichtemessungen bei Prototyp-Flügeln stimmen mit diesen theoretisch abgeleiteten Erwartungen überein. Kurzzeitige Veränderungen des Reliefs am Ästuarboden stehen im generellen Einklang mit der vorhergesagten Erosion im inneren und der verminderten Anlagerung im äußeren Flügelbereich. —Helmut Brückner, *Geographisches Institut, Universität Düsseldorf, F.R.G.*

**APPENDIX B: TRANSPORT OF FINE SEDIMENTS
BY HYDROSTATIC JETS**

by

SCOTT JENKINS, SAIMA AIJAZ & JOSEPH WASYL

Transport of Fine Sediments by Hydrostatic Jets

Scott A. Jenkins, Saima Aijaz and Joseph Wasyl

Reprinted From *Nearshore and Estuarine
Cohesive Sediment Transport*

Ashish J. Mehta (Ed.)

Coastal and Estuarine Studies

Published by the American Geophysical Union

Transport of Fine Sediments by Hydrostatic Jets

Scott A. Jenkins, Saima Aijaz and Joseph Wasyl

The effects of hydrostatic jets (those without propagating horizontal pressure gradients) on the transport and entrainment of fine grain estuarial sediments from the near bottom fluid mud layers are considered. Using mixing length arguments it is proposed that the elevated shear stresses resulting from these jets transport suspended sediment vertically upward across the lutocline, thereby reducing the abundance of suspended sediment directly adjacent to the consolidated bed. Through this entrainment the jets were found to cause reductions in the deposition rates. The extinction of jet-induced bottom stress with increasing distance from the jet was measured on laboratory scales and found to obey a power law over several orders of magnitude. This power law was invoked in a vertical advection-diffusion model to calculate the variation in jet entrainment flux with increasing distance away from the jet discharge nozzle. These calculations were compared with field measurements conducted at three different sites for a variety of jet discharge velocities, diameters and flow rates. When low salinity surface water was pumped through the jets, the entrainment flux at great distances was larger than expected. Consequently, the calculations required the assumption of a reduced cohesive yield stress to match the measured values. This was supported by laboratory viscometer measurements using native suspensions with artificially depressed salinities.

Introduction

Water jets have been employed since the late nineteenth century as a means for agitation dredging. This application requires large amounts of horsepower in order to achieve jet induced shear stresses in excess of the critical erosion stress of consolidated muds. Consequently the jets have only a local effect and require some sort of mobile platform to scour and erode large areas of muddy estuarial waterways. Furthermore significant increases in turbidity result from this practice which ultimately limit its application in environmentally sensitive areas.

In recent years automated jetting systems have been attached to piers and quay walls to resuspend fluid mud before it remains immobile long enough to form partially consolidated mud, see Jenkins, Bailard and Inman (1980), Jenkins

and Bailard (1989), Heinz, Bailard, and Jenkins (1989). In this application the jetting system does not function as a dredging device which must induce erosion. Rather, the jetting system is employed as a depth maintenance device which must merely produce enough bottom stress to exceed the cohesive yield stress of mobile fluid mud in order to effect its resuspension. These automated jetting systems fall into two basic classes; (1) pump based systems; and (2) ducted propeller based systems. The pump based systems consist of a centrally located pump which discharges through a manifold to a line array of fixed bottom mounted jets, see Fig. 1. Control valves at each branch point along the manifold regulate the entire pump discharge sequentially through each jet for a predetermined duty cycle. The bottom mounted jets consist of a convergent nozzle. The operation of the jet system is controlled by a computer which sequences its operations to coincide with early ebbing tide immediately after slack water. When operated on a daily basis only a relatively thin fluid mud layer is reintroduced into the water column, rather than the deposition of an entire season as in the case of agitation dredging.

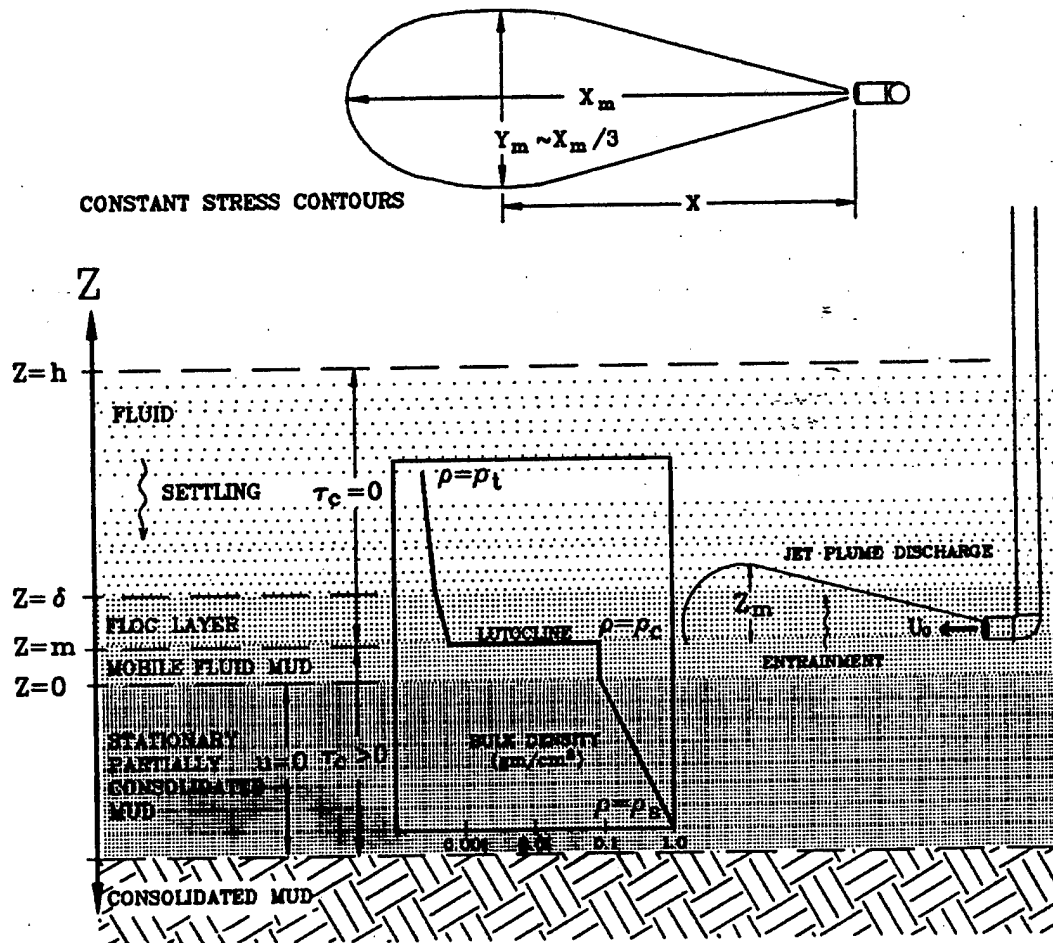


Figure 1. Section view of the pump based jet system at the Port of Grays Harbor, Washington.

The propeller based systems operate in a similar manner, but employ ducted fans rather than centrifugal impellers to drive the jet flow, see Fig. 2. These systems are detailed in Bailard and Jenkins (1990). The propeller is mounted inside a vertically oriented 90° elbow with a horizontal discharge at the bottom. This configuration protects the propeller from bottom debris or slumping mud banks, as commonly found beneath piers and docks. The elbow may be hinged to a frame and articulated with a hydraulic ram to allow the jet to scan through 180° arcs, thereby increasing the area of influence of the jet discharge. Whereas the pump based systems generally produce a high velocity low flow rate jet through a small convergent nozzle, the propeller based system produces a relatively low velocity jet at a very high flow rate. We shall show subsequently that either high velocity or high flow rate jets are capable of elevating bottom stresses sufficiently to exceed the cohesive yield stress of fluid mud and thereby induce resuspension.

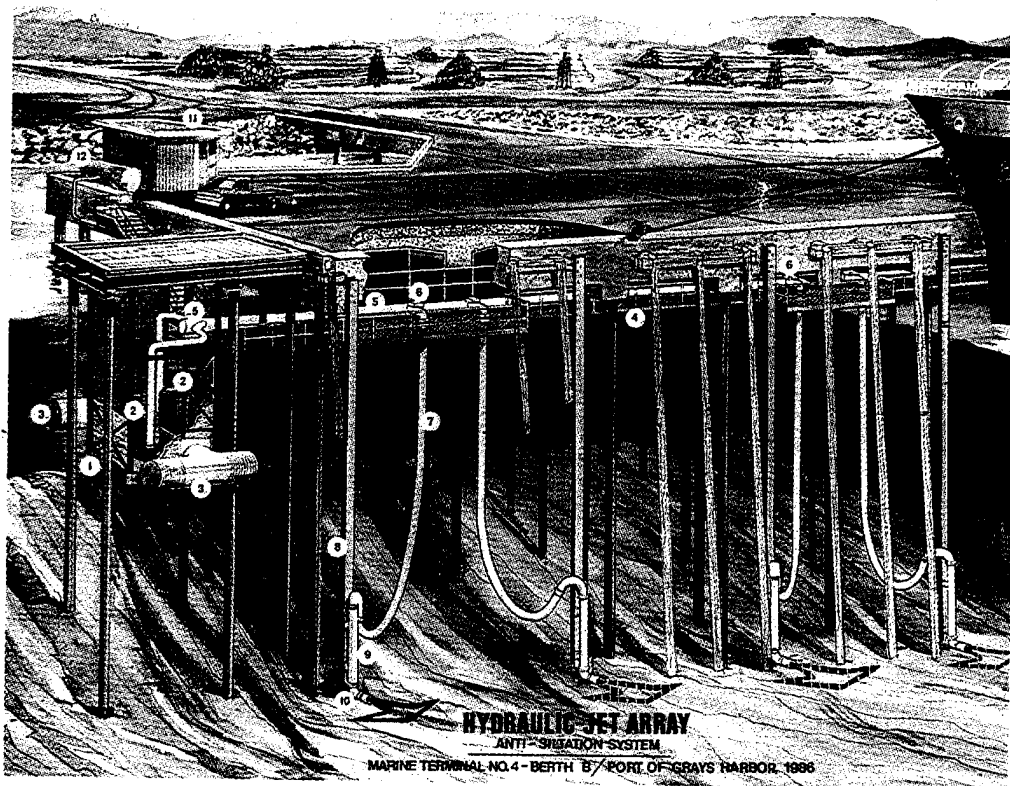


Figure 2. Schematic of the propeller based jet system tested at the Port of Grays Harbor November 1989 - February 1990. Components are indicated as follows: 1) pump chamber; 2) 400 h.p. pump; 3) water intake screens; 4) access catwalk; 5) 24" manifold pipe; 6) butterfly control valve; 7) 12" nozzle supply hose; 8) nozzle guide pile; 9) nozzle support assembly; 10) nozzle - 13,700 g.p.m. output; 11) control house; 12) air tank.

Theory

Consider a jet discharging horizontally across a partially consolidated muddy bottom at $z = 0$, as shown in Fig. 3. Let the jet diameter at the discharge point be, d , where the centerline axial velocity of the jet discharge is U_0 . Above the bottom at $z = 0$ assume a suspension of uniform particles, each with a settling velocity relative to the fluid, ω_0 and a solid density, $\rho_q = 2.65 \text{ g/cm}^3$. If the density of the fluid is ρ_f , then the density of the fluid sediment mixture, ρ_m may be written:

$$\rho_m = \rho_q N + (1-N)\rho_f \quad (1)$$

where N is the volume concentration equal to the volume of sediment per volume of the fluid-sediment mixture. The density of the sediment component of this mixture, ρ , is sometimes referred to as the excess density and is defined:

$$\rho = \rho_q N \quad (2)$$

The upper regions of the water column are relatively deficient of suspended sediment, where the density of the sediment component at the free surface, $z = h$, is $\rho = \rho_f$. Because of settling under the influence of gravity the abundance of suspended sediment begins to increase in the neighborhood of the bottom below $z = \delta$, forming a non-cohesive floc layer as shown in Fig. 3, see Mehta and Partheniades (1975) and Krone (1978). At the bottom of the floc layer, at $z = m$, there is a rapid increase in bulk density referred to in the recent literature as a lutocline, see Dyer (1985) and Mehta (1989). At or below the lutocline the suspended sediment concentrations are sufficiently high for the fluid sediment mixture to exhibit a non-zero cohesive yield stress, τ_c , and behave therefore as a viscoplastic. Above the lutocline at $z = m$, the cohesive yield stress vanishes and the fluid sediment mixture behaves as a fluid, i.e. unable to support shear stress at equilibrium. The sediment component density at $z = m$, where the fluid sediment mixture first begins to exhibit a cohesive yield stress, is $\rho = \rho_c$. The region between the lutocline and the immobile partially consolidated bottom at $z = 0$ is referred to as a fluid mud layer which may exhibit a non-zero velocity when applied stresses exceed the cohesive yield stress. Thus the lutocline at $z = m$, between the fluid and the viscoplastic material, is not a no-slip boundary. For analytic purposes we shall assume that the lutocline at $z = m$ is a stress free boundary much like a free surface, with the shear stresses resulting from fluid motion appearing in the stress field of the fluid mud layer itself. This assumption relieves the equations of motion for the velocity field of the jet on the fluid side of the interface from having to satisfy a no-slip condition at $z = m$. The no-slip boundary appears at the immobile partially consolidated bottom at $z = 0$. We shall assume there are minor

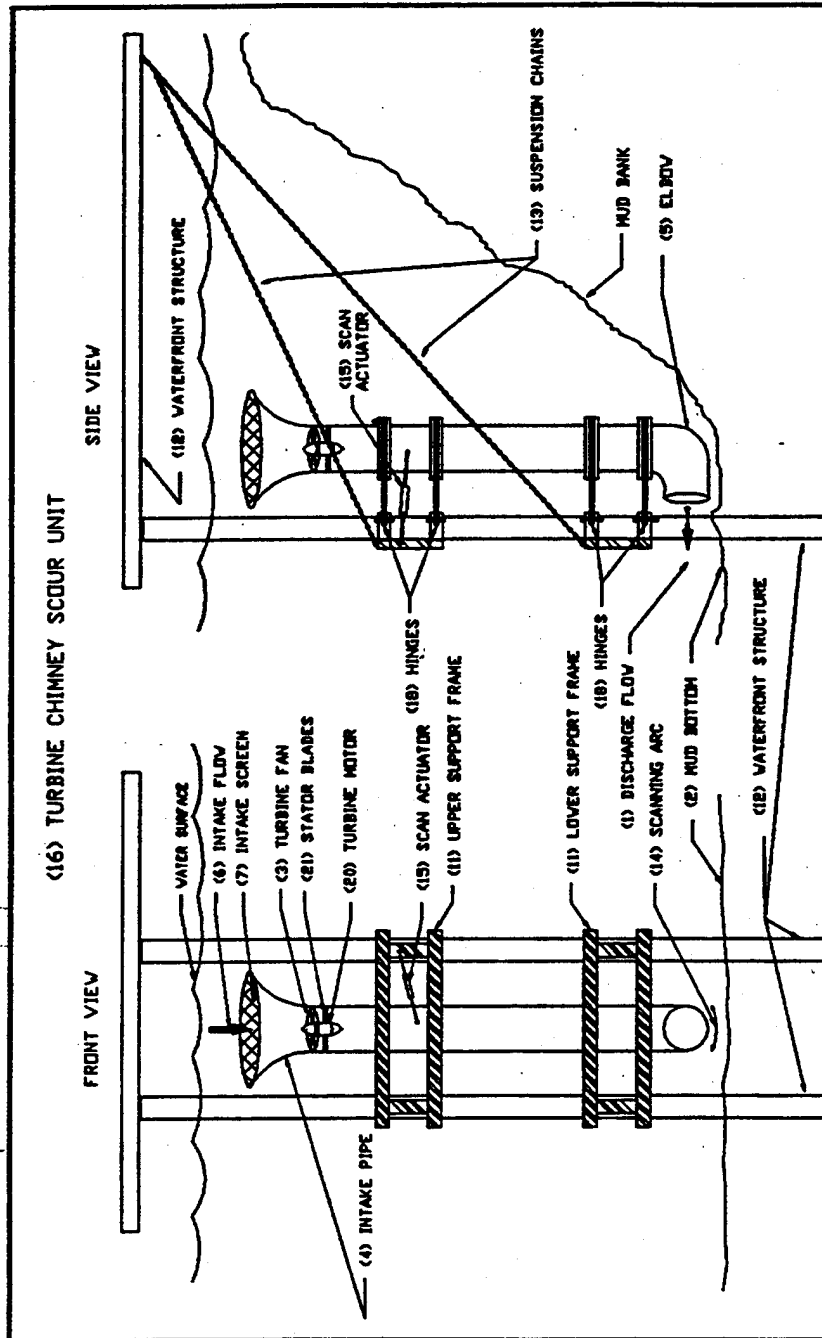


Figure 3. Conceptual diagram of the fluid bed interface as influenced by a generic hydrostatic jet.

irregularities along the surface $z = 0$ whose elevations are characteristically, z_0 , where $z_0 \ll m$.

Below the fluid mud layer, $z < 0$, the sediment is at rest and there is a progressive buildup in sediment component density to some ultimate saturation value, $\rho = \rho_s$. This is due to consolidation and compaction under the weight of the overburden which proceeds at a rate characterized by $\rho_c K_s g$, where g is the acceleration of gravity and K_s is the sedimentation coefficient in seconds, Fugita (1962). The portion of the cohesive bottom below the fluid mud layer for which $\rho_c < \rho < \rho_s$ shall be referred to as the partially consolidated mud, which remains immobile.

Now superimpose a jet discharge across the lutocline surface at $z = m$. Assume this jet has operated a sufficient length of time for all transient pressure disturbances to propagate into the far field (the hydrostatic assumption). Therefore, along the axis of the jet we may assume a one-dimensional steady state in which upward diffusive mass fluxes due to the turbulent eddy transport of the jet are balanced by downward advective mass fluxes due to the settling of the suspended sediment under the influence of gravity, or:

$$\frac{\partial^2 \rho}{\partial z^2} = \frac{\omega_0}{\epsilon} \frac{\partial \rho}{\partial z} \quad (3)$$

Here ϵ is the eddy mass diffusivity which may be approximated from mixing length theory as:

$$\epsilon = \frac{ak_0\sqrt{\tau}}{\sqrt{\rho_m}}(z + z_0) \quad (4)$$

where k_0 is Von Karman's constant; τ is the jet induced shear stress; and a is the Peclet number, equal to a ratio of the mass diffusivity to the momentum diffusivity.

Equation (3) is solved by successive integrations subject to the following boundary conditions: (1) the jet will not entrain sediment from the fluid mud layer unless the applied jet stress, τ , exceeds the cohesive yield stress, τ_c , or $\rho = \rho_c$, at $z = m$ for $\tau < \tau_c$; and (2) $\rho = \rho_t$ at $z = h$ for $\tau \geq \tau_c$. A solution to Eq. (3) in the domain between the lutocline and the free surface subject to these boundary conditions is:

$$\rho = \frac{9a^2k_0^2(\tau - \tau_c)}{\omega_0^2 \log^2[(z + z_0)/2z_0]} + \rho_c \exp \left[\frac{(z-m)}{(h-m)} \log \frac{\rho_t}{\rho_c} \right] \quad (5)$$

for $\tau \geq \tau_c$ and $m \leq z \leq h$

The first term on the right hand side of Eq. (5) is the disturbance to the sediment component density profile induced along the axis of the jet, while the second term represents the ambient density profile above the lutocline. The sediment component density above the lutocline is found to grow in direct proportion to the excess applied jet shear stress relative to the cohesive yield stress of the fluid mud layer, while decreasing with increasing particle size or increasing settling velocity.

Fine sediment deposition at the consolidated muddy bottom, $z = 0$ in Fig. 3, is directly proportional to the abundance of suspended sediment in the fluid mud layer, Ariathurai and Krone (1976) and Cole and Miles (1983). This abundance is determined by the net mass fluxes across the lutocline at $z = m$. The flux of suspended sediment entering the fluid mud layer due to settling under gravity is $-\rho\omega_0$. These downward directed settling fluxes are the predominant mass fluxes which occur across the lutocline in a dredged estuary. However in the presence of a turbulent jet, vertical transport due to eddy diffusion may become important, especially along strong density gradients in the neighborhood of the lutocline. The net of settling fluxes and diffusive fluxes across the lutocline determines the rate of change of suspended sediment in the fluid mud layer. However there is only a finite probability $p(0,1)$, that this suspended sediment will actually stick to the bed at $z = 0$ and consolidate to some ultimate saturation density, ρ_s , see Krone (1962). Therefore the deposition flux, D , may be written:

$$D = \frac{-K_s \rho_c g + p(0,1) \left[\rho_c \omega_0 + \epsilon \frac{\partial \rho}{\partial z} \Big|_{z=m} \right]}{(1 - \rho_c / \rho_s)} \quad (6)$$

In Eq. (6) positive values of D correspond to deposition while negative values indicate entrainment of suspended sediment from the fluid mud layer into the floc layer and fluid above. In the absence of jet induced shear stresses, ($\tau < \tau_c$ as in control areas) the diffusive flux term in Eq. (6) is negligible and the deposition flux becomes a positive value controlled by local settling fluxes, $\rho_c \omega_0$. If, however, jet induced shear stresses become large, $\tau \geq \tau_c$, then a large negative diffusive flux term arises in Eq. (6) which we refer to as the jet entrainment flux, E_j , or:

$$E_j = \frac{-K_s \rho_c g + p(0,1) \left\{ -\operatorname{Re} \left[\frac{9a^3 k_0^3 (\tau - \tau_c)^{3/2} (m + z_0)}{\omega_0^2 z_0 \sqrt{\rho_m}} \log \left(\frac{m + z_0}{2z_0} \right) \right] \right\}}{(1 - \rho_c / \rho_s)} \quad (7)$$

where Re is the real part operator. Hence there is no jet entrainment flux when $\tau < \tau_c$. From Eq. (7) it is clear that the variation of the jet entrainment flux

along the jet axis depends decisively on the decay rate of the applied jet shear stress with distance from the jet discharge, and upon the cohesive yield stress of the fluid mud layer.

Applied Jet Shear Stress

A laboratory experiment was conducted in which a turbulent jet was discharged across a plain immobile bottom imbedded with a flush mounted shear stress probe. The position of the flush mounted shear stress probe was varied along the axis of the jet. The initial discharge velocity of the jet, U_0 was varied for several different jet diameters, d . The results were found through regression analysis to produce a systematic power law relation between the applied jet shear stress τ , and the distance, x , along the jet axis from the jet discharge. These results are plotted in Fig. 4. The regression line for the data was found to obey the following:

$$\tau = 120\rho_m U_0^2 \left(\frac{U_0 d}{\nu}\right)^{-0.4} \left(\frac{d}{x}\right)^{2.4} \quad (8)$$

We find that the applied jet shear strength decays as the -2.4 power of the distance, x , from the jet discharge point. The flush mounted shear stress probe indicated that lines of constant stress resemble teardrops as diagrammed in

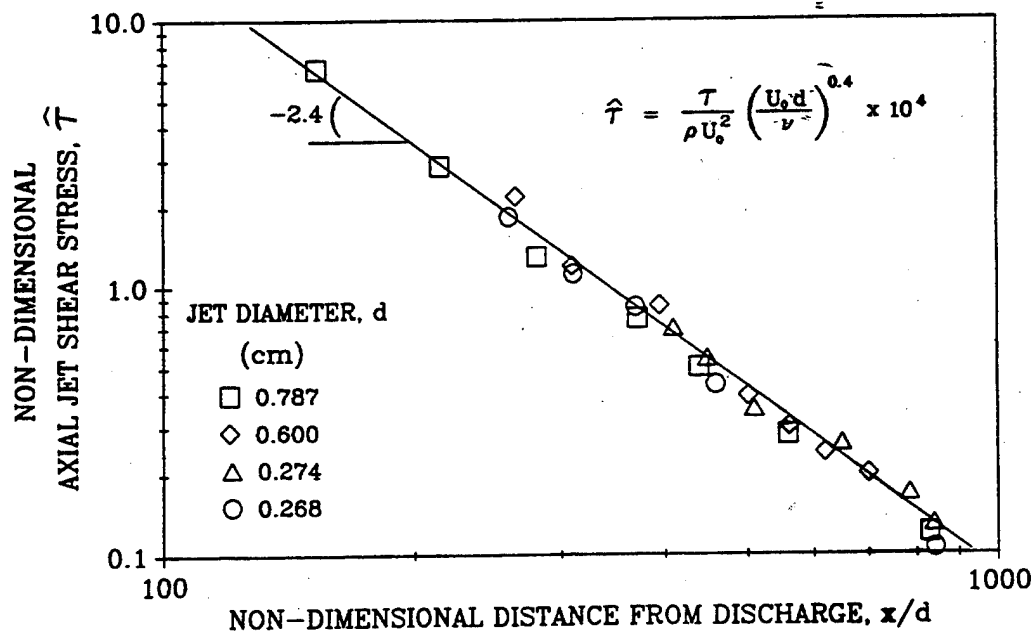


Figure 4. Extinction rate of applied jet shear stress measured on laboratory scales.

Fig. 3. The maximum width of each teardrop occurred at roughly 2/3 the maximum range from the jet for any given contour of constant stress. The width of the teardrop was found to be approximately 1/3 the maximum range of the shear stress contour. Our focus herein is along the jet axis for which the maximum range, X_m , for any given contour of constant applied jet shear stress, τ , is given by:

$$X_m = d \left[\frac{\tau R_j^{0.4}}{120 \rho_m U_0^2} \right]^{-0.417} \quad (9)$$

where R_j is the jet Reynolds number = $U_0 d / \nu$.

In Fig. 5, plots of Eq. (9) show that the maximum axial range of any given stress contour increases either with increasing axial jet discharge velocity or increasing jet diameter. In other words, X_m grows with increasing jet flow rate, $U_0 \pi d^2 / 4$. Equation (7) indicates that the particular value of applied stress, τ , must exceed the cohesive yield stress, τ_c , in order to effect deposition out to X_m . Consequently we find in Fig. 5 that X_m decreases for any given selection of U and d with increasing strength of the fluid mud.

Cohesive Yield Stress of the Fluid Mud Layer

Because the steady state jet plume must induce motion of the fluid mud layer to effect entrainment, the decisive question is whether the applied jet shear stress exceeds the cohesive yield stress in the fluid mud layer. To assess the strength of the fluid mud, grab samples were gathered by diver in the neighborhood of the consolidated bottom. Hydrometer analysis determined that the sediments in the fluid mud layer were 25% clay, 55% silt and 20% fine sand with an organic content of 4%. X-ray diffraction revealed that the predominant minerals present in the fluid mud layer were montmorillonite, illite, and kaolinite. The cohesive yield stress was determined with a Brookfield synchro-electric viscometer equipped with a special UL adapter, (Brookfield Engineering Laboratories Inc, Stoughton, MA). The usefulness of the instrument in predicting this behavior of cohesive sediments both in the field and in the laboratory has been described in detail by Faas (1990). The coaxial cylinder geometry of the UL adapter provides greater sensitivity for low viscosity suspensions and the instrument is accurate to within 1% of the full scale reading.

The grab samples from the fluid mud layer were washed with deionized water to remove sea salts, followed by screening to remove pieces of debris, shells, etc. The samples were then sieved through a 62 micron sieve to separate the fine fraction from the coarse fraction. Subsequently the suspension was agitated thoroughly to break up any large clumps or flocs. The suspension was then

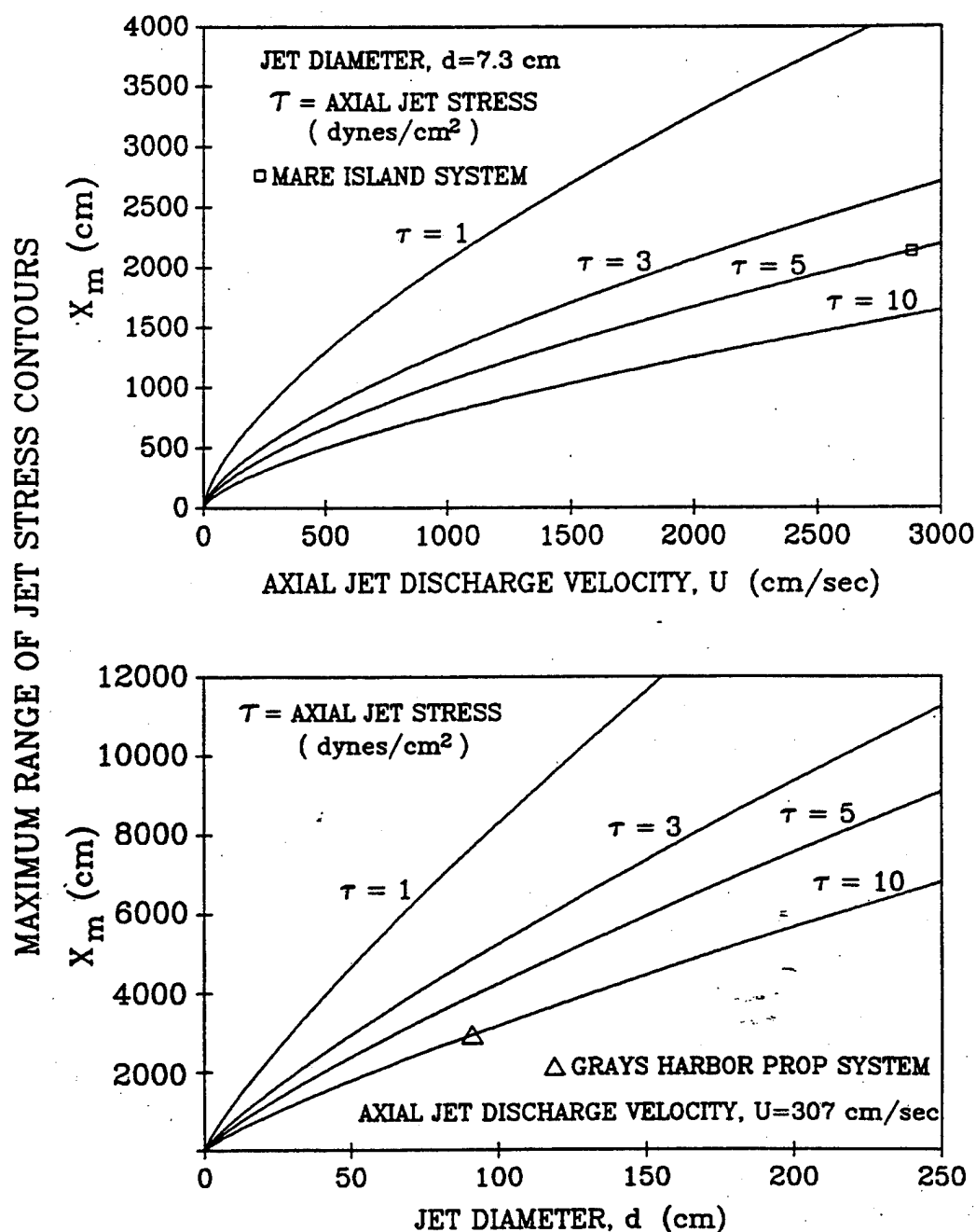


Figure 5. Dependence of the maximum range of applied jet shear stress upon: a) axial discharge velocity (jet diameter/ the Mare Island pump based system); and b) jet diameter (axial jet discharge velocity/ the propeller based Grays Harbor jet system). Symbols indicate design points for prototype tests shown in Fig. 8.

sheared in the Brookfield viscometer. The initial reading was taken at zero salinity. Subsequent readings were taken at increasing salinities of up to 30 o/oo. Three separate runs were made on the same sediment suspension and 3 or 4 viscometer readings were taken for each increment of salinity. There were no variations in the measured values for all three runs thereby assuring the accuracy of the viscometer to produce data of good quality.

Two sets of experiments were conducted. One consisted of analyzing the yield stress behavior of the natural sediment sample and the other measured the yield stress after removing the organic matter. The organic matter was removed by treating the sediment sample with 30% hydrogen peroxide solution. The sediment component density was then calculated from the ratio of the oven-dried weight of the sample to the total volume of the sediment suspension.

The yield stress was measured at a fixed sediment concentration while the salinity was varied in increments of 5 o/oo. The experiments were then repeated for varying sediment concentrations. The results show that as the salinity is increased from 0 to 5 o/oo, there is a sharp increase in cohesive yield stress followed by a gradual increase beyond 5 o/oo, see Fig. 6. This result is in agreement with the results of previous investigators in the lower salinity range, see Edzwald et al. (1974), Gibbs (1983). However, even after 5 o/oo, the yield stress does not level off but continues to increase at higher salinities. This result implies that the pump intakes should be placed as close to the surface as possible, to draw off the lens of low salinity surface water. The resulting reduction in yield stress within the low salinity jet plume would then, by Eq. (9), maximize the range of deposition reduction.

Several runs of experiments were conducted in the sediment concentration range of 10 grams/liter to 75 grams/liter. This range is representative of the seasonal variations in fluid mud layers at the prototype test sites at Mare Island, CA and Grays Harbor, WA, see Jenkins et al. (1980). The values of yield stress obtained were 0.85 dynes/cm² at 10 grams/liter and zero salinity up to 5 dynes/cm² at 75 grams/liter and 30 o/oo. The yield stress in Fig. 6 for the sediment concentration of 75 grams/liter rises from 1.5 dynes/cm² at zero salinity to 4.26 dynes/cm² at 3 o/oo and finally to 5.06 dynes/cm² at 30 o/oo. There is a 19% increase in yield stress from 3 o/oo to 30 o/oo. Similarly, other runs show a percentage increase of 15 to 20 % as the salinity increases from 3 to 30 o/oo. The sediment without the organic matter (Fig. 6) shows the same trend as the natural sediments, indicating that the organic matter is not playing a significant role in affecting the yield stress increase due to the effects of salinity.

Jet Experiments in the Field

Jet experiments were conducted at three west coast sites: (1) Mare Island, California; (2) Terminal 4, Grays Harbor, Washington; (3) Terminal 2, Grays Harbor Washington. The Mare Island jet system was a pump based system

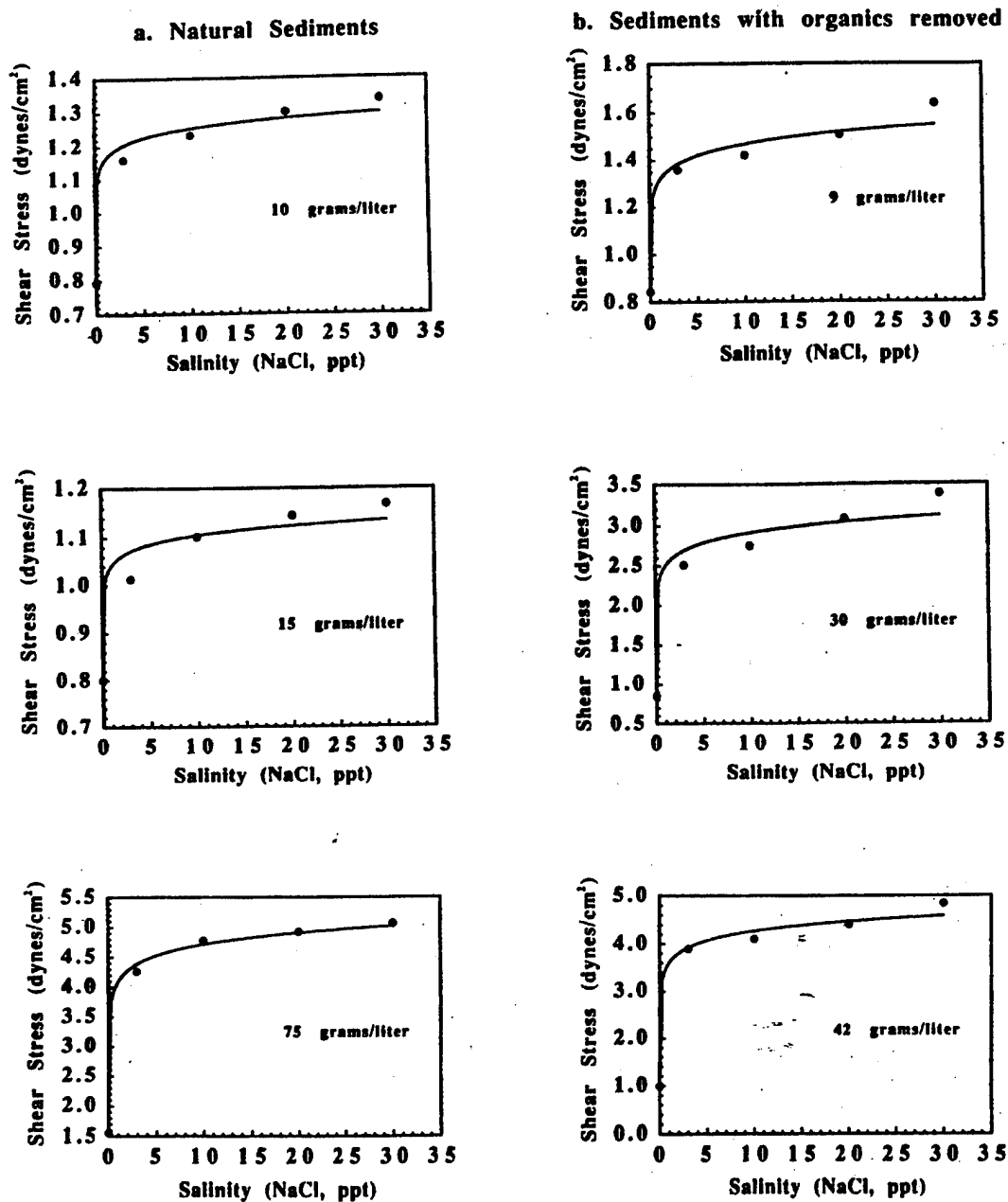


Figure 6. Cohesive yield stress dependence upon salinity and concentration. Right hand column figures are based upon sediment samples with the organics removed. Left hand column figures are based upon natural sediments with the organic content intact.

comprised of ten jets at 914 cm spacings, each with a diameter of 7.3 cm and a discharge velocity of 2,879 cm/sec. Two distinctly different jetting systems were tested at Grays Harbor, Washington. The Terminal 4 system was pump based, as shown in Fig. 1, comprised of 24 jets at 914 cm spacings, each with a diameter of 22.2 cm and a discharge velocity of 2,207 cm/sec. The Terminal

2 system was a propeller based system as diagrammed in Fig. 2 comprised of a single discharge with a 91.4 cm diameter and a 307 cm/sec discharge velocity.

Based upon cohesive yield stress results like those in Fig. 6, the Mare Island system was designed to produce an applied shear stress of 5 dynes/cm² out to a maximum range of 2,000 cm, to allow for seasonal maximums in suspended sediment. The settling velocity of the flocs in the fluid mud layer was determined to be 0.035 cm/sec with typical excess densities in the fluid mud layer of 0.075 g/cm³. The saturation density of the consolidated muds at Mare Island was determined to be 1.1 g/cm³. Dynamic shear stress analyses at Grays Harbor revealed significantly stronger fluid mud layers as thick as 150 cm with cohesive yield stresses as high as 10 dynes/cm². The flocs of these fluid mud layers were larger with median settling velocities of 0.05 cm/sec. Typical excess densities in the fluid mud layer at Grays Harbor were found to be 0.1 g/cm³ with saturated densities for the consolidated material on the order of 1.1 g/cm³. Accordingly, the design applied shear stress for both the Grays Harbor jetting systems was increased to 10 dynes/cm² out to a maximum range of 3,000 cm. The design point for the Mare Island system is indicated in Fig. 5a while the design point for the propeller based Grays Harbor system is shown in Fig. 5b.

Fathometer surveys were conducted over a 2 month period at Mare Island and over 2 separate 3 month periods at Grays Harbor. Comparisons between the local depths in the jetting areas to those in control areas were used to calculate the jet entrainment flux by the following:

$$E_j = \rho_s \frac{\eta_{\text{jet}} - \eta_{\text{control}}}{\Delta t} \approx D_{\text{jet}} - D_{\text{control}} \quad (10)$$

where η was the vertical position of the immobile bed as determined from 40 kHz fathometer soundings in the test areas and control areas, respectively. The jet entrainment flux is a measure of the deposition flux which did not occur due to the action of the jet stress over a period of time, Δt . Figure 7 shows a bathymetry contour plot from the survey of the Terminal 4 pump based Grays Harbor system conducted between March 1987 and June 1987. These soundings were conducted along 2,000 feet of waterfront, one half of which (along the upstream portion) served as a control area. Seven hundred feet of the downstream portion was influenced by a 700 ft long reach of 24 jets. It is clear from these bathymetry surveys that the jets had a pronounced effect on preventing deposition. The entire 610 meters of waterfront was dredged to -11.6 meters MLLW just before the activation of the jetting systems in March 1987. By June 1987 the control area had shoaled to between -7 and -8 MLLW while major portions of the jet test area inside 30 meters were maintained at the original dredged depths. Surprisingly, deposition was retarded as far out as 42 meters from the jet discharge nozzles.

Measured jet entrainment fluxes from the average depths over control areas and jet test areas according to Eq. (10) are plotted in Fig. 8 and compared against entrainment flux calculations based on Eq. (7) for the respective jet and

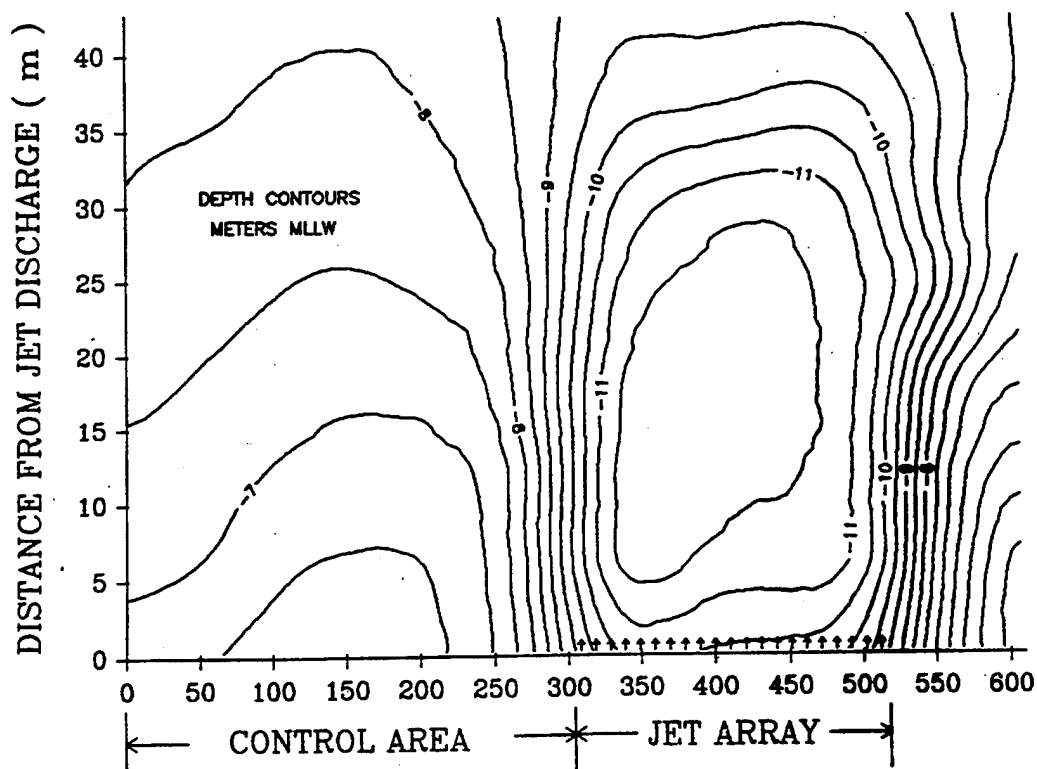


Figure 7. Bathymetry survey at the end of the test period of the pump based Grays Harbor jet system conducted between March 1987 and June 1987. Bathymetry contours are based upon echo soundings of a 40 kHz fathometer. Ebb flow proceeds from left to right with the control area situated on the upstream side during jet operations in ebbing flow arrows indicate the position of individual jets.

sediment properties listed. The value for the probability factor, $p(0,1)$, was adjusted to achieve best fit between the calculations and the data. Even then, it was necessary to base the calculations on cohesive yield stress values less than the design values in order to account for the non zero entrainment fluxes measured at great distances from the discharge points. The entrainment flux data suggests that the cohesive yield stress values during the tests were effectively only about 1 and 4 dynes/ cm^2 at MINSY and Grays Harbor respectively. However, these values are consistent with the results of Fig. 6, for artificially depressed salinities which would arise in the field from the jet discharges which derive their drive water from intakes near the surface.

Conclusion

The results indicate that deposition of fine grain sediments may be controlled through the semi-diurnal application of hydrostatic jets producing applied shear

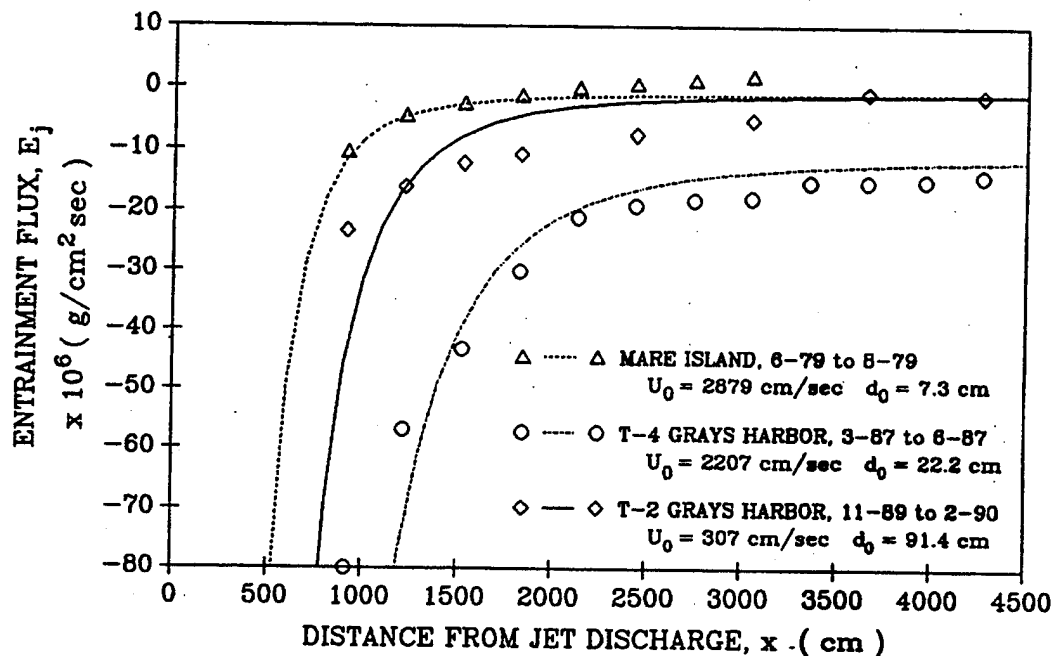


Figure 8. Measured deposition fluxes derived from spatial averages of fathometer surveys as compared with calculated deposition fluxes based on Eq. (7). The dotted curve represents the theoretical entrainment expected from the pump based jet array system at Mare Island Naval Shipyard using the following parameterization: $p = 0.001$, $z_0 = 1 \text{ cm}$, $m = 10 \text{ cm}$, and $a = 0.002$. The solid curve is the theoretical entrainment expected from the turbine chimney unit at Terminal 2, of the Port of Grays Harbor, WA, using the following values: $p = 0.0000005$, $z_0 = 10 \text{ cm}$, $m = 150 \text{ cm}$, and $a = 0.02$. The dashed-dotted curve corresponds to the theoretical predictions of the performance of the pump based jet array system at Terminal 4, the Port of Grays Harbor, WA, with parameterization as follows: $p = 0.0002$, $z_0 = 10 \text{ cm}$, $m = 150 \text{ cm}$, and $a = 0.0036$.

stresses in excess of the cohesive yield stress of the fluid mud layer. This may be accomplished by either of two means: (1) application of high velocity jets or (2) application of large diameter jets. By either approach the effect of controlling deposition thru jet entrainment in the far field is maximized by maximizing the total jet flow rate. This suggests that the total eddy momentum content of the jet discharge is the limiting factor in facilitating entrainment and hence controlling deposition. In other words the turbulent momentum of the jet discharge is progressively diluted with increasing distance from the jet discharge point. At some maximum range, the eddy momentum of the jet discharge is diluted to such an extent that it is incapable of entraining sediment from the fluid mud layer across the lutocline interface. The unexpected persistence of this entrainment in the far field of low salinity jets also suggests that the jet salinity

may exert a modifying effect on the cohesive yield stress of the fluid mud, rendering it more susceptible to eddy transport across the lutocline.

Acknowledgements

The authors wish to thank Dr. James A. Bailard for his many contributions to this work throughout its duration. We further wish to thank Mr. Joseph Sparks of the Mare Island divers for numerous contributions of effort and mechanical innovation in the Mare Island jet array design and maintenance. This work was supported in part by the Office of Naval Research Ocean Engineering Division, Code 1121.

References

- Ariathurai, R., and R.B. Krone, Finite element model of cohesive sediment transport, *J. Hydraul. Div. ASCE*, 102(HY3), 323-338, 1976.
- Bailard, J.A., and S.A. Jenkins, Method and apparatus for the active prevention of sedimentation in harbors and waterways, U.S. Patent #4,957,392, 1990.
- Cole, P., and G.V. Miles, Two-dimensional model of mud transport. *J. Hydraul. Eng. ASCE*, 109(1), 1-12, 1983.
- Dyer, K.R., *Coastal and Estuarine Sediment Dynamics*, 342 pp, Wiley, New York, 1985.
- Edzwald, J.K., J.B. Church, and C.R. O'Melia, Coagulation in estuaries, *Envir. Sci. and Tech.* 8, 58-63, 1974.
- Faas, R.W., A portable rotational viscometer for field and laboratory analysis, *J. Coast. Res.* 735-738, 1990.
- Fugita, H., *Mathematical Theory of Sedimentation Analysis*, 315 pp, Academic, York, 1962.
- Gibbs, R.J., Coagulation rates of clay minerals and natural sediments, *J. Sedimentary Petrology*, 53, 1193-1203, 1983.
- Heinz, R.A., J.A. Bailard, and S.A. Jenkins, Water jets fight silt, *Civil Engineering*, 59(1), 54-58, 1989.

Jenkins, S.A., D.L. Inman and J.A. Bailard, Opening and maintaining tidal lagoons and estuaries, *Proc. 7th Int Coastal Eng Conf*, Amer. Soc. Civil Eng, 2, 1528-1547, 1980.

Jenkins, S.A. and J.A. Bailard, Anti-sedimentation system for harbors, *World Wide Shipping*, 52(1), 70-75, 1989.

Krone, R.B., *Flume Studies of the Transport of Sediment in Estuarial Shoaling Processes*, Final report, Hydraulics Engineering Laboratory and Sanitary Engineering Research Laboratory, University of California, Berkeley, 1962.

Krone, R.B., Aggregation of suspended particles in estuaries. *In: Estuarine Transport, Process*, B. Kjerfve, (ed.). University of South Carolina Press, Columbia, SC, 177-190, 1978.

Mehta, A.J., On estuarine cohesive sediment suspension behavior, *J. Geophys. Res.*, 94, (C10), 14,303-14,314, 1989.

Mehta, A.J., and E. Partheniades, An investigation of the depositional properties of flocculated fine sediments. *J. Hydraul. Res.* 13(4), 361-381, 1975.

APPENDIX C: U. S. PATENT #4,957,392

**METHOD AND APPARATUS FOR THE ACTIVE PREVENTION
OF SEDIMENTATION IN HARBORS AND WATERWAYS**

by

JAMES A BAILARD & SCOTT A. JENKINS

[54] METHOD AND APPARATUS FOR THE ACTIVE PREVENTION OF SEDIMENTATION IN HARBORS AND WATERWAYS

[76] Inventors: James A. Bailard, 1150 Bailard Ave., Carpinteria, Calif. 93013; Scott A. Jenkins, 14765 Kalapana St., Poway, Calif. 92064

[21] Appl. No.: 344,079

[22] Filed: Apr. 27, 1989

[51] Int. CL³ E02F 3/88; E02B 3/04; E02B 5/28

[52] U.S. CL 405/73; 405/22; 405/74; 37/75; 37/78; 114/55

[58] Field of Search 405/21, 22, 52, 62, 405/73, 74, 79, 80; 37/75, 77, 78, 79; 114/55

[56] References Cited

U.S. PATENT DOCUMENTS

3,109,288	11/1963	Gross	405/61
3,449,915	6/1969	Cummings	405/74
3,683,627	8/1972	Girden	405/52
3,964,184	6/1976	Mathieu	37/78 X
4,073,078	2/1978	Leitz	37/77
4,439,060	3/1984	Liscio	405/52 X
4,548,525	10/1985	Priebe	405/52

4,819,347 4/1989 Lofgren 37/78

FOREIGN PATENT DOCUMENTS

809175 7/1951 Fed. Rep. of Germany 37/77

446073 3/1949 Italy 37/78

412356 7/1974 U.S.S.R. 37/78

Primary Examiner—Randolph A. Reese

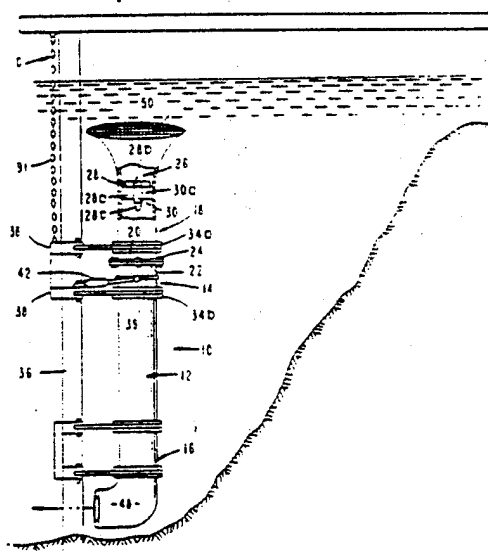
Assistant Examiner—John A. Ricci

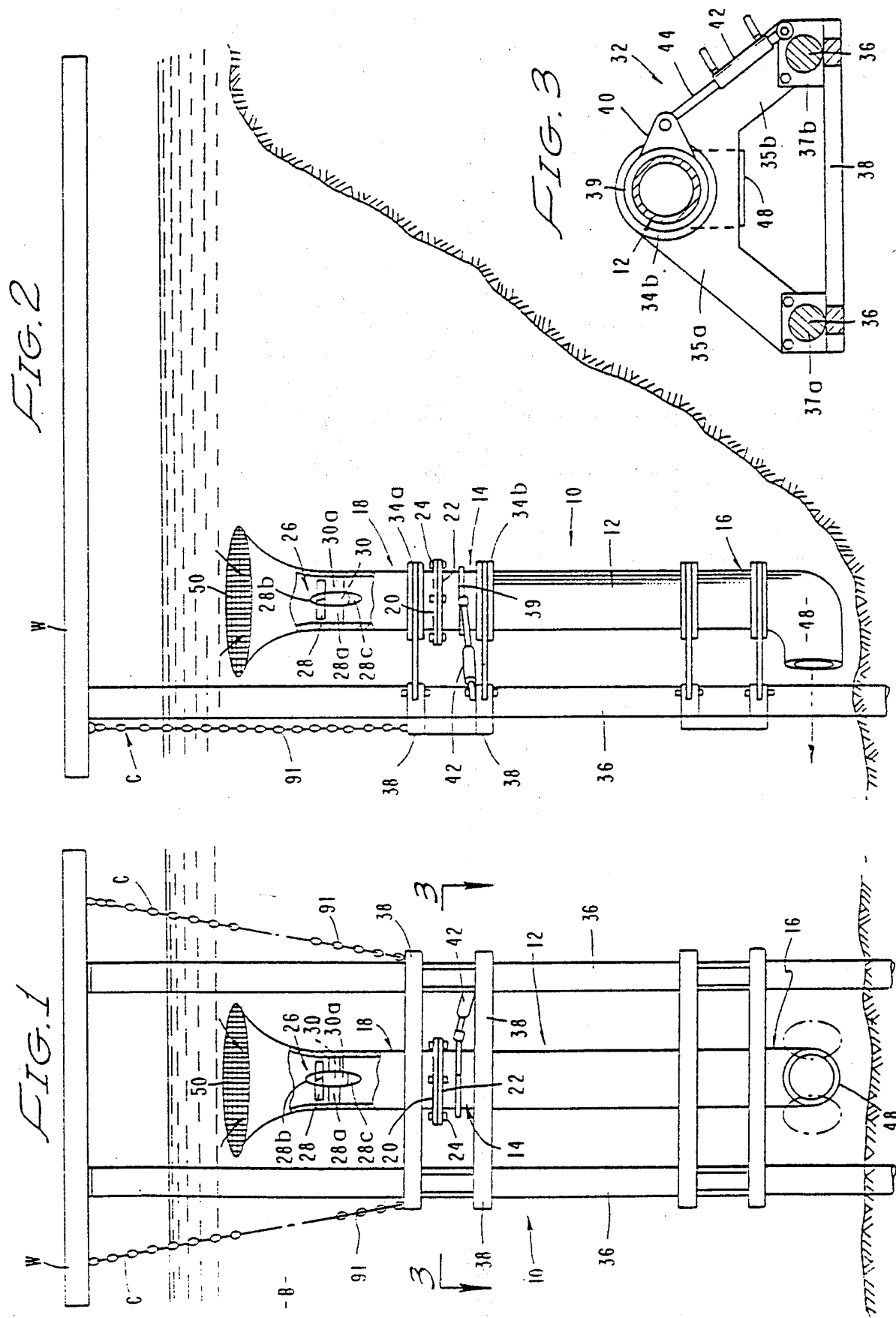
Attorney, Agent, or Firm—James E. Brunton

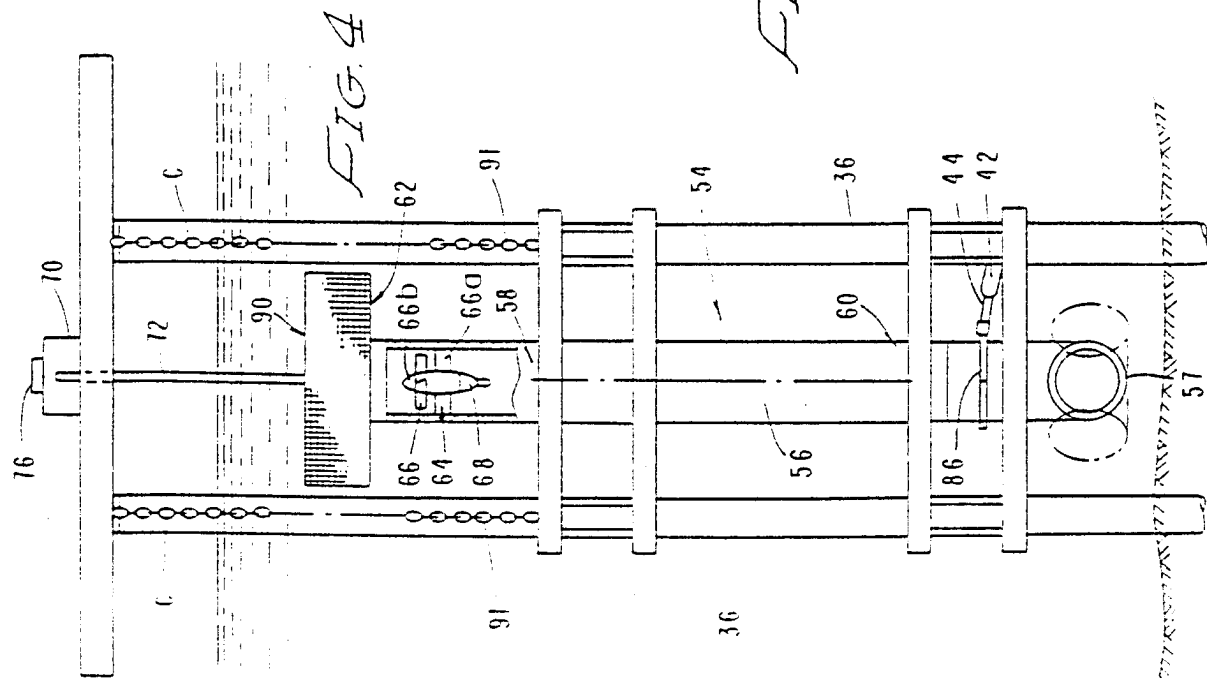
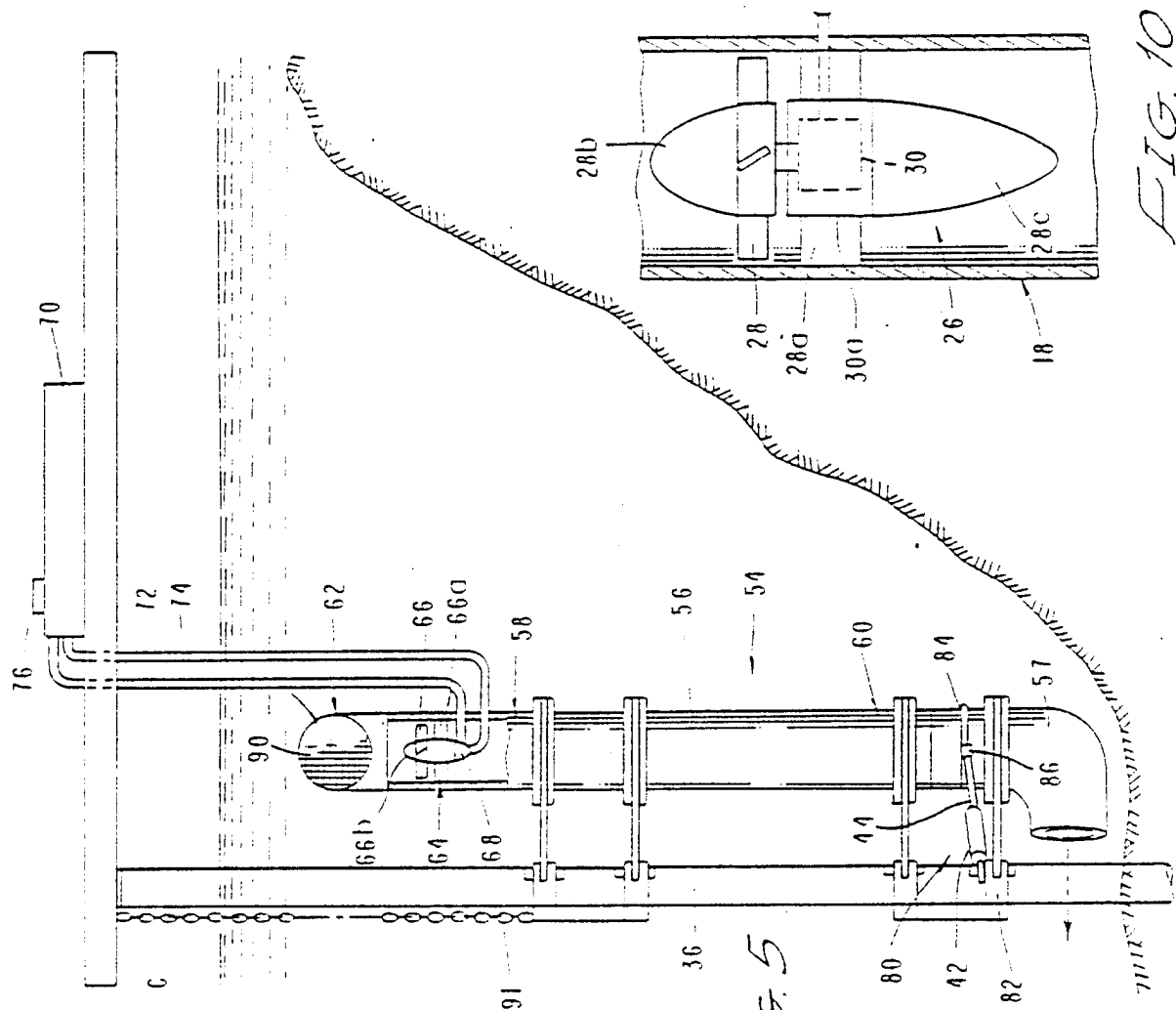
[57] ABSTRACT

An apparatus for preventing sedimentation buildup in waterways having a current, the apparatus being submersible at a location proximate the edge of the waterway and adapted to produce a scour pattern of predetermined configuration. The apparatus includes an elongated, substantially vertical tubular member having an inlet assembly connected proximate the upper end of the tubular member; a turbine fan unit mounted interiorly of the inlet assembly for controllably drawing water into the apparatus; and a discharge assembly connected to the tubular member proximate its lower end for directing the flow of water outwardly from the tubular member in generally horizontal direction at an optimum flow rate.

3 Claims, 4 Drawing Sheets







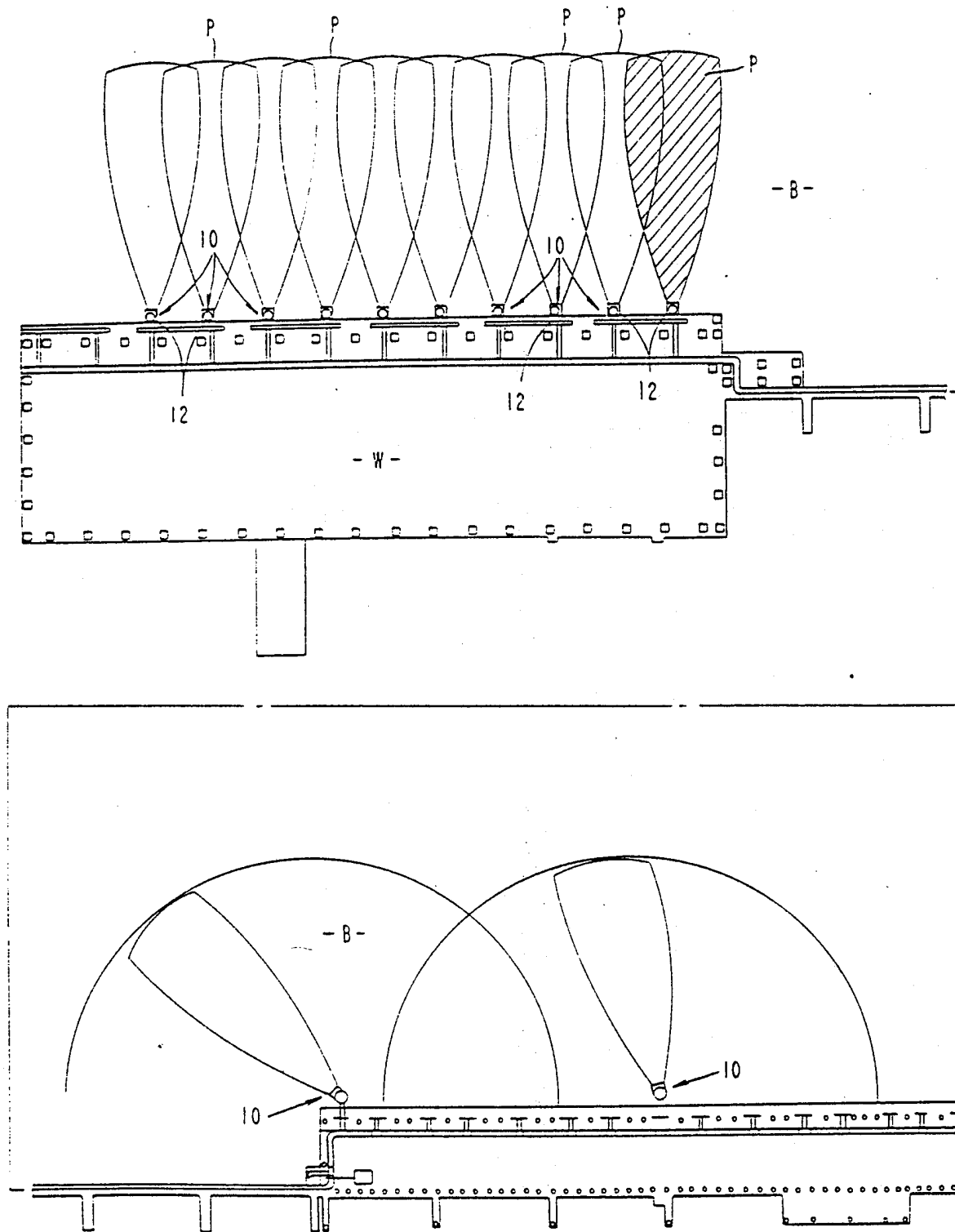


FIG. 6

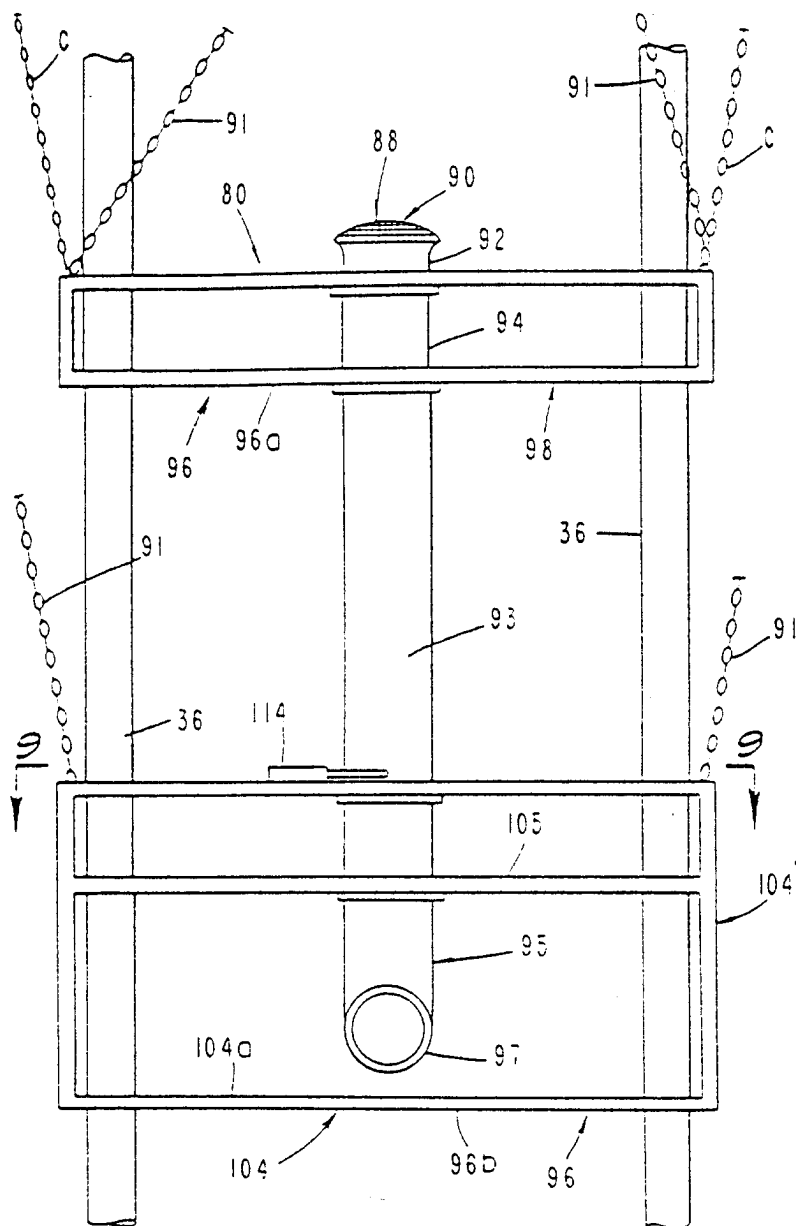


FIG. 7

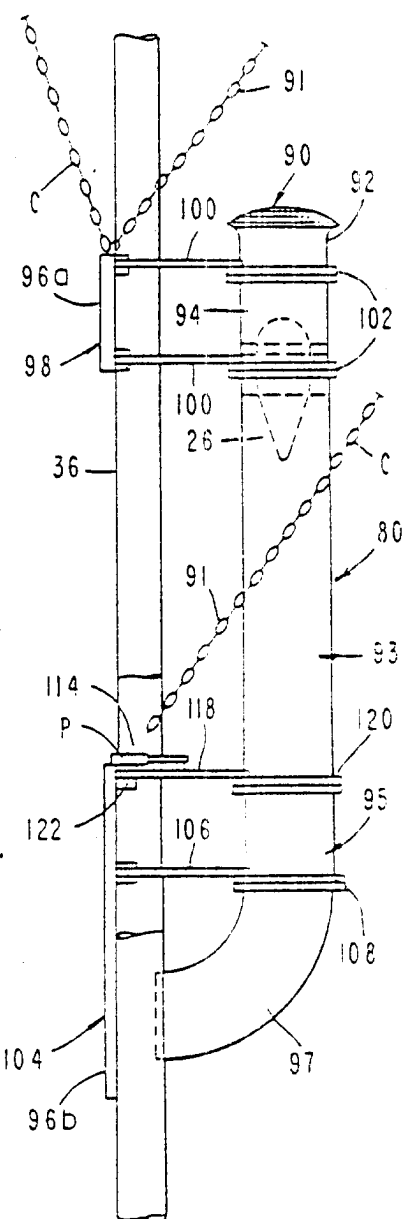


FIG. 8

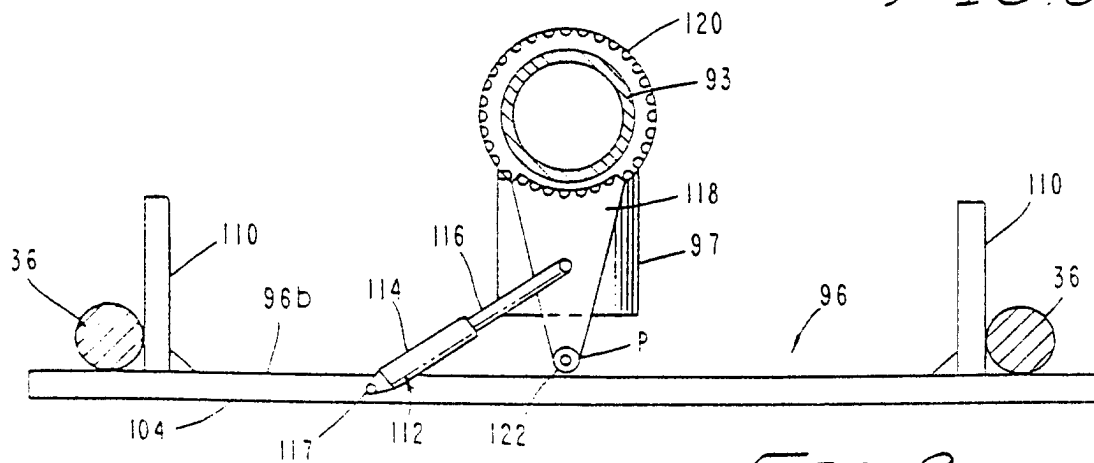


FIG. 9

METHOD AND APPARATUS FOR THE ACTIVE PREVENTION OF SEDIMENTATION IN HARBORS AND WATERWAYS

BACKGROUND OF THE INVENTION

1. Field of the Invention

The present invention relates generally to a method and apparatus for maintaining sufficient water depth in harbors and waterways to accommodate deep draft vessels. More particularly, the invention concerns a method and apparatus for accomplishing daily resuspension of newly deposited sediments using a submerged, turbulent water discharge, thereby eliminating the need for periodic dredging and its associated adverse environmental impacts.

2. Discussion of the Invention

Introduction - Most present day harbors are located in bays and estuaries which formed at the mouths of major rivers. These harbors have natural water depths of about 20 feet. At this depth, ebbing water currents are sufficiently intense to carry sediments, introduced by the rivers and streams, through the harbor and out to the ocean.

Although 20 foot water depths were adequate for early sailing vessels, the introduction of deeper draft vessels around the turn of the century created the need for greater water depths. Bucket and suction dredges were introduced to deepen the navigation channels and berthing areas. With these increased depths came the need for continual maintenance dredging. This process of progressive deepening and subsequent maintenance dredging continues to this day. For example, today's major ports and harbors have water depths of 40 feet or more, reflecting the massive size of modern deep draft tankers and bulk carriers.

Increasing the depth of channels and berthing areas reduces the scouring action of natural water currents. As a result, these quiet water areas have become natural collection points for sediments which in the past would be transported through the area and out to sea. Furthermore, the deeper one dredges these areas, the faster they fill in. As a result, maintenance dredging has become an increasingly burdensome problem.

After 150 years of dredging, dredged material disposal areas are becoming scarce. The problem has been compounded by recent environmental regulations which severely limit available options for dredged material disposal. These regulations came about through the recognition that harbor silts and clays have a proclivity for absorbing heavy metals and other toxins. As a result, the cost of dredging has risen sharply in recent years.

Conventional dredging techniques focus on the efficient removal of consolidated bottom sediments. Conventional dredges achieve their economies of scale by removing large volumes of sediment relatively infrequently. As a result, harbor channels and berthing areas are typically dredged every year or two. In between dredgings, sedimentation continues to occur, so that towards the end of a dredging cycle, ship operators are forced to carry only a partial load to avoid grounding.

The shortcomings associated with conventional dredging methods have led to the search for alternative methods of maintaining adequate water depths. One approach has been to interrupt the sedimentation process, either by preventing the influx of sediment to, or the deposition of sediment within a harbor or waterway

area. This approach, termed sedimentation control, has proven most effective in harbor berthing areas. An important benefit of the sedimentation control approach is that the costly dredge material disposal problem is avoided.

Another prior art sedimentation control method involves the use of the scour jet array. This system typically consists of a series of near-bottom water jets positioned along the face of a wharf or dock. The jet array is powered by a high pressure water pump, which discharges to a common manifold pipe. The jets are connected to the manifold pipe by a series of valves and hoses.

Although scour jet array systems are generally effective in preventing unwanted sedimentation, they are quite expensive to build and operate. Tests have shown that the most efficient method of producing a water jet with a sizable range of scour is to use a high flow rate, low velocity discharge. High flow rates, however, require large pumps and pipes, thereby increasing the cost of the scour jet array system.

An alternative method of generating a high flow rate, low velocity discharge is to use a motor driven propeller. A number of agitation dredging and sedimentation control systems have been built using open mounted, near-bottom propellers to produce the required scour flow. One type of prior art propeller system is described in U.S. Pat. No. 3,449,915, issued to T. E. Cummings.

The prior art propeller type systems typically suffer from several fundamental problems: (1) the open propeller design is subject to fouling or damage by waterborne debris; (2) the unprotected propeller can be buried by sediment avalanching from adjacent undredged banks; (3) the propeller type systems utilize high salinity (and, therefore, less efficient) bottom water in producing a turbulent scour plume; and, (4) the exposed propeller poses a hazard to divers and marine mammals.

The method and apparatus of the present invention overcomes the drawbacks of prior art systems through the use of an array of turbine chimney scour units of highly novel design. Compared to conventional prior art dredging methods, the turbine chimney scour system of the present invention is less costly and considerably less damaging to environmental water quality. By continually preventing sediment deposition, the turbine chimney scour system avoids the costly problem of dredged material disposal. Additionally, reducing the residence time of the resuspended sediments minimizes the very serious environmental problem of adsorption and release of heavy metals and other toxins. The turbine chimney scour system also minimizes the impact to benthic organisms which are periodically destroyed by conventional dredging methods.

The turbine chimney scour system of the present invention is also considerably more effective and less environmentally damaging than the prior art agitation dredging methods. The prior art agitation dredging methods typically function by remobilizing consolidated bottom sediments, allowing ambient currents to carry them from the area. For example, one common prior art method utilizes a specially-designed vessel to suck sediment off the bottom and discharge it horizontally across the water surface. The objective is to raise the material high enough within the water column so that it is carried a significant distance downstream by ebbing currents. Agitation dredging is typically performed only once or twice a year. The lengthy period

of time between dredging is critical, for it allows the sediments to consolidate, greatly increasing their shear strength and resistance to resuspension. As a result, agitation dredging methods are not particularly effective, since they fail to fully resuspend the consolidated bottom sediments, causing them to deposit a short distance downcurrent.

In contrast to agitation dredging, the apparatus of the present invention is typically activated on a daily basis, fully resuspending the thin layer of newly deposited sediment. This provides three important benefits: (1) water turbidity is less because less sediment is resuspended during each operation; (2) transport distances are greater because the sediment is fully resuspended; and, (3) fewer toxins are released because the bottom sediments have a negligible residence time before being resuspended.

Compared with the pump based prior art scour jet array systems, the turbine chimney scour system of the present invention is less costly and considerably more efficient. Cost savings accrue primarily through the use of individual turbine fan units to produce the required jet discharge. This eliminates the need for a long and costly large diameter piping system. Moreover, by utilizing a high flow rate/low velocity discharge, the turbine chimney scour system requires about 1/10th the input power to achieve the same scour performance.

The turbine chimney scour system of the present invention is readily distinguishable from and clearly superior to the prior art open propeller scouring system for several reasons. In the first place, the turbine fan is a different and intrinsically more efficient propulsion method than an exposed propeller. The ducting around the turbine fan acts to produce a higher discharge velocity per unit power input. Enclosing the propulsion device, also, protects divers and unsuspecting marine mammals from accidental injury.

Secondly, the ability to readily adjust the intake location of the apparatus allows low salinity, oxygen rich surface water to be used for scouring. Tests have shown that low salinity water reduces the cohesive strength of the bottom sediments and is more effective in resuspending fine bottom sediments. Additionally, the higher oxygen content of the ingested surface water provides improved water quality near the bottom, which tends to be anaerobic with consequently high bacterial levels. The combination chimney/elbow configuration of the apparatus, also, provides excellent protection of the turbine fan unit from sediment avalanching of adjacent mud banks. Field tests of propeller based scour jet array systems have shown this to be a serious problem.

Another advantage of the apparatus of the invention resides in the novel design of the screened intake which helps to prevent damage to the propulsion unit from waterborne debris. The design, also, prevents the ingestion of fish during operation. The latter is an important permitting consideration in areas having significant marine fisheries (e.g. the salmon fishery in the Pacific Northwest). As an added feature, the flow from the turbine fan can be briefly reversed following operation, helping to clean the screen of any accumulated debris. Still another advantage of the apparatus of the invention is the gravity support frame which permits rapid installation and recovery of the turbine chimney scour units for routine maintenance.

SUMMARY OF THE INVENTION

It is an object of the present invention to provide an efficient, cost effective and environmentally acceptable method and apparatus for preventing sediment build-up in harbor and waterway areas.

Another object of the invention is to provide a method and apparatus for reducing adverse environmental impacts associated with conventional prior art methods, including release of sediment borne toxins into the water column release of excessive sediment turbidity and the periodic killing of benthic organisms.

Another object of the invention is to provide a method and apparatus for preventing sediment deposition which uniquely uses a safe and efficient horizontal directed, turbulent, nearbottom water discharge typically operated on a daily basis.

Still another object of the invention is to provide a safe and easy to use method and apparatus for preventing sediment deposition in harbors and waterways without interfering with ship navigation.

Another object of the present invention is to provide a method and apparatus for significantly reducing the cost of maintaining adequate water depths in harbors and waterways.

Still another object of the present invention is to provide a method and apparatus which effectively eliminates the need for periodically dredging harbor and waterway areas and disposing of the dredged material.

A further object of the invention is to provide a method and apparatus in which low salinity water can be used for scouring.

BRIEF DESCRIPTION OF THE DRAWINGS

FIG. 1 is a front view of one form of the apparatus of the invention.

FIG. 2 is a side elevational view of the apparatus.

FIG. 3 is a cross-sectional view taken along lines 3—3 of FIG. 1.

FIG. 4 is a front view of an alternate form of apparatus of the present invention.

FIG. 5 is a side view of the apparatus shown in FIG. 4.

FIG. 6 is a generally diagrammatic view illustrating alternate scour patterns obtainable through the use of the apparatus of the present invention.

FIG. 7 is a front view of another alternate form of the apparatus of the invention comprising a gravity support frame which rests against, but is not attached to the pier pilings.

FIG. 8 is a side view of the apparatus shown in FIG. 7.

FIG. 9 is a cross-sectional view taken along lines 9—9 of FIG. 7.

FIG. 10 is an enlarged schematic view of the turbine assembly of the apparatus.

DESCRIPTION OF THE INVENTION

Referring to the drawings and particularly to FIGS. 1, 2 and 3, one form of the apparatus of the present invention is there illustrated. Here, the apparatus is shown being used for preventing sedimentation build-up in a harbor berthing area of the character having a wharf W fronting a berthing area B. In this embodiment of the invention, the apparatus comprises a plurality of scour units 10 and connected to the wharf W in a side-by-side relationship (FIG. 6).

Each scour unit 10 comprises a vertical tubular member 12 having a vertical axis, an upper end 14 and a lower end 16. Connected proximate the upper end of each tubular member 12 is an inlet means for directing the flow of water from a location near the surface of the water of the berthing area into tubular member 12. This inlet means is provided in the form of a bell-mouth shaped, inlet assembly 18. As best seen in FIGS. 1 and 2, assembly 18 is connected with tubular member 12 by means of mating flanges 20 and 22 provided respectively on members 18 and 12. Flanges 20 and 22 are interconnected together by suitable fasteners, such as bolts 24. With this arrangement inlet members of various heights can be readily interconnected with the tubular members 12 so as to position the upper end of the bell-shaped inlet assembly 18 at an optimum location below the surface of the water in the particular berthing area being scoured.

Mounted interiorly of each inlet member 18 is means for controllably drawing water from the near surface of the berthing area into the inlet means. As best seen in FIG. 10, in the present embodiment of the invention, this means is provided as a turbine assembly 26, which includes impeller blades 28, stator blades 28a, a nose fairing 28b, and a tail fairing 28c. Stator blades 28a are attached to the inlet member or chimney (FIG. 10). The impeller blades, or fan, are controllably rotated by a motor means, such as a submersible electric motor 30 mounted inside motor housing 30a. Electric or hydraulic motors, suitable for use in the present application, are well-known to those skilled in the art and are readily commercially available. However the fan stator blades and fairing are custom designed for the defined use.

Connected proximate the lower end of each tubular member 12 is a discharge means, shown here as an elbow shaped member 48, for directing the flow of water outwardly therefrom in a generally horizontal direction to produce a near bottom scour pattern of a predetermined configuration. As best seen in FIG. 6, the scour units 10 are strategically positioned along the wharf W so that the scour patterns P produced by the discharge means overlap one another in an optimized manner.

Referring particularly to FIG. 3, actuating means, generally designated by the numeral 32, are operably connected to each tubular member 12 to affect a desired degree of rotation of tubular member 12 as, for example, selectively through angles of 90 or 180 degrees. As best seen by referring to FIGS. 2 and 3, each of the tubular members 12 is rotatably mounted within vertically spaced apart collar assemblies 34a and 34b. These collar assemblies are, in turn, fixedly interconnected to adjacent wharf pilings 36 by brackets 37a and 37b in the manner shown in FIG. 1.

Collar assemblies 34a and 34b are of identical construction each including angularly inwardly extending arms 35a and 35b which are connected to brackets 37a and 37b. Collar assemblies 34a and 34b also include transverse members 38 which engage the adjacent pilings 36 to counteract the forces generated by the discharge of water through elbows 48. A ring 39 having an ear 40 is connected to each tubular member 12 intermediate collars 34. Disposed intermediate ear 40 and a mounting bracket 37b which interconnects the lower collar assembly 34b with the piling 36 is a hydraulically actuated means for urging rotational movement of ring 39 and in turn tubular member 12.

In the present embodiment of the invention, the hydraulically actuated means comprises a hydraulic cylinder 42 within which a connector arm and piston assembly 44 is carried. Hydraulic cylinder 42 is pivotally interconnected with mounting bracket 37b and connector arm 44 is pivotally interconnected with ear 40 in the manner shown in FIG. 3. Reciprocal movement of the piston interiorly of cylinder 42 urges telescopic movement of connector arm 44 inwardly and outwardly of the cylinder 42, which, in turn imparts rotational movement to ring 39 and to tubular member 12 to which it is connected. With this construction, as tubular member 12 is rotated, the discharge means, shown here as an elbow 48, which is interconnected to tubular member 12 proximate its lower end 16, is also rotated through a predetermined angle. As the tubular member 12 and discharge elbow 48 are rotated by the actuating means, a scour pattern of the character illustrated in the lower part of FIG. 6, is achieved. In the drawings, this scour pattern is shown as semicircular in shape. However, the scour pattern may be of any angle desired for the optimum displacement of sedimentation within any particular berthing area or waterway.

An important aspect of the apparatus of the present invention, is means for preventing ingestion into the scour units of fish, debris and other articles larger than a predetermined size. In the embodiment of the invention shown in FIGS. 1 and 2, this means is provided in the form of a mesh screen 50 which covers the open end of the bell-mouthed shaped inlet 18.

Referring particularly to the upper portion of FIG. 6, the scour units 10 are arranged along the face of the wharf in the manner shown to provide near uniform scour coverage throughout the protected area. Spacing between the assemblies is governed by the lateral dimensions of the individual scour patterns. In the form of the apparatus shown in the drawings, the discharge means are strategically configured to produce fixed scour patterns of a generally tear-dropped configuration having a length to width ratio of about 3. To minimize zones of incomplete scour, the assemblies are arranged so as to produce approximately 20 percent overlap between adjacent scour patterns. As indicated in the lower portion of FIG. 6, rotating the discharge means in the manner previously discussed, produces arcuate shaped scour patterns which span up to 180 degree sectors depending on whether the jets are operated only during ebb and flow conditions or during both ebb and flood flow conditions.

Turning now to FIGS. 4 and 5, another form of the apparatus of the present invention is there illustrated. The apparatus of this form of the invention is similar in many respects to the earlier described apparatus and like numbers are used to identify like components. Each scour unit 54 of this embodiment of the invention comprises a vertical tubular member 56 having a vertical axis, an upper end 58 and a lower end 60. Connected proximate the upper end of each tubular member 56 is an inlet means for directing the flow of water from a location near the surface of the water of the berthing area into tubular member 56. This inlet means is provided in the form of a generally "T" shaped, inlet assembly 62 integrally formed with tubular member 56.

Mounted interiorly of each tubular member 56 is means for controllably drawing water from the near surface of the berthing area into the inlet means. In this second embodiment of the invention, this means is provided as a turbine assembly 64, which includes a fan 66.

a stator 66a and a fairing 66b. The fan is controllably rotated by a pneumatic motor means, such as a submersible hydraulic motor 68. Hydraulic motor 68 is connected to a central, deck-mounted hydraulic power unit 70, via a pair of supply hoses 72 and 74 (FIG. 5). Power unit 70 feeds a supply manifold loop (not shown) with branch lines to each scour unit. Flow to each branch line is controlled by a control device 76 operably associated with power unit 70. Power units and manifolding and control devices of the character described are well known to those skilled in the art and are readily commercially available.

Rotatably connected proximate the lower end of each tubular member 56 is a discharge means, shown here as an elbow shaped member 57, for directing the flow of water outwardly therefrom in a generally horizontal direction to produce a near bottom scour pattern of a predetermined configuration. As was the case with the earlier described embodiment, the scour units 54 are strategically positioned along the wharf W so that the scour patterns P produced by the discharge means overlap one another in an optimized manner. In this second form of the invention, the tubular members 56 are fixedly mounted and only the discharge means is rotatable to produce the scour patterns shown in the lower portion of FIG. 6.

Referring particularly to FIG. 5, actuating means, generally designated by the numeral 80, are operably connected to each discharge elbow 57 to affect a desired degree of rotation of the elbow, for example, selectively through angles of 90 or 180 degrees. The actuating means 80 is of similar construction to that previously described and shown in FIG. 3. More particularly, means 80 comprises a hydraulic cylinder 42 within which a connector arm and piston assembly 44 is carried. Hydraulic cylinder 42 is pivotally interconnected with mounting bracket 82 (FIG. 5) and connector arm 44 is pivotally interconnected with a ring 84 having ear 86. In the present instance, however, ring 84 is connected to discharge elbow 57 which, in turn, is rotatably mounted to tubular member 56 proximate its lower end 60. Reciprocal movement of the piston interiorly of cylinder 42 urges telescopic movement of connector arm 44 inwardly and outwardly of the cylinder 42, which, in turn imparts rotational movement to ring 84 and to elbow 57 to which it is connected. With this construction, as elbow 57 is rotated by the actuation means, a scour pattern of the character illustrated in the lower part of FIG. 6, is achieved. As before, while the scour pattern is shown as semicircular in shape, the scour pattern may be of any angle desired for the optimum displacement of sedimentation within any particular berthing area or waterway.

The apparatus of the second form of the invention, also, includes means for preventing ingestion into the scour units of fish, debris and other articles larger than a predetermined size. This means is here provided in the form of a cylindrically shaped, closed end mesh screen 90 which forms a part of the "T" shaped inlet 62. The "T" shaped screen provides an increased surface area which reduces screen intake velocities sometimes.

Referring particularly to the upper portion of FIG. 6, the scour units 54 are arranged along the face of the wharf in the manner previously described to provide near uniform scour coverage of the character shown throughout the protected area.

In the embodiment of the invention shown in FIGS. 1 through 3, as well as that shown in FIGS. 4 and 5, the

support frame is designed to span two adjacent pilings 36. Chains C (91) which are connected to the wharf, help to support the weight of the scour units and to hold them in place relative to the pilings. The frame allows the thrust from the jet discharge to be carried back against the face of the pilings. The use of simple chain hoist and flexible supply hoses 72 and 74 allows an entire scour unit to be raised out of the water for servicing. Hoist arrangements of this character are well known to those skilled in the art and the details thereof will not be described herein.

Referring to FIGS. 7 through 9, still another form of the apparatus of the invention is shown. In this form of the invention, an alternative support method is illustrated.

The apparatus of this third form of the invention is similar in many respects to the earlier described apparatus and like numbers are used to identify like components. Each scour unit 80 of this embodiment of the invention comprises a vertical tubular member 93 having a vertical axis, an upper end 94 and a lower end 95. Connected proximate the upper end of each tubular member 93 is an inlet means for directing the flow of water from a location near the surface of the water of the berthing area into tubular member 93. This inlet means is provided in the form of an inlet assembly integrally formed with tubular member 93 and having a convex shaped inlet screen 90 covering the inlet port 92.

Mounted interiorly of each tubular member 93 is means for controllably drawing water from the near surface of the berthing area into the inlet means (FIG. 8). In this embodiment of the invention, this means is provided as a turbine assembly 26, of the character shown in FIG. 1.

Connected proximate the lower end of each tubular member 93 is a discharge means, shown here as an elbow shaped member 97, for directing the flow of water outwardly therefrom in a generally horizontal direction to produce a near bottom scour pattern of a predetermined configuration. As was the case with the earlier described embodiment, the scour units 80 are strategically positioned along the wharf W so that the scour patterns P produced by the discharge means overlap one another in an optimized manner.

An important aspect of the form of the invention shown in FIGS. 7 through 9, is the design of the support frame 96 which comprises upper and lower assemblies 96a and 96b. Importantly, frame 96, which is connected to and supports tubular member 93, rests against, but is not connected to the pier pilings 36.

Upper frame assembly 96a comprises a generally rectangularly shaped face member 98 which is connected to upper and lower braces 100 (FIG. 8), which are, in turn, connected to support rings 102 mounted on member 93. Lower frame assembly 96b also comprises a generally rectangularly shaped face member 104 having a cross member 105 which is connected to a brace 106, which is, in turn, connected to a support ring 108 mounted on member 93 (FIG. 8).

Turning to FIG. 9, it can be seen that lower frame assembly 96b further includes a pair of horizontally extending arms 110 which engage pilings 36. These arms function to carry the lateral thrust of the discharge means as the scour unit is rotated in a manner presently to be described. Additionally, face member 104 (FIG. 7) is provided with a lower, transversely extending member 104a which is disposed below elbow 97 to eliminate

the rotational movement induced by the discharge means.

As best seen by referring to FIGS. 8 and 9, actuating means generally designated by the numeral 112, are operably connected to each tubular member 93 to affect a desired degree of rotation of the support member about a fixed point P on the support frame 96b. The actuating means 112 comprises a hydraulic cylinder 114 within which a connector arm and piston assembly 116 is carried. Hydraulic cylinder 114 is pivotally interconnected with frame 96b at a point 117 and connector arm 116 is pivotally interconnected with a bracket 118. Bracket 118 is, in turn, connected to ring 120 which is connected to tubular member 93 at a location above ring 108. The inboard end of bracket 118 is pivotally connected to frame 96b by a pivot pin 122 located at point P. Reciprocal movement of the piston interiorly of cylinder 114 urges telescopic movement of connector arm 116 inwardly and outwardly of the cylinder 114, which, in turn, imparts pivotal movement to bracket 118 about point P. This results in an arcuate movement of tubular member 93 in the manner illustrated in FIG. 9.

The scouring units 80 of this latter embodiment are typically held in place against pilings 36 by chains C (91) of the same character shown in FIGS. 1 and 2. Similarly, the units are raised and lowered by chain hoists of a character well known to those skilled in the art.

In operating the various embodiments of the invention in accordance with the method of the present invention, the scour units are typically activated twice daily by an automatic control system. The control system is programmed to initiate system operation at the optimum time to ensure maximum sediment flushing by ambient currents. Typically, the individual scour units are sequentially activated, beginning with the furthest upstream unit. The duty cycle for each scour unit can be adjusted to accommodate differences in sediment scour properties and the arc of scan rotation. In addition, the rate of scan of each scour unit can be adjusted. Tests have shown that highly cohesive sediments require longer duty cycle times and slower scan rates to ensure proper scouring action. As previously mentioned, by adjusting the location of the intake means, low salinity water can be used for scouring.

The scouring action of the turbine fan discharge serves to resuspend the thin layer of sediment newly deposited during the previous flood tide. The frequent operation of the scour system reduces input power requirements and minimizes the turbidity produced by the discharge plume. In addition, the short residence time of the newly deposited sediments minimizes adsorption of undesirable toxins. Both features serve to minimize potential adverse environmental impacts to water quality.

Having now described the invention in detail in accordance with the requirements of the patent statutes, those skilled in this art will have no difficulty in making changes and modifications in the individual parts or their relative assembly in order to meet specific requirements or conditions. Such changes and modifications may be made without departing from the scope and

spirit of the invention, as set forth in the following claims.

We claim:

1. An apparatus for preventing sedimentation build-up in harbor berthing area of the character having wharf fronting the berthing area, comprising a plurality of submerged, scour units disposed adjacent said wharf in side-by-side relationship, each said scour unit comprising:
 - (a) a vertical tubular member having a vertical axis including an upper end and a lower end;
 - (b) inlet means connected proximate said upper end of said tubular member for directing the flow of water into said tubular member;
 - (c) turbine means mounted interiorly of said inlet means for controllably drawing water into said inlet means, said turbine means including a rotating fan and hydraulic motor means for controllably rotating said fan;
 - (d) discharge means connected proximate the lower end of said tubular member for directing the flow of water outwardly therefrom in a generally horizontal direction to produce a near bottom, scour pattern of a predetermined configuration, said scour units being arranged along said wharf so that said scour patterns produced by said discharge means overlap one another;
 - (e) means for rotating each said discharge means about the vertical axis of each said tubular member, whereby each said discharge means produces a scour pattern spanning about 180 degrees;
 - (f) operating means mounted on said wharf and operably interconnected with each said hydraulic motor means for providing hydraulic fluid for operating each said hydraulic motor means; and
 - (g) means mounted on said wharf for raising and lowering each said tubular member.
2. An apparatus for preventing sedimentation build-up in a harbor berthing area, of the character having a wharf fronting the berthing area, comprising:
 - (a) a vertical tubular member having a vertical axis including an upper end disposed below the surface of the berthing area and a lower end;
 - (b) inlet means connected proximate said upper end of said tubular member for directing the flow of subsurface water into said tubular member;
 - (c) turbine means mounted interiorly of said inlet means for controllably drawing water into said inlet means;
 - (d) discharge means connected by means of a single 45 degree to 135 degree turning elbow proximate the lower end of said tubular member for directing the flow of water outwardly therefrom in a generally, horizontal direction to produce a near bottom scour pattern of a predetermined configuration;
 - (e) fully submerged means for rotating said discharge means about the vertical axis of said tubular member; and
 - (f) means mounted on said wharf for raising and lowering said tubular member.
3. An apparatus as defined in claim 2 further including operating means mounted on said wharf for controllably operating said turbine means.

APPENDIX D: TACKLING TRAPPED SEDIMENTS

by

SCOTT A. JENKINS, JOSEPH WASYL AND DAVID SKELLY

TACKLING TRAPPED SEDIMENTS

SCOTT A. JENKINS
JOSEPH WASYL
DAVID W. SKELLY

Crater-sink fluidization has been used to recover sediment from harbors for the past couple of decades. Can this method bypass sediment around dams and return it to eroded beaches, solving two major problems? Here's how it might happen in Southern California.

Turn-of-the-century photographs show an immense beach near Oceanside, Calif., about 1000 ft wide. Today, no beach in the area has a width of more than a few hundred feet. Many, in fact, are totally denuded of sand during the winter months.

An eight-year, \$6 million study of San Diego County's coastline, completed by the U.S. Army Corps of Engineers in 1990, confirmed that the beaches are in dire need of nourishment. One of the Corps' recommendations involves restoring the equilibrium in the area's littoral cells (the coastal regions defined by the limits of beach sediment movement) by augmenting the sand supply. One possible source of this sand would be to bypass, or transfer, sediment trapped behind area dams to the beaches. Due to the steep topography of the region, dams are situated near the coast, making the suggestion feasible.

At the Scripps Institution of Oceanography, La Jolla, Calif., research is under way with the California Water Authority and the San Diego Association of Governments to discern the best method of dam bypassing for the area. One method under consideration is crater-sink fluidization. The key advantage of this type of hydraulic-extraction system is its fixed-place installation, which allows automation. This system would col-

lect coarse-grain sediments from a top-set delta by means of mobile fluidizer pipes that inject high-pressure water into the sedimentary mass.

During fluidization, the weight of sand particles is balanced by the upward flux of fluid momentum via weight drag. As the body of sand dilates, there is an almost total loss of static shear strength. This loss allows the slurry to readily flow down a shallow slope to a centrally located eductor crater, formed by excavation of sediments with a jet pump (see Fig. 1). From here, the pipes would pump sediments through a hydraulic pipeline to the eroding streambed directly downstream of the dam, or to a collection point for overland transport to eroding beaches.

To understand the efficiency of this method, it helps to take a look at the problems facing the coastal area between Point La Jolla and Dana Point, Calif., which comprises the Oceanside littoral cell (Fig. 2). Dam building in this region began in 1922. The most recent dam was completed in 1977. Altogether, there are 21 catch basins and nine major dams with reservoirs.

A number of streams and rivers in this littoral cell empty into the ocean in the neighborhood of Oceanside, Calif. The delta deposits from the Santa Margarita

and the San Luis Rey rivers, as well as numerous creeks, once contributed an average sediment load estimated at 250,000 cu yd per year to the foreshore.

The entire coastal area in Southern California is typical of a so-called collision coastline. The steep topography of the nearby mountain range and narrow continental shelf are the result of tectonic processes involving collisions between the oceanic and continental plates. The semi-arid climate combined with the steep hydraulic grading results in high sediment transport rates down streams and rivers during seasonal rainfall.

Construction of the Oceanside Harbor-Del Mar boat basin in 1942 exacerbated beach erosion by intercepting the southerly littoral drift. Sediment trapped by the harbor is now dredged on a regular basis and returned to littoral cell south of the harbor entrance. This results in no net long-term effect on the sediment supply to the littoral cell, but the episodic nature of the dredge cycle does contribute to cycles of beach erosion, called erosion waves.

BYPASSING IS BETTER

The principal cause of beach erosion in this area lies in the insufficient supply of beach-sized sand to replace sand transported

south along the coast by waves and wave-driven currents. From 1922 to 1976, an estimated 14.5 million cu yd of sediment was lost down the La Jolla submarine canyon.

As the foreshore recedes landward, waves act directly on the base of the sea cliffs. The beach communities south of Oceanside suffered millions of dollars of property damage from cliff failures during the 1978, 1980 and 1983 winter storms. When large blocks of sea cliff collapse, tens of thousands of cubic yards of potentially new beach sediments enter the near-shore zone. But intense development of the sea cliffs precludes this as an alternative for beach nourishment.

Sandy beaches in equilibrium with incoming waves are the most desirable means of wave energy dissipation and shoreline protection. Structural shore protection and other remedial measures taken so far treat only the symptoms of beach erosion. Building seawalls at the base of the sea cliffs protects only the property directly behind them. In addition to being costly, conventional seawalls accelerate erosion rates by increasing the reflectivity of the shoreline. This causes an increase in the rate at which sand travels cross shore and down slope.

The building of groins and jetties inhibits littoral drift by creating pocket beaches. These beaches don't stop regional erosion, they only defer it to the beaches down drift of the structures. No new sediment is added to the foreshore. The dwindle

ing supply of available sand is merely rearranged.

Bypassing sediment around area dams would not only nourish beaches, but would help mitigate many of the other adverse environmental impacts of dam building. For instance, the streambeds below the dams were in equilibrium with the seasonal flows of sediment-laden water. With no new sediment introduced from upstream sources,

**The three systems
could completely
replenish the
14.5 million cu yd
sand deficit
in 24 years.**

the streambeds can't resist erosion caused by elevated bottom stresses arising from the excess kinetic energy of strong, clear water flows. High river flow rates occur either during periods of heavy rainfall or high water discharge rates from the dams.

Another adverse environmental impact in the Oceanside littoral cell can be found along the San Luis Rey River below the Lake Henshaw Dam. Bank erosion has damaged numerous trestles and utility poles along state Highway 76 and has undermined the roadbed in several places. Reintroducing bypassed sediment directly to the streambeds below the dams would

mitigate much of this erosion.

Also, deposition of sediment in the reservoirs has decreased reservoir capacity. Lake Mead, on the Colorado River, traps an estimated 3 cu mi of sediment every 100 years. Early dam designers recognized this problem and specified sediment traps upstream of the dams. Nevertheless, large sediment deposits still form in the upper reaches of the reservoirs.

These deposits can cause serious problems, even before the useful capacity of the reservoir is seriously threatened. Newly formed deposits place tremendous static loads on the native soils of the original riverbed, resulting in soil subsidence with costly consequences. The static loading of the sedimentary deposits behind Lake Henshaw has caused parts of the Warner Valley to subside as much as 0.5 ft. This subsidence produced large cracks in the dam's earthen core, reducing the reservoir's water storage capacity to only one-third of its original design value.

CRATER-SINK FLUIDIZATION

In choosing the best method of dam bypassing for the area, there are four aspects to consider: (1) the extraction of the sediments from their at-rest position at the reservoirs; (2) the transportation of sediments around the dams; (3) the transportation of sediments from the dam site to the beaches or eroding areas; (4) the dispersion of sediments within the erosion areas.

To effectively extract sediments from

FIELD TEST OF A CRATER-SINK FLUIDIZATION SYSTEM AT THE OCEANSIDE LITTORAL CELL.



the reservoir, the system must adapt to the depositional pattern within the reservoir. Much evidence suggests that in most reservoirs this pattern follows a characteristic delta pattern (see Fig. 1). Surveys of Lake San Marcos in San Diego County, for instance, demonstrate such a pattern.

Typically, these deltas consist of three distinct depositional beds: the top set, fore set and bottom set. These deposits extend along the old river channel and may reach the base of the dam. Grain-size matching, the main criterion in selecting a bypass site, is helped by the natural horizontal sorting within a depositional delta.

Top-set beds consist of the coarsest grain-size sediments, and their packing yields the lowest percentage by weight of water. Generally, these beds most nearly match the grain sizes of the beach and streambed sediments and are the preferred nourishment material. Fore-set beds are intermediate in grain size. Core analysis must determine their suitability as beach nourishment material. Bottom-set deposits consist primarily of clays and fine sand and are unsuitable for beach nourishment, though they have value as topsoil replacements.

This depositional pattern exhibits some variation with annual water-level changes. However, the pattern is sufficiently predictable to allow consideration of a fixed-place hydraulic-extraction technique, known as crater-sink fluidization, to bypass sediment from the top-set deltas. Where road and railroad networks render dam sites accessible, a combination of conventional earth-moving technologies (dredges, bulldozers, clam shells, dump trucks and conveyor belts) must also be considered.

The crater-sink fluidization system has several advantages. It can be run more or less continuously in order to bypass the existing top-set delta, then operated as needed to bypass sediments that accumulate on the top-set portion of the delta during subsequent depositional events. Manpower costs are reduced since the natural dynamics of deposition within the reservoir transport the sand to the system. In addition, sediment can't accumulate undesirable anaerobic bacteria or toxicity when it's bypassed at the same rate it is deposited.

The dimensioning of a crater-sink fluidization is primarily dependent on the bypassing transport rate, the capture volume and the median grain size. The system is sized so that bypassing transport rates are

sufficient to match the deposition rate in the top-set delta. Additionally, the combined capture volume of the crater and fluidization trenches should be large enough to intercept the yield of a major depositional event, which would occur during a 50-year storm.

The annual transport rate into Lake San Marcos reservoir during 1980, for instance, was 200 cu yd per hour. A similar solids fraction pumping capacity would be required. The estimated top-set flux of the extreme flood event of Feb. 16, 1980, is 27,000 cu yd. This capture volume could be generated by excavating five 400 ft long open fluidizers trenches to a depth of 15 ft. In the design of our proposed fluidizer, we use a flexible, noncollapsing hose that workers can retrieve after excavation. This would allow the excavation of each fluidization trench to be accomplished with the same mechanical components. Past experience has shown that the systems are sensitive to debris-fouling in the fluidization trenches. So it is important that the mechanical components are retrievable for defouling.

VALUE ENGINEERING

The precise economics of bypassing sediment depend on site factors unique to each

reservoir. However, we can make a reasonable estimate of the costs using conventional means, based on numbers from a major beach nourishment project undertaken by the Corps of Engineers from November 1981 through May 1982, at the San Luis Rey river. The Corps extracted 923,000 cu yd of sediment from borrow pits, then dry hauled it by truck 7 mi to nourishment sites south of the Oceanside Harbor. The process cost \$2.71 per cubic yard. Assuming a 5% annual inflation rate, a similar nourishment project today would cost \$4.41 per cubic yard.

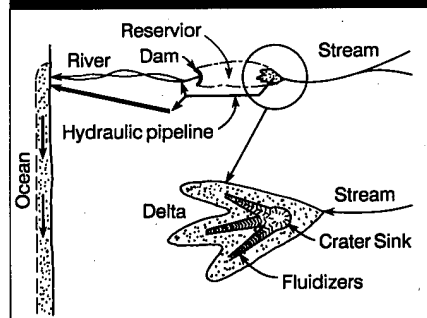
The average distance from a reservoir in the Oceanside littoral cell to the beach is 30 mi. Extra transportation costs would be 15–30¢ per mile. This would increase unit costs anywhere from \$7.86 to \$11.31 per cubic yard. Fully restoring the beaches in the Oceanside littoral cell would require 14.5 million cu yd of sediment at a cost of \$114 million–\$164 million.

Crater-sink systems must operate on at least three major reservoirs in order to bypass the required 14.5 cu yd of sediment. The three most promising sites are Lake Henshaw, Vail Lake and the San Marcos reservoirs. Assuming a 10-year system life span, and that each system will bypass 300,000 cu yd of sediment each year, unit capital costs would be about 85¢ per yard of sediment. The annual maintenance costs are estimated at 5% of initial capital costs, adding 5¢ per cubic yard of sediment. Energy costs for equipment operation will add roughly 20¢ per cubic yard to the cost of bypassing the sediment around the dams. The unit cost totals \$1.10 per cubic yard.

The three systems would completely replenish the 14.5 million cu yd sand deficit in the Oceanside littoral cell in 24 years, assuming that sand is continually lost in sediment sinks such as La Jolla Canyon at the historic littoral drift rate of 300,000 cu yd per year. If the sediments are transported hydraulically in the streambeds with natural stream flow, the total cost of this nourishment would come to \$15.9 million. This compares very favorably with the \$114 million–\$164 million estimated for bypassing with conventional earth-moving equipment.

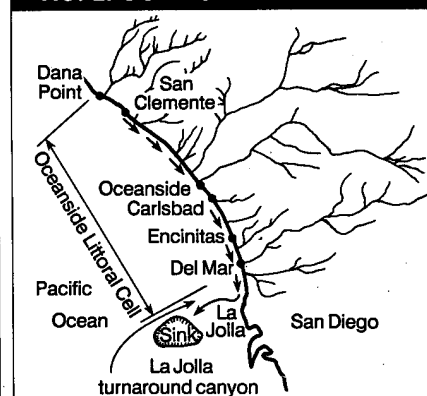
Scott A. Jenkins is research engineer, and Joseph Wasyl and David W. Skelly, M.ASCE, are development engineers for Scripps Institution of Oceanography, University of California, San Diego.

FIG. 1. DAM BYPASS SYSTEM



THE PRINCIPAL COLLECTION DEVICE IS A CRATER-SINK FLUIDIZATION SYSTEM POSITIONED OVER A DEPOSITION DELTA.

FIG. 2. OCEANSIDE LITTORAL CELL



APPENDIX E:

**U. S. PATENT PENDING
SERIAL # 08/206,501**

**METHOD AND APPARATUS FOR FOCUSING WAVE
ENERGY ON COLLECTING DEVICES**

by

SCOTT A. JENKINS, JOSEPH WASYL & CHARLES ROBINS

BACKGROUND OF THE INVENTION

5

Although the available power of ocean wind wave has been calculated at 2.5×10^{12} W globally, present wave energy recovering technology is only marginally economical even along a high energy coastline such as the United Kingdom. This is in large part due to limited available energy density, which requires large numbers of energy collectors to be strung out along a given length of coastline in order to recover economically feasible quantities of wave energy.

10
15
20
25
30
A number of attempts have been made to focus tidal and wave energy into a limited area to allow for efficient conversion for power production, including those disclosed in the patents of Arpin (U.S. Patent No. 2,069,715), Danel (U.S. Patent No. 2,435,576), Gay (U.S. Patent No. 2,441,759), Southwick (U.S. Patent No. 2,820,148), Conn, et al. (U.S. Patent No. 4,034,231), Borgren (U.S. Patent No. 4,363,564) and Mehlum (Re 32054). The Danel, Gay, Southwick and Borgren patents each describe the use of sea walls of various geometries which are designed to channel wave energy to one or more focal points. The Mehlum patent discloses a variation on the solid converging sea walls or channels which involves the creation of a diffraction grating formed from discreet structures arranged in a grid pattern. The grid pattern becomes a Fresnel lens, focusing the energy by diffracting the incoming waves. Finally, the Conn, et al. patent relies only partially on redirection of wave energy. Instead, this device is a V-shaped pier-like structure with a number of water turbines distributed at different points of the structure. Rather than bringing the waves to the turbine, or the conversion device, the turbines are distributed to utilize a section of the wave front.

A common concern of each of these devices is the sea wall or channel. The construction of permanent structures can be expensive and potentially environmentally destructive by altering the local ocean current patterns. Also, changes in sea topography due to storms and erosion can

cause the ideal location for energy collector placement to shift, rendering an expensive permanent structure less effective.

5 The need for a portable reef or sea wall has been addressed in U.S. Patents No. 2,069,715 of Arpin and No. 3,886,751 of Porraz Jimenez Labora.

10 The artificial reef of Arpin is limited in that its structure is relatively shallow, either in a triangular or semicircular cross section. While some modifications of wave patterns in shallow water is possible, the entire purpose of this artificial reef is to provide a nucleation point to accumulate sand to form a sandbar. This type of structure would not be effective in providing sufficient wave channeling for energy conversion purposes.

15 The aquatic construction modules of Porraz Jimenez Labora come closer to meeting the needs of a portable, sturdy structure for modifying water flow patterns. However, the interlocking edges of the modules must be individually aligned and linked together during assembly of the reef or other protective barrier. This procedure, while suitable for construction of temporary levees and channels well in advance of flooding, where rapid assembly of the barrier is not critical, is extremely impractical for construction in existing bodies of water, especially in the presence of ocean swells, using conventional floating cranes and riggings.

SUMMARY OF THE INVENTION

25 It is an advantage of the present invention to provide a structural unit for formation of artificial reefs for diverting and channeling wave energy and water in general.

It is another advantage of the present invention to provide an artificial reef structure for channeling wave energy for energy collection.

30 It is still another advantage of the present invention to provide an optimized artificial reef structure for enhancing the energy of a collected wave.

35 In an exemplary embodiment the artificial reef of the present invention is constructed from a plurality of structural units each of which is a tetrahedron-shaped sandbag, which are arranged in a talus pile. With the exception of the tetrahedron-shape, the sandbags themselves are

constructed according to conventional sandbag technology, using the same materials and assembly techniques. Typically, sandbags are made from polypropylene or polyester fabric bags which are filled with sand. A minimum of five layers thick of the structural units is required in the talus pile to reduce the permeability of the reef to less than five percent. This level of permeability is important to obtain a solid body response.

The reefs are formed by dropping the structural units in the desired locations. The tetrahedron-shape of the structural units provides a self-interlocking structure which can be placed *en mass* on the sea floor without individual alignment of each bag.

The geometry of the reef structure is a sloped bar, a parallel bar, or a V-shaped bar, or combinations thereof. The seaward slope is important in determining the amount of energy which can be focused, while the parallel bar or V-shaped bar focuses energy to discreet locations. The parallel bars, which run parallel to the wave front, trap standing waves between the bars to reinforce the incoming waves with a maximum energy focused where the rays of trapped waves cross the wave rays of the incoming swell.

A multiple V-shaped bar configuration, with the apex of the V pointing diagonal to the incoming waves creates Bragg reflection patterns which cause crossing wave rays to form local concentrations of wave energy.

BRIEF DESCRIPTION OF THE DRAWINGS

Understanding of the present invention will be facilitated by consideration of the following detailed description of the preferred embodiment of the present invention, taken in conjunction with the accompanying drawings in which like reference numerals refer to like parts and in which:

Figure 1 is a perspective view of a structural unit of the present invention, partially cut away;

Figure 2a is a front elevation and Figure 2b is a side elevation of an artificial reef according to the present invention;

Figure 3 is a top view of a parallel bar arrangement;

Figure 4 is a top view of a multiple V-shaped bar arrangement;

Figures 5a-5c are plots of wave enhancement by a parallel reef at frequencies of 0.85 Hz (Figure 5a) and 0.95 Hz (Figure 5b) with a reef spacing of 125 cm and at .70 Hz with a reef spacing of 105 cm (Figure 5c);

5 Figure 6a is a plot of the power spectrum of the control wave from the structure of Figure 5b;

Figure 6b is a plot of the power spectrum of the enhanced wave from the structure of Figure 5b;

Figure 7 is a comparison of predicted resonance separation for a parallel bar reef from linear theory versus measured laboratory results;

10 Figure 8 is a plot illustrating the blue shift hypothesis;

Figures 9a-9c are plots of alterations in wave characteristics caused by a V-bar reef for wave frequencies of 0.5 Hz (Figure 9a), 0.7 Hz (Figure 9b) and for a wave period of 1.6 seconds (Figure 9c).

15 DESCRIPTION OF THE PREFERRED EMBODIMENT(S)

As illustrated in Figure 1, the structural unit 2 is a sandbag formed by sewing together triangular sheets of polypropylene or polyester fabric, typically woven, to form a tetrahedron-shaped bag within which sand 3,
20 gravel, or a sand/gravel mixture is retained. Generally, any type of filler with a similar weight and conformability may be used, including gels or liquids. For simplicity, further descriptions will identify the filler as "sand", which can include any of the above-identified fillers and their equivalents. The dimensions of each structural unit 2 may vary, however, in the preferred
25 embodiment, structural units with heights of 4 feet and 6 feet are intermixed to form the desired artificial reef structures. In Figures 2a, 2b and 3, the different sizes of structural unit are indicated by the hashed triangles for 6 feet and open triangles for 4 feet.

In Figure 2, a single bar structure artificial reef formed from plurality
30 of structural units 2 is illustrated. As can be seen, the structural units have intermixed sizes which are randomly distributed by dropping the structural units over the location at which the reef is to be formed. As illustrated in Figure 3, the bar arrangement does not consist of a single thickness wall of structural units, but is essentially a talus pile formed by dropping the
35 structural units around the target point to form a bar with a width

corresponding to the combined widths of structural units. In the preferred embodiment, a reef width of at least five structural units is needed to reduce the permeability of the reef to less than 5%. The height of the reef is determined by the ocean depth at the location of formation as well as the range of wave heights and wave periods. The seaward slopes of the artificial reefs are important in determining the amount of energy which can be focused on a given energy collector by the given reef shape.

The optimal wave form for both energy recovery and shore protection was found to be a plunging wave. The plunging wave was obtained when the slope of the reef was sufficiently steep to ensure a Carrier-Greenspan parameter less than 0.4 according to the equation:

$$\tan \beta > \left(\frac{\sigma^2 H_b}{0.4g} \right)^{1/2}$$

(1)

15

Here, $\tan \beta$ is the slope of the bar, H_b is the height of the breaking wave, σ is the radian frequency equal to $2\pi/T$, where T is the wave period, and g is the acceleration of gravity. Consequently, the bar must be steeper as the wave heights increase or the wave periods decrease. If the reef slope is constrained for structural regions to some particular angle of repose, the tendency for plunging waves will increase as the wave period expands or the wave height decreases.

20

To accommodate both average and extreme conditions, multiple reefs such as the parallel bar of Figure 3 and V-shaped reefs of Figure 4 may be required. Multiple reef configurations have the added advantage of providing unique wave structure interactions that can dramatically enhance the local wave height, as much as 80%.

25

In the case of the parallel bars 4 and 4' of Figure 3, standing waves, indicated by wave rays 6, may become trapped between the bars and reinforce the incoming waves, indicated by wave rays 8. For non-normal incidence, the strongest reinforcement occurs where the rays of trapped

30

waves 6, shown by the dotted lines, cross the wave rays 8 of the incoming swell, indicated by the solid lines. The wave energy collection devices should be placed in the region of the loci 30 for maximum energy recovery. Other wave effects resulting from the placement of the parallel bars include
5 specular reflected waves, shown as wave rays 7, and non-specular leaky waves, shown as wave rays 9.

In the multiple V-bar configuration illustrated in Figure 4, there is the possibility for appropriate spacings of the V-bars 42 to create Bragg reflection patterns. These complex interference patterns result in crossing
10 wave rays which provide local concentrations in wave energy, indicated by "bright spots" 10, after multiple reflections between the various elements of the V-bar system. The bright spots 10 in this complex interference pattern are the focal points of the incident wave beams 12 and become the most efficient wave energy collection points.

15 In Figure 3, wave rays are diagrammed over a parallel bar configuration consisting of 4 and 4'. It has been found that for a given wave direction relative to the reefs, there is a particular frequency at which wave enhancement is especially vigorous. Figures 5a-5c provide comparative data of wave enhancement due to the parallel reefs at three
20 different wave frequencies. In these plots, the solid lines (labeled "REEF") are measured by wave staffs in the trapping zone 12 between the parallel reefs 4 and 4', while the dotted lines (labeled "CONTROL") correspond to waves at a comparable depth along the undisturbed shore. In all cases, the heights of the waves are increased due to the presence of the parallel reefs
25 4 and 4', while at the same time, the peaks are made steeper and sharper.

For the higher frequency waves in Figure 5a, the heights have been increased by nearly 87% over those of the control wave heights as a result of the energy trapping effects of the parallel reefs. A similar enhancement is seen at the slightly higher frequency illustrated in Figure 5b.

30 For more complex sea states at lower frequencies, such as the conditions of Figure 5c, the parallel reefs are shown to greatly increase the steepness of the waves. Again, the increase in wave heights relative to the undisturbed shore (control) ranges from 78-91%. By examining the power spectra of the data in Figure 5c, it is apparent that increases in wave heights

are the result of harmonics which are enhanced or trapped by the parallel reefs.

Figure 6a is a plot of the power spectra in the control area of the undisturbed beach, while Figure 6b shows the power spectra obtained between the two parallel reefs 4 and 4' in the energy trapping zone 14. Comparing the two plots, the harmonics in Figure 6b are significantly enhanced from those of Figure 6a. Because these harmonics are phase-locked to the fundamental frequency of the incoming waves, they act to reinforce the predominant peak, resulting in the very steep faces and increased wave heights shown in Figure 5C.

Initial laboratory testing involved direct measurement and photography of the response of 1-2.5 second laboratory waves to model talus pile bars and reefs. These model reefs were constructed of concrete tetrahedrons of two sizes, 2" and 3". In certain modeled cases that involved local wave height doubling, the interactions induced in the laboratory from incident waves of 1 second period and 10 cm amplitude formed jets of water which rose as high as three feet in the air. This condition was observed for 1 m spacings between the parallel bars and a 12° wave angle. Video data of this condition was combined with wave staff measurements to provide the optimal reef separation as a function of the frequency of the incoming waves. This relationship is plotted in Figure 7. The solid line corresponds to the prediction based on linear theory for the formation of a trapped wave at some multiple of the incident wave lengths, as given by:

$$S = \frac{T}{2} \sqrt{gh} \cos \alpha$$

(2)

Here, S is the separation between the bars (the width of trapping zone 14) in the on/offshore direction and α is the approach angle of the incoming swells.

Two physical phenomena combine to create the vigorous wave enhancement. The first is a trapping of the incident wave energy between the two bars 4 and 4' in the form of a standing wave. If this were the only

mechanism, the data in Figure 7 should allow the solve line prediction of linear theory. Therefore, another mechanism is clearly at work. That mechanism is the creation of a double caustic as a result of the change in the wave lengths.

5 The wave length is reduced by dissipative effects over the porous breakwater surfaces as the incoming and reflected waves refract over the tops of the bars. This is illustrated schematically in Figure 8, in which an undisturbed incident wave 20 is compared against a wave 22 propagating over the reef 4. The phase speed of the incident wave 20 is C_0 . Phase
10 speed of the waves after passing over the reef 4 is C' , which is slowed down due to the effects of friction over the reef.

 Since the phase speed is simply a ratio of the radian frequency to the wave number, the phase speed can only be reduced by either reducing the frequency, or by increasing the wave number through wave length
15 reduction. (The wave number is 2π over wavelengths.) However, according to the principle of stationary phases

$$20 \quad \frac{\partial k}{\partial t} + \nabla \sigma = 0 \quad (3)$$

$$\text{in steady state: } \frac{\partial k}{\partial t} = 0 \quad \text{so} \quad \nabla \sigma = 0, \quad (4)$$

25 so if the incoming wave train is steady, the frequency cannot change in space, i.e.,

$$30 \quad C' < C_0 \quad \text{so} \quad k' > k_0. \quad (5)$$

 Therefore, the wave number must be increased due to friction, and the wave length is correspondingly reduced. This reduction in wave length can be estimated by applying the Lorentz Principle:

$$35 \quad (C_{D0} = C_r |u|) u \sim \sigma f u \quad (6)$$

hence,

$$k' = k_0 \left(\frac{\sqrt{1+f^2} + 1}{2} \right)^{1/2} = k_0 + \frac{\phi}{l}$$

(7)

5 The Lorentz Principle linearizes the drag effects of the reef in terms of units of virtual mass force or first order wave pressure. The resulting formulation gives rise to a blue-shift in wave number k' proportional to a dissipation coefficient f .

10 Because of this change in wave number or wave length, the data in Figure 7 did not obey linear theory. Instead, the optimal separation distance in space 14 of Figure 2 is proportional to the dissipation coefficient. The result is a double caustic at the point indicated by reference numeral 30, formed by the constructive interference between the incoming swell waves, the trapped standing waves 32 between the reefs 4 and 4' and the refracted waves with altered wave lengths. This constructive interference actually
15 occurs between the two bars 4 and 4', although generally closer to the inshore bar 4. This positioning of the double caustic 30 insures that the optimal location 34 of the wave energy collectors occurs in the relatively deep area between parallel bars 4 and 4', rather than over them, thereby limiting the possibility of potential damage to the moorings of the collectors.
20 Measurements of the onshore and inshore wave heights showed wave height nearly doubling due to the energy trapping and an 80% reduction of wave height inshore of the parallel bar system. Therefore, the double caustic 30 offers both enhanced wave energy recovery as well as an effective mechanism for providing shore protection.

25 The other wave height enhancing reef geometry tested was the V-bar system illustrated in Figure 4. The vertex 40 of the V-bar 42 is arranged seaward with the axis before of the V orthogonal to the local depth contours. Incoming waves are focused near the vertex 40 of the V-bar 42 through local diffraction, acting to bend wave rays perpendicular to the local
30 surfaces of the bar and thereby creating a convergence of energy at the vertex 40. Time series measured for the wave enhancing effects of the V-bar are shown in Figures 9a-9c. In these plots, the curves labeled CONTROL

correspond to the control area on the undisturbed beach. The time series denoted with REEF were measured in the breaker zone of the V-bar. Waves having a low frequency on the order of 0.5 Hz (Figure 9a) experience only modest increase in the breaker heights, on the order of 25-30%, as a result of the placement of the V-bar arrangement. At higher frequencies, in Figures 10 and 11, the breaker heights are nearly doubled by the convergence effects of the V-bar. Again, the wave form is steepened with the higher frequency lumps (surface chop) measured in the control area not being eliminated from those breakers in the V-bar.

In some cases at 0.7 Hz, shown in Figure 9b, the V-bar more than doubles the incident wave height. Vertex angles ranging from 30-160° were evaluated. The optimal range of vertex angles for the V-bar was found to be 120°. The actual selection of vertex angles at a given site, however, will be controlled by the beach slope, with steep beaches requiring larger vertex angles. The large vertex angles on the steep beaches will cause the wave to shoal farther offshore with characteristics desirable for efficient energy recovery.

In order to obtain the highly dissipative plunging breakers that are optimal for energy recovery and shore protection alike, the reef slope and the water depth over the reef must be tailored to suit 4 particular sight parameters: (1) the wave height and (2) wave period resulting from the local wave climate, H and T ; (3) the local tidal elevation η ; and (4) the wave direction α . The reef slope must be adjusted according to some prevalent wave height, period and tidal range. To take advantage of wave height enhancing techniques such as the parallel bar and the V-bar, the design must also be tuned to the most prevalent wave directions α . Once these site-specific design wave conditions have been established, together with the tidal conditions, the reef geometry can be posed by Equation (1) and

$$S = \frac{n\lambda}{2} \left(\frac{2}{\sqrt{1+f^2} + 1} \right)^{\frac{1}{2}} \cos \alpha$$

The wave forces on the structural units 2, which act to roll them, vary in response to local wave conditions according to the equation:

$$F = \frac{1}{2} t^2 \rho c_f \sigma^2 H^2 + \rho c_m \frac{4}{3} l^2 \sigma^2 \quad (9)$$

5 where c_f is the drag coefficient, c_m is the virtual mass coefficient, ρ is the density of water, and l is the dimension of the structural unit 2. Experiments were conducted in the wind/wave channel to determine the drag and virtual mass coefficients in the above equation. During these
10 experiments, frequencies varied 0.73 Hz-1.93 Hz. Wave heights were varied from 5-20 cm. This produced variations in wave lengths corresponding to deep water waves for the 0.73 Hz waves to the shallow water waves for the 0.195 Hz waves. The resulting virtual mass (c_m) and drag (c_f) coefficients obtained during these tests are compiled in Tables 1a-c and 2a-c
15 for deep water waves, intermediate water waves and shallow water waves. Tables 1a and 2a provide the conditions under which the tests were run, Tables 1b and 2b are the virtual mass coefficients c_m corresponding to Tables 1a and 2a, respectively. Tables 1c and 2c are the drag coefficients c_D corresponding to Tables 1a and 2a.

20

TABLE 1A

	Freq (Hz)	H(cm)	k (cm ⁻¹)	k ₂	u _m D/u	U _m T/D
Deep Water	0.732	5	0.0216	0.216	0.409 x 10 ⁴	0.167
Waves	0.732	10	0.0216	0.216	0.785 x 10 ⁴	0.322
<u>kh</u>	0.732	15	0.0216	0.216	1.128 x 10 ⁴	0.462
2π > 1/2	0.732	20	0.0216	0.216	1.408 x 10 ⁴	0.577
Intermediate	0.585	5	0.0142	0.142	0.617 x 10 ⁴	0.316
Water Waves	0.585	10	0.0142	0.0142	0.173 x 10 ⁴	0.600
<u>1 kh</u>	0.585	15	0.0142	0.142	1.749 x 10 ⁴	0.895
200 < 2π < 1/2	0.585	20	0.0142	0.142	2.203 x 10 ⁴	1.128
Intermediate	0.391	5	0.0076	0.0757	0.835 x 10 ⁴	0.640
Water Waves	0.391	10	0.0076	0.0757	1.756 x 10 ⁴	1.347
<u>1 kh</u>	0.391	15	0.0076	0.0757	2.608 x 10 ⁴	2.000
200 < 2π < 1/2	0.391	20	0.0076	0.0757	3.373 x 10 ⁴	2.580
Shallow Water	0.195	5	0.0033	0.0333	1.027 x 10 ⁴	1.580
Waves	0.195	10	0.0033	0.0333	2.091 x 10 ⁴	3.216
<u>kh</u>	0.195	15	0.0033	0.0333	2.965 x 10 ⁴	4.560
2π < 1/200	0.195	20	0.0033	0.0333	3.609 x 10 ⁴	5.553

TABLE 1B

	run 1	run 2	C_m run 3	run 4
Deep Water	0.639	0.643	0.642	0.645
Waves	0.699	0.689	0.699	0.695
$\frac{kh}{2\pi} > 1/2$	0.704	0.700	0.704	0.703
	0.763	0.758	0.752	0.754
Intermediate	0.636	0.635	0.634	0.636
Water Waves	0.635	0.641	0.634	0.636
$\frac{1}{200} \frac{kh}{2\pi} < 1/2$	0.694	0.694	0.690	0.696
	0.706	0.710	0.719	0.718
Intermediate	0.859	0.865	0.873	0.878
Water Waves	0.811	0.807	0.810	0.808
$\frac{1}{200} \frac{kh}{2\pi} < 1/2$	0.745	0.753	0.751	0.751
	0.803	0.772	0.781	0.720
Shallow Water	0.417	0.419	0.421	0.421
Waves	0.408	0.404	0.409	0.409
$\frac{kh}{2\pi} < 1/200$	0.448	0.447	0.453	0.446
	0.491	0.481	0.495	0.491

TABLE 1C

$$C_D = 2C_f$$

	run 1	run 2	run 3	run 4
Deep Water	45.31	45.58	45.67	46.17
Waves	26.29	25.57	25.16	25.80
$\frac{kh}{2\pi} > 1/2$	18.41	18.16	18.41	18.26
	15.99	15.76	15.48	15.64
Intermediate	24.19	24.45	24.35	24.11
Water Waves	12.44	12.66	12.61	12.69
$\frac{1}{200} < \frac{kh}{2\pi} < 1/2$	9.15	9.16	9.06	9.22
	7.26	7.37	7.56	7.58
Intermediate	15.61	15.72	15.99	16.24
Water Waves	7.16	7.12	7.16	7.11
$\frac{1}{200} < \frac{kh}{2\pi} < 1/2$	4.39	4.46	4.46	4.45
	4.07	3.79	3.83	3.29
Shallow Water	3.16	3.17	3.19	3.19
Waves	1.50	1.48	1.49	1.51
$\frac{kh}{2\pi} < 1/200$	1.16	1.19	1.17	1.18
	1.06	1.08	1.04	1.06

TABLE 2A

	Freq (Hz)	H (cm)	k (cm ⁻¹)	k ₂	U _m D/u	U _m T/D
Deep Water	0.732	5	0.0216	0.108	0.204 x 10 ⁴	0.334
Waves	0.732	10	0.0216	0.108	0.393 x 10 ⁴	0.644
<u>kh</u>	0.732	15	0.0216	0.108	0.564 x 10 ⁴	0.924
2π > 1/2	0.732	20	0.0216	0.108	0.704 x 10 ⁴	1.154
Intermediate	0.586	5	0.0142	0.071	0.308 x 10 ⁴	0.632
Water Waves	0.586	10	0.0142	0.071	0.586 x 10 ⁴	1.200
<u>1 kh</u>	0.586	15	0.0142	0.071	0.874 x 10 ⁴	1.790
200 < 2π < 1/2	0.586	20	0.0142	0.071	1.101 x 10 ⁴	2.256
Intermediate	0.391	5	0.0076	0.037	90.417 x 10 ⁴	1.280
Water Waves	0.391	10	0.0076	0.037	90.878 x 10 ⁴	2.694
<u>1 kh</u>	0.391	15	0.0076	0.037	91.304 x 10 ⁴	4.001
200 < 2π < 1/2	0.391	20	0.0076	0.037	91.686 x 10 ⁴	5.160
Shallow Water	0.195	5	0.0033	0.0167	0.513 x 10 ⁴	3.161
Waves	0.195	10	0.0033	0.0167	1.045 x 10 ⁴	6.432
<u>kh</u>	0.195	15	0.0033	0.0167	1.482 x 10 ⁴	9.122
2π < 1/200	0.195	20	0.0033	0.0167	1.804 x 10 ⁴	11.106

TABLE 2B

	C_m			
	run 1	run 2	run 3	run 4
Deep Water	0.676	0.674	0.678	0.680
Waves	0.726	0.726	0.727	0.732
$\frac{kh}{2\pi} > 1/2$	0.754	0.748	0.761	0.761
	0.749	0.746	0.754	0.746
Intermediate	0.675	0.688	0.689	0.691
Water Waves	0.708	0.685	0.700	0.709
$\frac{1}{200} < \frac{kh}{2\pi} < 1/2$	0.662	0.656	0.659	0.663
	0.689	0.689	0.691	0.697
Intermediate	0.814	0.816	0.818	0.819
Water Waves	0.792	0.790	0.792	0.790
$\frac{1}{200} < \frac{kh}{2\pi} < 1/2$	0.716	0.713	0.714	0.714
	0.671	0.665	0.672	0.666
Shallow Water	0.405	0.401	0.403	0.400
Waves	0.367	0.381	0.383	0.379
$\frac{kh}{2\pi} < 1/200$	0.406	0.404	----	0.407
	0.416	0.411	0.426	0.414

TABLE 2C

$$C_D = 2C_f$$

	run 1	run 2	run 3	run 4
Deep Water	23.78	23.77	23.99	24.21
Waves	13.91	13.78	13.75	13.94
$\frac{kh}{2\pi} > 1/2$	10.13	10.01	10.32	10.34
	7.30	7.22	7.41	7.52
Intermediate	14.57	14.98	15.13	15.20
Water Waves	8.43	7.93	8.25	8.48
$\frac{1}{200} < \frac{kh}{2\pi} < 1/2$	4.41	4.34	4.37	4.42
	3.57	3.57	3.60	3.65
Intermediate	7.72	7.64	7.67	7.70
Water Waves	3.52	3.50	3.51	3.49
$\frac{1}{200} < \frac{kh}{2\pi} < 1/2$	2.13	2.12	2.11	2.12
	1.55	1.53	1.55	1.55
Shallow Water	1.55	1.53	1.53	1.50
Waves	0.711	0.697	0.706	0.692
$\frac{kh}{2\pi} < 1/200$	0.542	0.540	-----	0.544
	0.468	0.466	0.483	0.470

The virtual mass coefficients were found to be surprisingly small, ranging from 0.4 to 0.9. However, the drag coefficients were found to be remarkably large, reaching as high as $c_d = 45$. In order to provide a design safety margin to ensure that the reef maintains its integrity and remains in place, the most extreme values in drag coefficient and virtual mass coefficient were used for estimating the strength requirements of a prototype reef.

To satisfy the requirements of the extreme design wave, the minimum structural unit count for the talus pile according to Equation (9) with values from the tables is estimated to be 860 bags to construct a single V-bar reef, as shown in Figure 4, or 1,825 structural units to construct a single parallel bar field.

The structural units and artificial reefs constructed therefrom of the present invention effectively concentrate or focus the incident wave energy at discrete locations so that wave energy can be efficiently channeled into collectors for conversion into usable power. The structural units are inexpensive and durable, can be easily installed at the desired site, and can be repositioned without major demolition and reconstruction efforts, as compared to a fixed form artificial reef. The parallel bar and V-bar configurations are designed to concentrate and amplify energy for improved efficiency of energy conversion. The structural units and artificial reefs constructed therefrom may also be used for protection of the shoreline from wave damage and as an alternative for levee and flood barrier construction.

It will be evident that there are additional embodiments which are not illustrated above but which are clearly within the scope and spirit of the present invention. The above description and drawings are therefore intended to be exemplary only and the scope of the invention is to be limited solely by the appended claims.

WE CLAIM:

CLAIMS

1. An artificial reef structure for focusing ocean wave energy on
2 collection devices comprising:
a plurality of structural units disposed in at least one talus pile,
4 each structural unit comprising a sandbag having a tetrahedron-shape
with four corners wherein said corners substantially interlock one said
6 structural unit with other structural units of said plurality.
2. An artificial reef structure as in Claim 1, wherein said sandbag
2 comprises a durable polymer fabric formed into a tetrahedron-shaped bag
filled with sand.
3. An artificial reef structure as in Claim 1, wherein said plurality of
2 structural units comprises at least two groups of structural units, each
group having different dimensions from other groups.
4. An artificial reef structure as in Claim 1, wherein said at least one
2 talus pile comprises two parallel bar aligned generally parallel to a
shoreline and separated by spacing to enhance wave height of incoming
4 waves within said spacing at a location of said collection devices.
5. An artificial reef structure as in Claim 1, wherein said at least one
2 talus pile comprises a plurality of V-shaped bars, each V-shaped bar
having a vertex and an axis, wherein said axis is disposed orthogonal to
4 local depth contours.
6. An artificial reef structure as in Claim 5, wherein said vertex has an
2 angle within the range of 30°-160° and said angle is selected according
to a slope of an adjacent beach, with a steep beach requiring a larger
4 vertex angle.
7. An artificial reef structure as in Claim 1, wherein said at least talus
pile has a height and a slope selected according to wave height, wave
period, local tidal elevation and wave direction.

8. An artificial reef structure as in Claim 1, wherein said at least one
2 talus pile has a width comprising at least five structural units.

9. A structural unit for an artificial reef structure comprising:
2 a sandbag having a tetrahedron-shape with four corners wherein
said artificial reef structure is formed by creating a talus pile from a
4 plurality of structural units so that corners of said structural units
substantially interlock one said structural unit with other structural units
6 of said plurality.

10. A method for focusing ocean wave energy on a collection device
2 which comprises:
forming a plurality of structural units each comprising a
4 tetrahedron-shaped bag filled with sand;
identifying a location adjacent a shoreline at which the ocean wave
6 energy is to be collected; and
disposing said plurality of structural units at said location to form at
8 least one talus pile.

11. A method for focusing wave energy as in Claim 10, wherein the
2 step of identifying a location includes measuring wave height, wave
period, local tidal elevation and wave direction.

12. A method for focusing ocean wave energy as in Claim 10, wherein
2 the step of disposing said plurality of structural units includes forming two
parallel bars separated by a spacing to enhance wave height of incoming
4 waves within said spacing at a location of the collection device.

13. A method for focusing ocean wave energy as in Claim 10, wherein
2 the step of disposing said plurality of structural units includes forming a
plurality of V-shaped bars to create a diffraction pattern for enhancing
4 wave height.

ABSTRACT

6

8 The artificial reef of the present invention is constructed from a
10 plurality of structural units each of which is a tetrahedron-shaped
12 sandbag, which are arranged in a talus pile. The reefs are formed by
14 dropping the structural units in the desired locations. The tetrahedron-
16 shape of the structural units provides a self-interlocking structure which
18 can be placed *en mass* on the sea floor without individual alignment of
20 each bag. The geometry of the reef structure is a sloped bar, a parallel
 bar, or a V-shaped bar, or combinations thereof. The parallel bars, which
 run parallel to the shoreline, trap standing waves between the bars to
 reinforce the incoming waves with a maximum energy focused where the
 rays of trapped waves cross the wave rays of the incoming swell. A
 multiple V-shaped bar configuration, with the apex of the V pointing
 diagonal to the incoming waves creates Bragg reflection patterns which
 cause crossing wave rays to form local concentrations of wave energy.

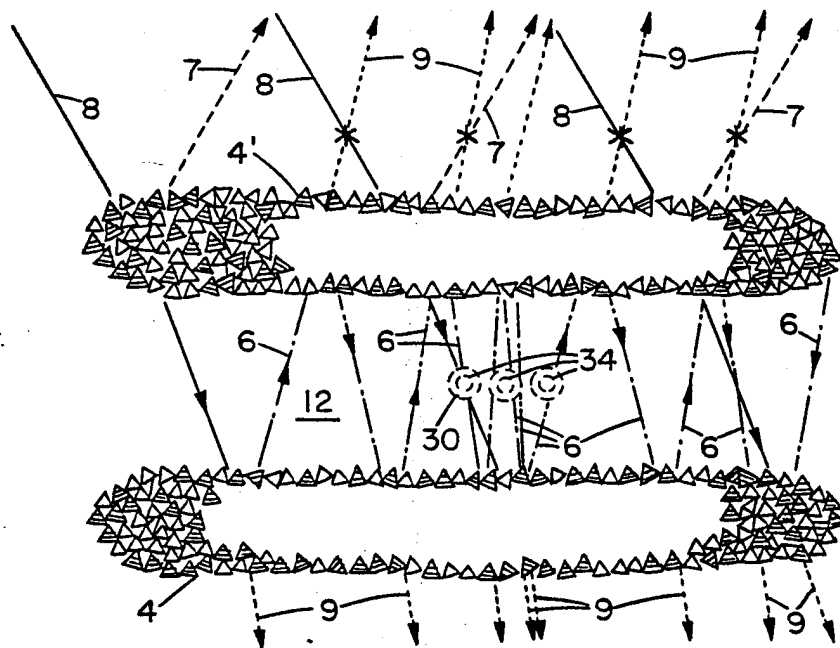
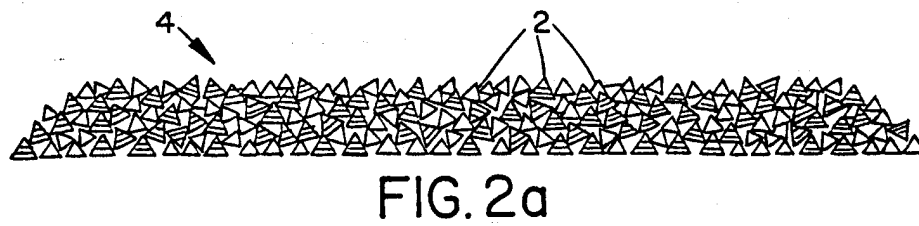
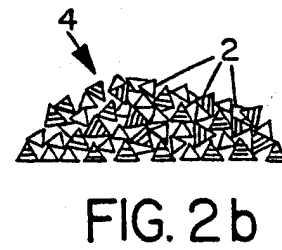
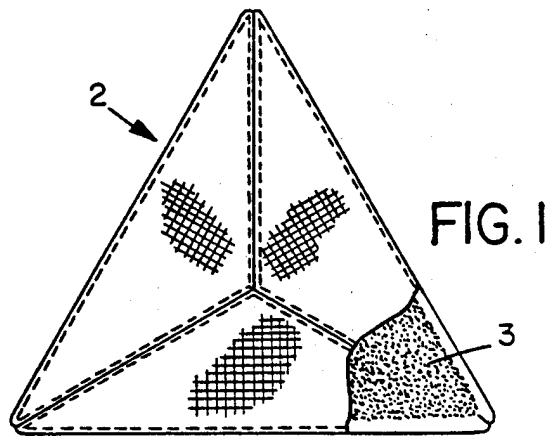


FIG. 3

FIG. 5a

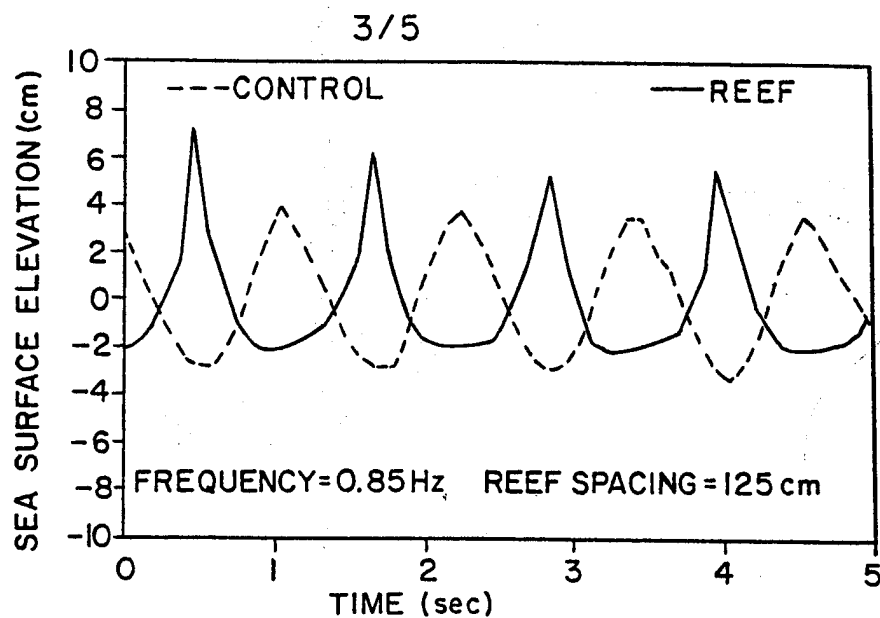


FIG. 5b

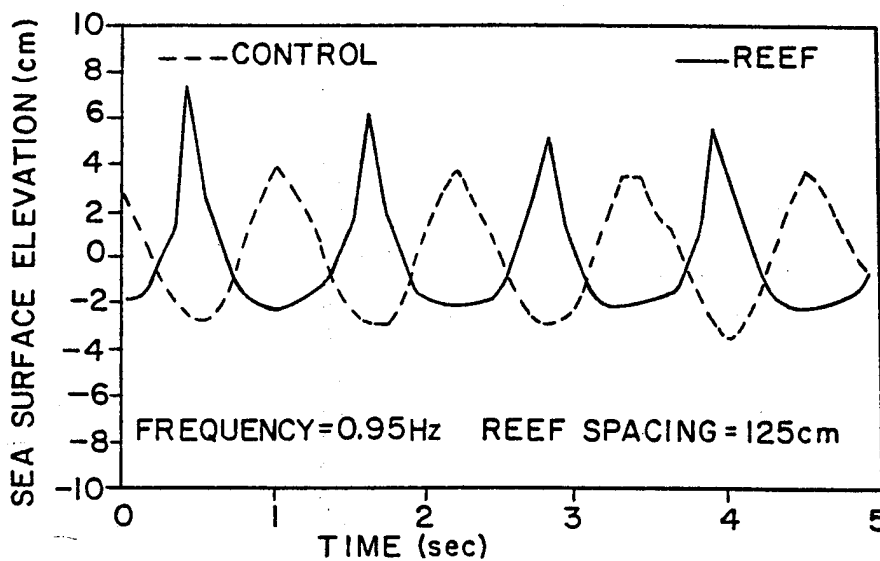
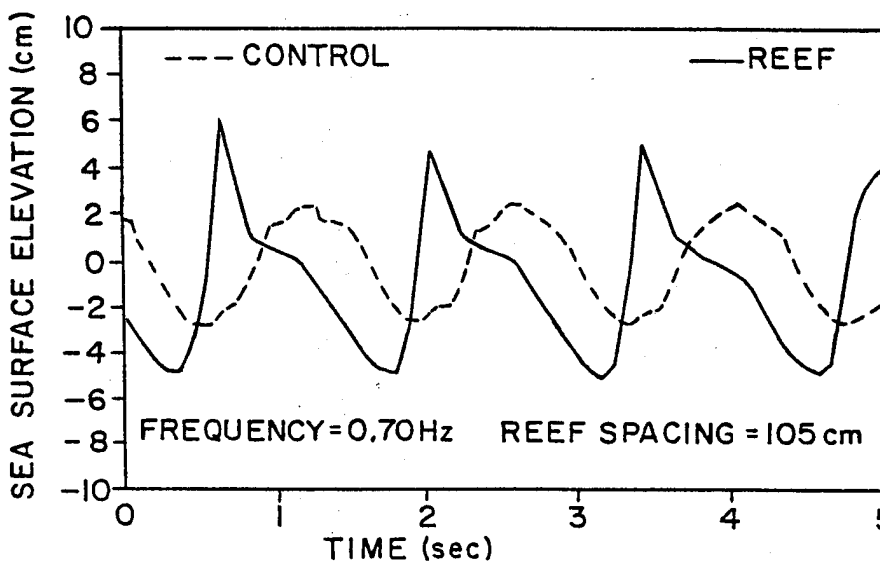


FIG. 5c



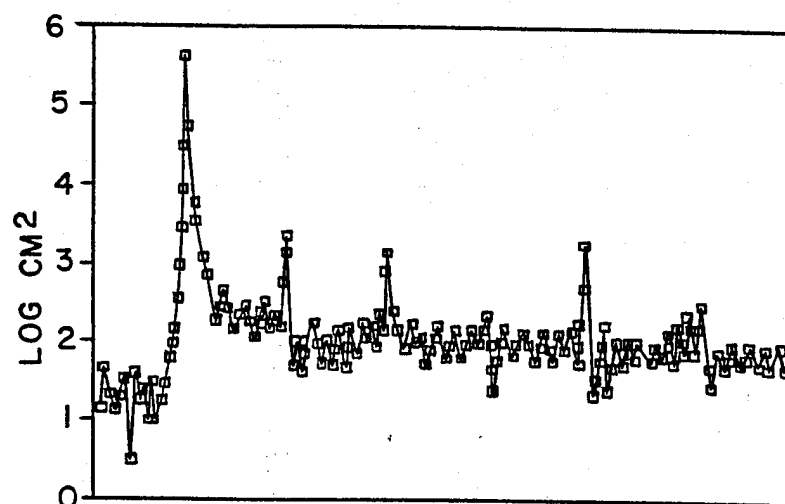


FIG. 6a

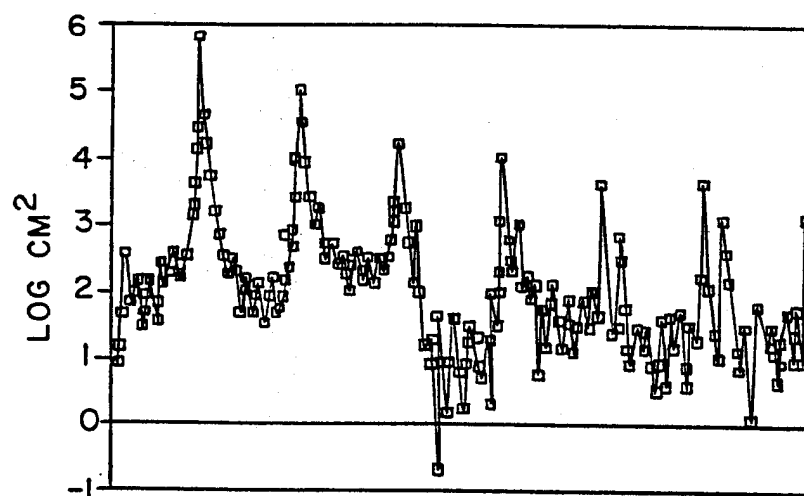
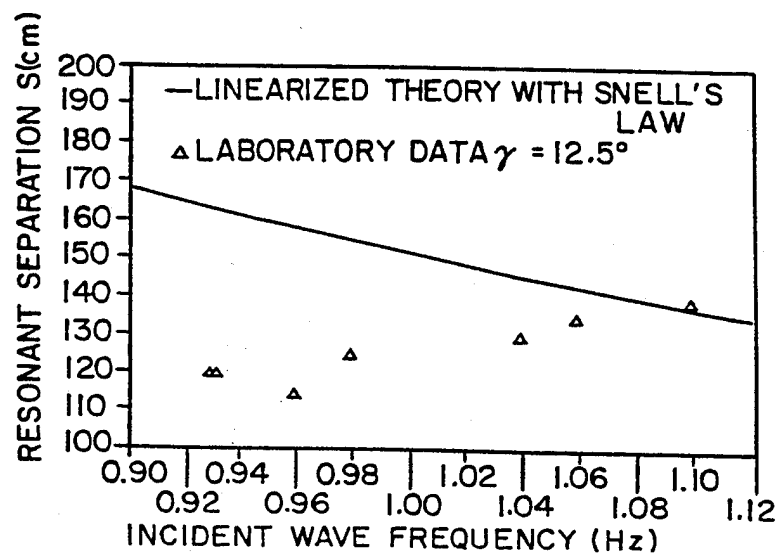
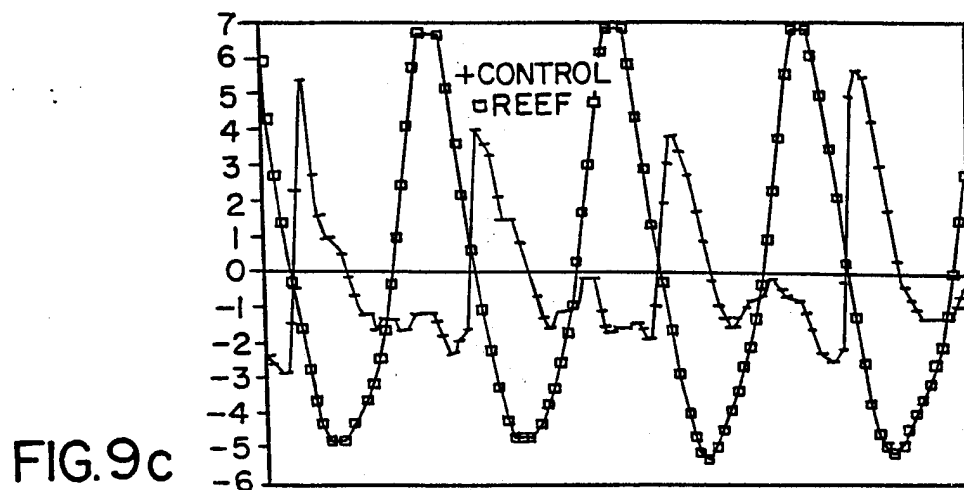
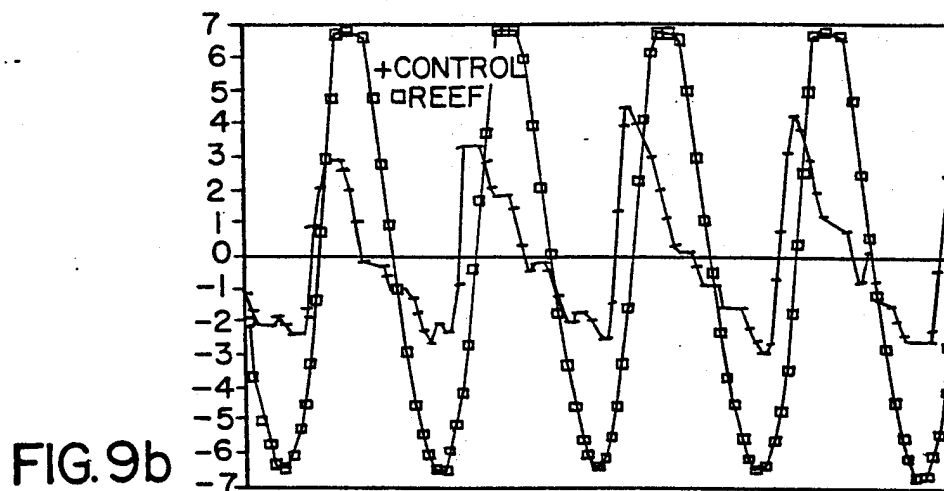
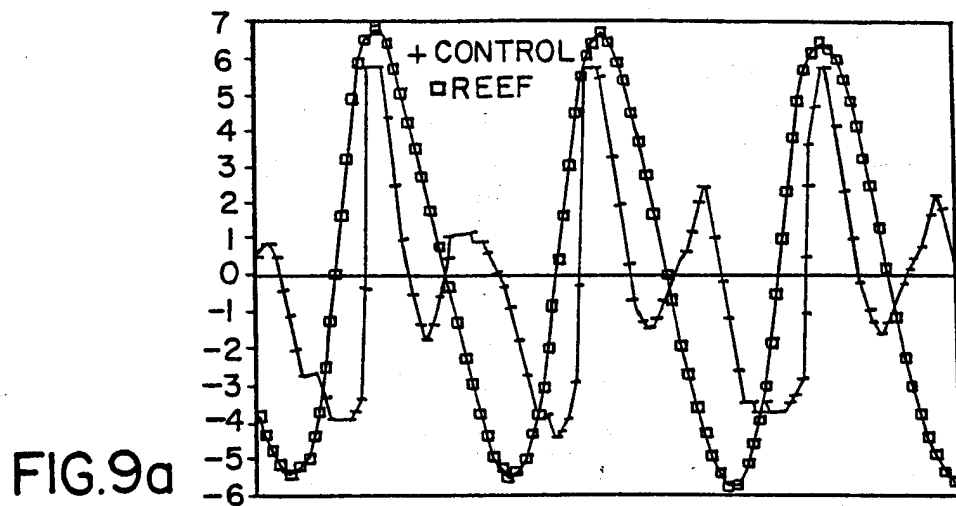


FIG. 6b

FIG. 7



5/5



**APPENDIX F: TEST AND EVALUATION PLAN FOR THE
GLIDING SUBMARINE TACTIC**

by

SCOTT A. JENKINS

UNIVERSITY OF CALIFORNIA, SAN DIEGO

BERKELEY • DAVIS • IRVINE • LOS ANGELES • RIVERSIDE • SAN DIEGO • SAN FRANCISCO



SANTA BARBARA • SANTA CRUZ

CENTER FOR COASTAL STUDIES, A-009
SCRIPPS INSTITUTION OF OCEANOGRAPHY

LA JOLLA, CALIFORNIA 92093-0209

April 11, 1990

Captain Richard W. Mies
COMSUBDEVRON-12
Box 70
Naval Submarine Base New London
Groton, Connecticut 06340

Dear Commodore Mies,

Enclosed please find a copy of the test and evaluation plan for the gliding submarine tactic which we discussed with Admiral Pittenger at the Tactical Oceanography Symposium in Monterey. The plan includes a brief discussion of the concept and its possible application, as well as my thoughts on how to best go about attempting to glide a submarine in the initial sea trials. These thoughts have been based on some discussions I have had with Commander Harold Skelly, USN retired, who is now living in San Diego. The test and evaluation plan also includes some discussion of the optimal glide speeds and crab angles when the tactic is attempted in ocean currents. These optimal calculations are based on a technical paper of mine that will be published shortly in the AIAA Journal of Aircraft. I have included a copy of this paper to assist in further evaluation of the proposed tactic by you and your staff.

I realize that SSN's and SSBN's have not been designed for operation in a gliding mode. No doubt the tactic would be more effective if submarines had somewhat larger dive planes. Nonetheless I was impressed by your willingness to consider an "off-the-wall" idea such as this. Although the first attempts at gliding a submarine may not be altogether successful, I hope enough of a positive result is achieved to encourage further pursuit of this idea. I am willing and eager to contribute further to its evolution, (619) 534-6480.

Sincerely,

A handwritten signature in cursive script, reading "Scott A. Jenkins".

Scott A. Jenkins, Ph.D.
Research Engineer

cc: Rear Admiral Pittenger, OP-96
Dr. Steven Ramberg, ONR, Code 1121

TEST AND EVALUATION PLAN FOR THE GLIDING SUBMARINE TACTIC

prepared by: Dr. Scott A. Jenkins,
Scripps Institution of Oceanography

submitted to: Captain Richard W. Mies COMSUBDEVRON-12
Naval Submarine Base New London
Groton, Connecticut

April 12, 1990

TEST AND EVALUATION PLAN FOR THE GLIDING SUBMARINE TACTIC

TABLE OF CONTENTS:

INTRODUCTION.....	1
CONCEPT.....	1
FIGURE 1, DOLPHIN GLIDE PATH.....	2
FIGURE 2, SINKING GLIDE MODE.....	3
FIGURE 3, RISING GLIDE MODE.....	4
GLIDE POLARS.....	7
GLIDE SLOPE MINIMIZATION.....	9
ACHIEVING STEADY STATE GLIDE.....	11
DOLPHIN GLIDES.....	13
REFERENCES.....	14

THE GLIDING SUBMARINE TACTIC
by Scott A. Jenkins, Ph.D.
Scripps Institution of Oceanography

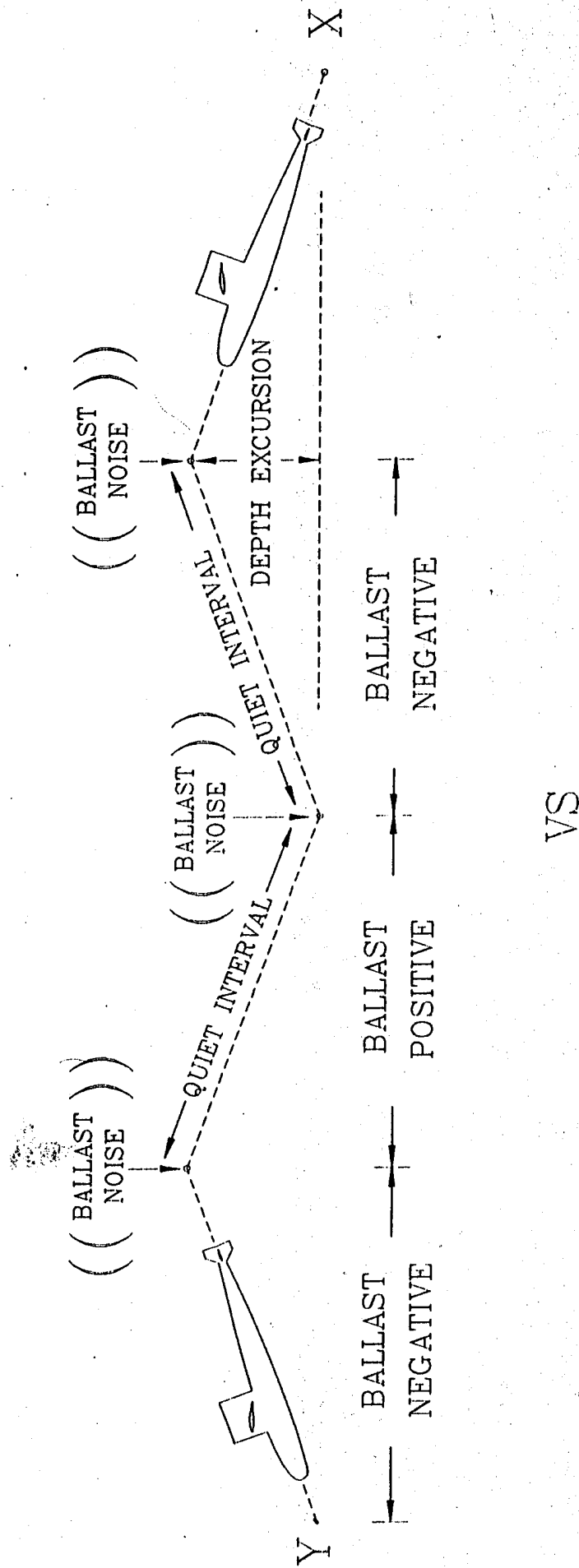
I INTRODUCTION

The purpose of this test and evaluation plan is to explore the feasibility of low speed translation between any two points *without turning the screw*. It is believed that this might be possible by ballasting in a slightly positive or negative state and then gliding on sail-plane lift in the manner of an airplane or bird. The notion here is that passive acoustic detectability can be reduced by trading the continual emittance of hydrodynamic noise from propellor swirl for an occasional "burp" of ballast pump noise as the buoyancy is alternately adjusted between positive and negative states during a dolphin style glide path, see Figure 1. Tactical advantages would likely arise following high speed transits to some patrol area, whence low speed dolphin glides could be invoked to quietly slip away from suspected contact.

II CONCEPT

Two distinct glide modes appear to be possible, a sinking glide as shown in Figure 2 or a rising glide as shown in Figure 3. A steady state sinking glide can probably be achieved by ballasting negatively in a nose down attitude. Similarly a steady state rising glide mode can probably be achieved by ballasting positively in a nose up attitude. In either case the center of buoyancy must be

FIGURE 1: A) DOLPHIN STYLE GLIDE PATH



VS

B) CONTINUOUS SCREW & MACHINERY NOISE

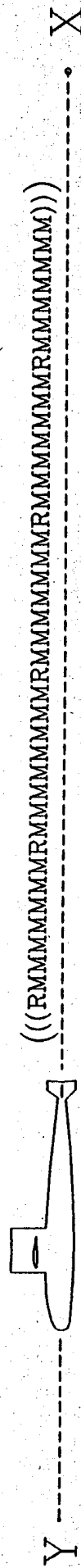
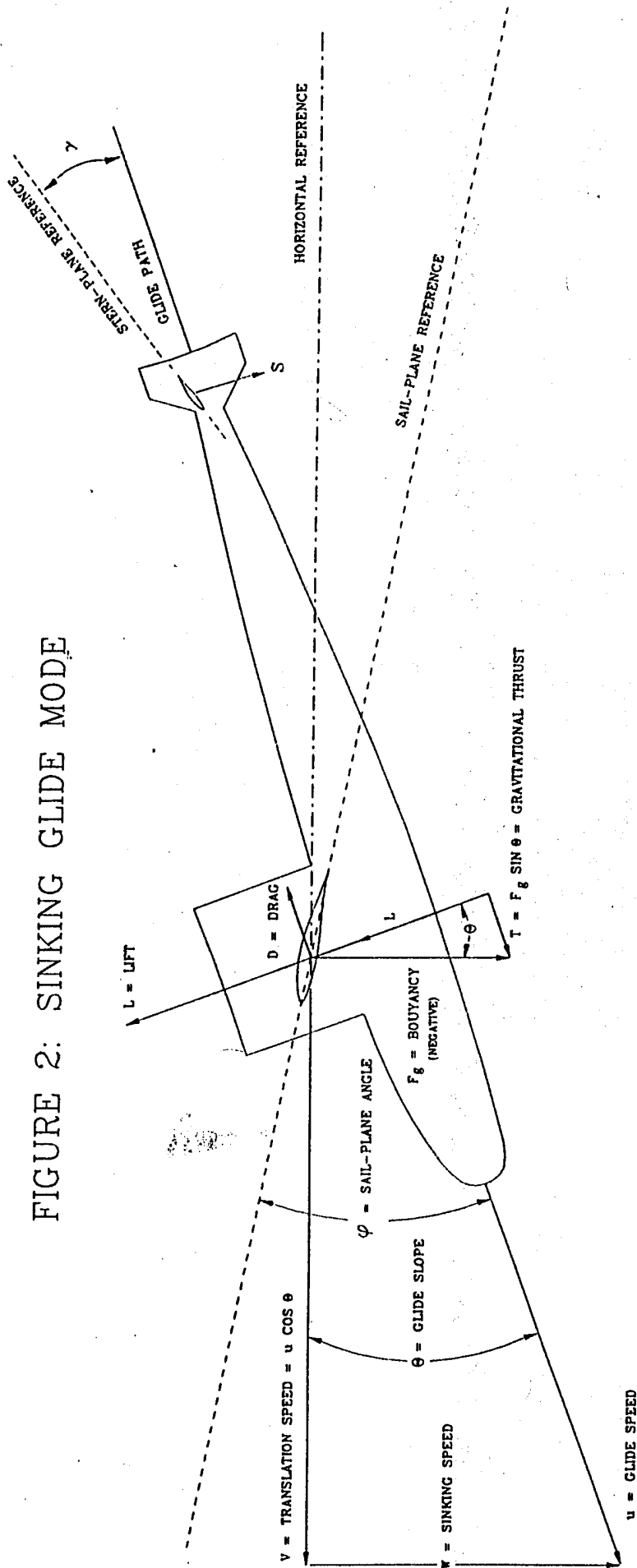
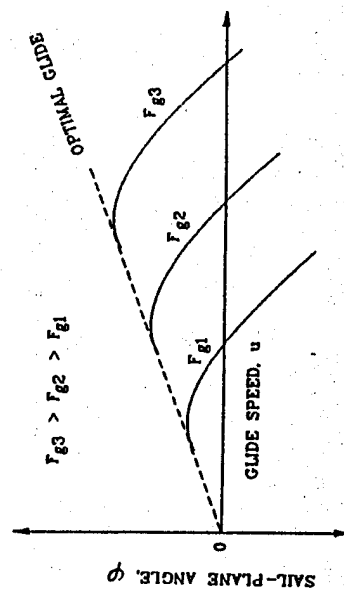


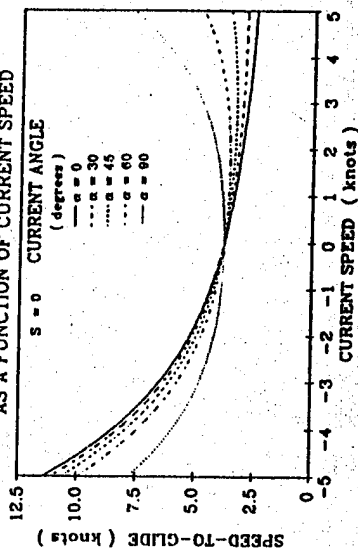
FIGURE 2: SINKING GLIDE MODE



SINKING GLIDE POLAR



HYPOTHETICAL OPTIMAL GLIDE SPEEDS AS A FUNCTION OF CURRENT SPEED



HYPOTHETICAL OPTIMAL CRAB ANGLE AS A FUNCTION OF CURRENT SPEED

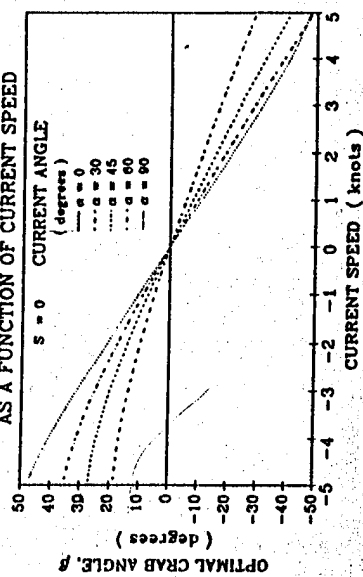
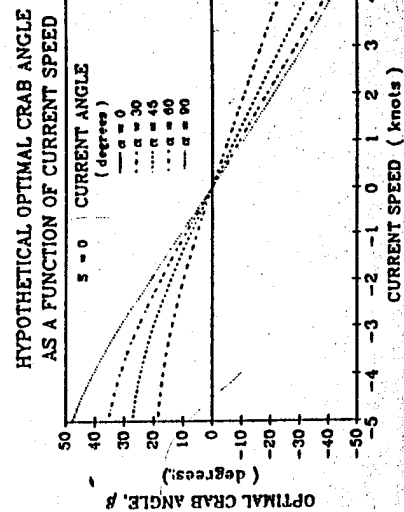
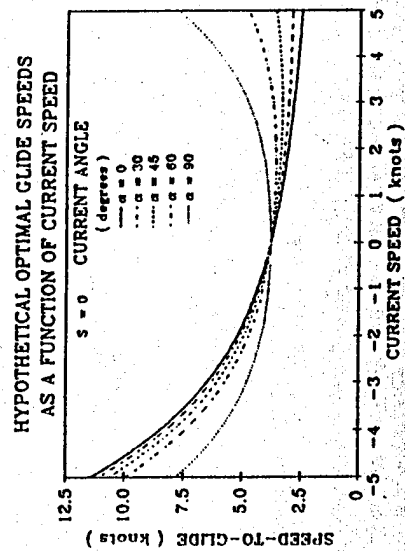
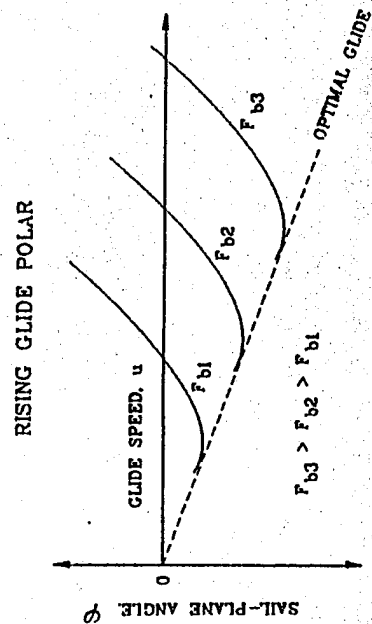
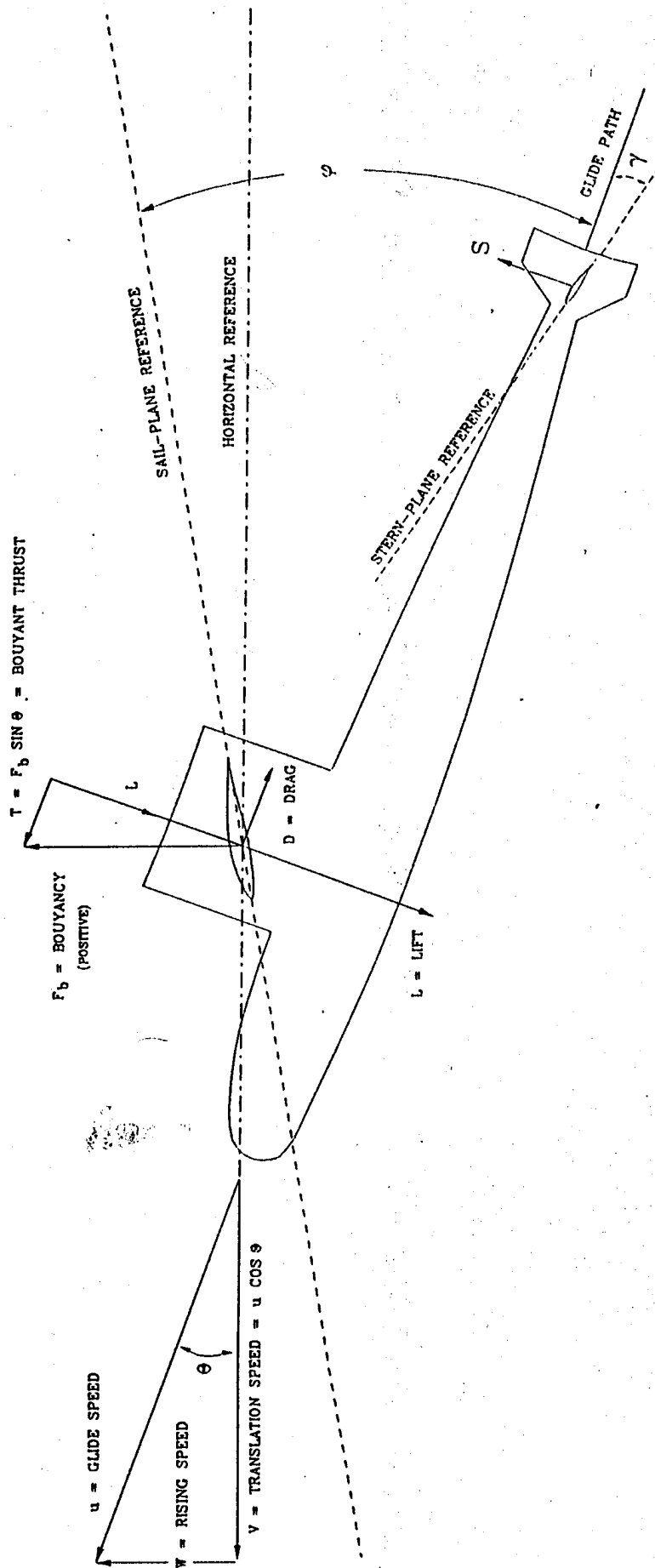


FIGURE 3: RISING GLIDE MODE



moved forward to some point in the neighborhood of the center of pressure on the sail-plane as shown in Figures 2 and 3. The exact vertical position of the center of buoyancy relative to the longitudinal axis of the hull is not particularly critical from the standpoint of gliding dynamics.

Naturally, a submarine ballasted nose heavy as diagrammed in Figure 2 will begin to sink along a trajectory that will continually steepen to a nearly vertical nose down descent. If, however, the sail-planes are adjusted to a positive angle of incidence, $\phi > 0$, then they will generate a lift force, L , acting at right angles to the descent trajectory as shown in Figure 2. The sail-plane lift will prevent the trajectory from becoming vertical. Instead, the trajectory will assume some glide slope, θ , along which the vertical component of the lift force, $L \cos \theta$, balances the gravitational force, F_g , due to the negative buoyancy. The submarine will glide at some speed, u , along this glide slope for which the drag on the submarine, D , exactly balances the gravitational thrust, T , due to the component of negative buoyancy acting along the glide slope, $F_g \sin \theta$. A nose-down pitching moment will result from the dynamic pressure distribution associated with the lift of the sail-planes. This nose-down pitching moment must be corrected by a slight downward trim force, S , exerted by a negative angle of incidence, γ , on the stern-planes. The condition of such a force balance is known as a steady state glide. The

gravitational force due to the negative buoyancy is pulling the submarine down along its glide slope and causing it to translate forward in the process at a speed, $u \cos \theta$.

A similar steady state glide is possible when the submarine is ballasted positively in a nose up attitude as shown in Figure 3. In this case the sail-planes are set at a negative angle of incidence, $\phi < 0$, giving rise to a lift force acting at right angles to the ascent trajectory in the downward direction. This downward oriented lift force prevents the ascent trajectory from becoming vertical and establishes a steady state ascending glide slope along which the vertically downward component of lift, $L \cos \theta$, balances the positive buoyancy, F_b . An upward pitching moment due to the dynamic pressures on the sail-planes must be corrected by a slight upward trim force, S , resulting from a positive angle of incidence, γ , on the stern-planes. When trimmed in this manner, the submarine ascends along a constant glide slope at a glide speed, u , such that the drag on the submarine is balanced by the component of buoyancy acting upward along the glide slope, $F_b \sin \theta$. While the submarine ascends along this rising glide slope, it will translate forward at a speed, $u \cos \theta$.

While translating forward in either the sinking or rising glide mode, the submarine must execute a certain depth excursion. Because depth excursions must remain limited to take advantage of sound ducts, a succession of alternating rising and sinking glides will be necessary in

order to translate over significant distances. This will result in a dolphin style glide path as diagrammed in Figure 1, during which it will be necessary to periodically operate the ballast pumps to reconfigure the buoyancy and trim for alternating rising and sinking glide modes. If a controllable pitch screw is available, it should be feathered to reduce drag and hydrodynamic noise during each glide mode.

III GLIDE POLARS

Consider the sinking glide mode in Figure 2. For any given degree of negative buoyancy, F_{g1} , F_{g2} , F_{g3} , ..., there will be a unique relation between the sail-plane angle or sinking speed and the maximum obtainable steady state glide speed. That relation is known as a glide polar. Each degree of negative buoyancy will have its own specific glide polar. For any given ballast configuration, smaller sail-plane angles will result in higher gliding speeds, but at a cost of greater sinking speeds or greater depth excursions. Conversely the smallest sinking speeds or depth excursions result from the largest sail-plane angles but at a cost of a slower glide speed. The smallest depth excursions and sinking speeds result from the largest sail-plane angle that can be achieved without the sail-planes stalling. Sail-plane stall therefore limits the glide polar at some minimum gliding speed and maximum sail-plane angle setting. Greater degrees of negative buoyancy result in higher glide speeds for any given sail-plane angle. However, the higher glide

speeds resulting from greater negative buoyancy are achieved at a cost of higher sinking speeds or greater depth excursions.

The rising glide mode, Figure 3, also has a family of glide polars associated with it depending upon the degree of positive buoyancy. In this case however larger (less negative) sail-plane angles result in higher gliding speeds. The smallest rising speeds or depth excursions result from the smallest (most negative) sail-plane angles that can be achieved before sail-plane stall ensues. For any given sail-plane angle, the glide speed will be increased by increasing the degree of positive buoyancy, but at a cost of greater rising speeds or depth excursions.

Despite the wealth of design data on SSN's and SSBN's, the glide polars can probably not be calculated exactly. In all likelihood they will have to be measured directly in sea trials. This is due to the fact that the glide polar results from the complex variations of lift and drag with glide speed. Nonetheless the glide polar can probably be represented by a parabola of some sort once the data is obtained because a large portion of the drag is due to profile drag on the hull and induced drag on the dive planes whose general behavior with glide speed is known. Therefore it will not be necessary to measure a glide polar for each particular degree of positive or negative buoyancy. The glide polar measured for a particular ballast configuration

can be used to calculate the glide polars for all other possible ballast configurations.

IV GLIDE SLOPE MINIMIZATION

In an operational scenario one seeks to minimize the numbers of times that the ballast pumps must be operated during a dolphin style glide path between any two points. Therefore, it is desirable to operate at a combination of dive plane angles and glide speeds on the glide polar which minimizes the glide slope in either the rising or sinking mode. These optimal points are shown in Figures 2 and 3 as the optimal glide tangent lines which intersect the glide polars for particular degrees of positive and negative buoyancy. These optimal tangent lines are shown for the case of an ocean with no motion. However in a real ocean with currents, the glide polars become distorted depending on whether the current is acting in the direction of the glide path or at some angle, α , to it. For the general case of rising or sinking glides at some arbitrary angle, α , to the current, there will be an optimal combination of glide speed and crab angle which minimizes the glide slope, rising speed, and depth excursion while maintaining the desired course heading. Some hypothetical calculations of the optimal glide speeds and crab angles are shown in Figures 2 and 3. The curves are calculated for an assumed parabolic glide polar. The algorithms are rather complicated and are based on reference 1. However, the qualitative features of these calculations are perfectly general. For instance, the

optimal glide speed directly into a current ($\alpha = 0$) is faster than for the case of a glide with the current. In order to minimize the glide slope and vertical depth excursions, an 11 knot glide is required directly against a 5 knot current whereas only a 2.5 knot glide is required for gliding along with a 5 knot current. If the glides are performed at $\alpha = 90^\circ$ to the currents, then faster glide speeds are required for higher currents in order to minimize the depth excursions. For glides performed at $\alpha = 45^\circ$ either against or with the current, a sufficiently fast glide speed is required such that the crab angle does not have to exceed 45° in order to maintain the required course heading. Otherwise the submarine is not making adequate progress towards its goal. There are additional corrections to the optimal glide speeds and crab angles when vertical water motions are encountered such as along fronts, eddies and internal waves. These can also be calculated as described in reference 1.

The optimal glide speeds (speed-to-glide) and the optimal crab angles for varying current regimes are all based on the rising and sinking glide polars in still water. In other words, once the glide polar is known, it is possible to make all of the necessary subsequent calculations for glides in a moving ocean. These calculations can be easily summarized in either nomographic tables or on graphs such as those shown in Figures 2 and 3. Adherence to these optimal combinations of glide speeds and

crab angles is necessary to minimize the numbers of times that the ballast pumps must be operated when translating between any two points along a dolphin style glide path.

V ACHIEVING STEADY STATE GLIDE

The first attempt should probably be made by coasting into glide after setting the buoyancy and ballast trim while under power and then stopping the screw. This will ensure sufficient control authority while making the transition from power to glide. If on the other hand the attempt is made from a static condition, then the submarine must either fall or rise from a state of rest and transition through a low speed acceleration during which control authority could be marginal. Furthermore the first attempts to transition from power to glide should be made for the rising glide mode in the event of unforeseen difficulties.

The following sequence of events for the first glide attempts are suggested:

- a) Establish a constant speed under power of 5 knots;
- b) Adjust the ballast while under power for positive buoyancy and nose up trim. (The center of buoyancy must be moved at least as far forward as the mean hydrodynamic center of pressure on the sail-planes. The point at which the sail-planes pivot is sufficiently far forward for this condition.);
- c) Adjust the sail-planes for negative angle of incidence while the ballast is being adjusted for positive buoyancy. Establish a negative sail-plane

angle and positive stern plane angle of incidence sufficient to maintain constant depth once ballasting for positive buoyancy and a forward center of buoyancy has been achieved.

d) Stop and feather the screw. Allow the submarine to decelerate to a constant steady state glide speed.

Adjust the stern-plane trim to some positive angle of incidence sufficient to maintain a constant nose up attitude along the glide slope. The idea here is to keep the nose pointed directly into the flow, and to avoid flying the hull at some angle to the flow. Record the sail-plane angle, the rate of change of depth, and the glide speed.

e) Increase the negative incidence of the sail-planes and the positive incidence of the stern-planes by a small amount. Allow the submarine to decelerate to a new steady state glide speed. Record the sail-plane angle, the rate of change of depth, and the glide speed.

f) Repeat steps d and e in small increments of increasingly negative sail-plane angle and positive stern plane angle until sail-plane stall ensues.

g) Return to the original 5 knot powered configuration. Adjust ballast and trim to the same settings as above. Once the submarine has decelerated to a steady state glide, decrease the degree of negative angle of incidence on the sail-planes. Retrim

the stern planes to fly the hull directly into the flow along the glide slope. Repeat steps e-f for successive reductions in sail-plane angle until unreasonably large ascending glide slopes (greater than 30 or 45°) result.

h) The above procedure will essentially detail the glide polar. If the experiment is performed with little or no current, then the data will be sufficient for following optimization calculations.

Once steady state rising glide modes have been demonstrated, then the above procedures can be followed for ballasting for negative buoyancy and nose down trim. It will be necessary to repeat the above steps for sinking glide modes to determine the sinking glide polar. The sinking glide polar will not necessarily be the exact inverse of the rising glide polar, since the sail-planes atop the sail do not produce the same interference drag effects with the hull for both positive and negative angles of incidence.

VI DOLPHIN GLIDES

Transitions from power to glide while underway should be repeated a sufficient number of times to develop crew proficiency. Once such proficiency is achieved, then transitions from rising glide modes to sinking glide modes can be attempted in order to demonstrate dolphin style gliding over large distances. Initially these transitions should be attempted at fairly high glide speeds and steep glide slopes, in order to insure substantial control

authority. Once dolphin gliding has been proven feasible at relatively inefficient high glide speeds, then the maneuver can be practiced at lower glide speeds and flatter glide slopes for which the tactic will be operationally most effective. Once such dolphin gliding proficiency has been demonstrated, then detailed studies of the acoustic signature during long distance dolphin glides can be undertaken. Such tests should be undertaken only for a pitch controllable screw. The drag and acoustic noise while gliding with an unfeathered screw would likely prove to be prohibitive.

VII REFERENCES

Jenkins, S.A. and J. Wasyl, (in press), "Optimization of skewed glides across lee waves", Journal of Aircraft, AIAA, 20 pp.

**APPENDIX G: OPTIMIZATION OF GLIDES FOR CONSTANT WIND FIELDS
AND COURSE HEADINGS**

by

SCOTT A. JENKINS & JOSEPH WASYL

Optimization of Glides for Constant Wind Fields and Course Headings

S. A. Jenkins and J. Wasyl

Reprinted from

Journal of Aircraft

Volume 27, Number 7, July 1990, Pages 632-638

AMERICAN INSTITUTE OF AERONAUTICS AND ASTRONAUTICS, INC.
370 L'ENFANT PROMENADE, SW • WASHINGTON, DC 20024



Optimization of Glides for Constant Wind Fields and Course Headings

Scott A. Jenkins* and Joseph Wasyl†

University of California at San Diego, La Jolla, California 92093

Theory and experiment are presented for optimal combinations of glide speeds and crab angles that minimize the glide slope at any arbitrary angle to the wind along a constant course heading. The optimization scheme is formulated for constant wind speeds, wind direction, and air mass sink rates. An analytic solution is found in the asymptotic limit of a small crosswind component. A general solution is obtained by seeded iterations with a Taylor series expansion about that limit. The solution was verified in test flights with quartering tailwinds and direct crosswinds at the 700, 500, and 300 mb levels. It was concluded that relatively small pilot-induced speed errors result in significant glide slope degradations with unnecessary and potentially dangerous altitude losses. Applications of the results are considered for wind fields that vary slowly in space, such as lee waves and Rossby waves.

Nomenclature

A_0	= wing area, ft ²
A, B,	
A', B', G	= flight path way points
a, b, c	= glide polar coefficients at altitude
$\hat{a}, \hat{b}, \hat{c}$	= glide polar coefficients at sea level
C_D	= quadratic drag coefficient
$C_{D,i}$	= quadratic induced drag coefficient
$C_{D,p}$	= quadratic profile drag coefficient
C_L	= quadratic lift coefficient
d_n, f_n	= resolvent cubic parameters for iterative general solution
d_0, f_0	= resolvent cubic parameters for weak crosswinds
K_1	= profile drag factor
K_2	= induced drag factor
K_3	= glide polar factor due to profile drag
K_4	= glide polar factor due to induced drag
L/D	= inverse glide slope
L/D_{\max}	= inverse glide slope due to speed to fly
$L/D(u = U + \delta U)$	= inverse glide slope due to speed-to-fly errors
l	= wing cord, n.mi.
m	= gross weight, lb
n	= integral index number
p_n	= second-order coefficient for general iterative case
p_0	= second-order coefficient for weak crosswinds
q_n	= first-order coefficient for general iterative case
q_0	= first-order coefficient for weak crosswinds
R	= Rossby radius of deformation, n.mi.
r_n	= zero-order coefficient for general iterative case
r_0	= zero-order coefficient for weak crosswinds
S	= air mass sink rate, kt
U	= speed-to-fly at altitude, kt
\hat{U}	= speed-to-fly at sea level in still air, kt
U_i	= indicated speed-to-fly, kt
U_n	= general speed-to-fly for n th wind increment, kt
U_0	= speed to fly in weak crosswinds, kt

u	= horizontal component of glide velocity relative to air at altitude, kt
\hat{u}	= horizontal component of glide velocity relative to air at sea level, kt
u_s	= stall speed, kt
v	= wind speed, kt
v_0	= weak wind speed, kt
w	= vertical component of glide velocity relative to air at altitude, relative sinking speed in knots
\hat{w}	= vertical component of glide velocity relative to air at sea level, relative sinking speed in knots
x	= position along flight path relative to any given way point
α	= wind angle relative to course line
β	= crab angle relative to course line
γ	= profile drag exponent
δU	= speed-to-fly error, kt
δv	= wind speed increment, kt
η	= relative squared crosswind velocity difference, kt ²
θ	= minimum glide slope in still air at sea level
λ	= wave length, n.mi.
ρ	= density at altitude, slug/ft ³
$\hat{\rho}$	= density at sea level, slug/ft ³

Introduction

THE first treatment of the problem of the optimal glide speed that minimizes the glide slope in a moving atmosphere was due to MacCready.^{1,2} The solutions have since been referred to as "speed-to-fly." MacCready's original work was valid only for a convective atmosphere in which regions of rising or sinking air translate horizontally with the wind. His speed-to-fly solutions were thus independent of the wind speed and determined uniquely by the rate of vertical air mass movement and the glide polar in still air at sea level.

Subsequently, Kuettner,³ following arguments introduced by Reichmann,⁴ considered the effects on glide slope minimization when regions of rising or sinking air do not translate with the wind over the ground. Such a condition is typically encountered in both hydrostatic and nonhydrostatic lee waves (see Ref. 5). Kuettner considered only the cases of glides directly with the wind. The solutions for speed-to-fly by both Kuettner and Reichmann were graphical in nature, involving tangent plotting for a few selected cases with no mathematics as such presented. Even so, some striking departures from MacCready's original findings were uncovered by both authors. Speed-to-fly was found to be dependent on the wind

Received Dec. 4, 1989; revision received Feb. 13, 1989. Copyright © 1990 by the American Institute of Aeronautics and Astronautics, Inc. All rights reserved.

*Research Engineer and Lecturer, Department of Scripps Institution of Oceanography.

†Development Engineer, Department of Scripps Institution of Oceanography.

speed with the flattest glide slopes achieved for tailwinds at speeds less than the MacCready speed-to-fly. Kuettner also considered the degradation in glide slope at high altitudes with a direct tailwind. He concluded that the practice of ballasting to high wing loadings is disadvantageous since the reduced air density at high altitudes has already effectively raised the wing loading considerably. The increase in relative sinking speeds at these higher wing loadings cannot be compensated in downwind glides because slow speeds-to-fly are required.

In the present paper, the speed-to-fly problem is treated for the general case of glides along constant course headings at an arbitrary angle to the wind for any given altitude. Optimal flight paths for crossing lee waves are shown to result from an orthogonal series of constant course glides. The formulation of the problem is based on a quadratic glide polar in a constant wind field. The constant wind-field assumption provides acceptable accuracy for treating glides in lee waves and Rossby waves, which vary over geophysical length scales. The resulting speed-to-fly equation is, nonetheless, found to be transcendental. An asymptotic analytic solution is found in the limit of small crosswind components. A general solution for arbitrary crosswind components is then developed based on a seeded iteration with a Taylor series expansion about the weak crosswind solution. The results are compared with data from skewed test glides performed between the 700- and 300-mb levels. These comparisons show that speed-to-fly errors can degrade the glide slope to such an extent that the performance gains achieved by modern airfoils and composite construction are lost.

Formulation

Consider glides performed at 1-g load factor across a field of lee waves in such a manner that a constant course heading is maintained between any two arbitrary points (A,B) in an Eulerian frame. Let the course heading connecting (A,B) be at an angle α to the wind whose speed is v as shown in Fig. 1. If the horizontal component of the glide velocity relative to the air is u , then it must be directed at some crab angle β in order to maintain a constant course heading between (A,B). The crab angle is thus given by:

$$\beta = \sin^{-1} [-(v/u) \sin \alpha] \quad (1)$$

While traversing the lee wave field, regions of rising flow (lift) will be encountered along the upwind faces of the lee wave crests, and descending flow (sink) along the downwind faces. Let the vertical velocity component of the air mass be S , which shall be taken as positive in the downward direction in an Eulerian frame. If the vertical component of the glide velocity relative to the air is w (positive downward), then the inverse glide slope (L/D) with respect to an Eulerian frame such as the ground will be

$$L/D = \frac{v \cos \alpha + u \cos \beta}{w + S} = \frac{v \cos \alpha + \sqrt{u^2 - v^2 \sin^2 \alpha}}{w + S} \quad (2)$$

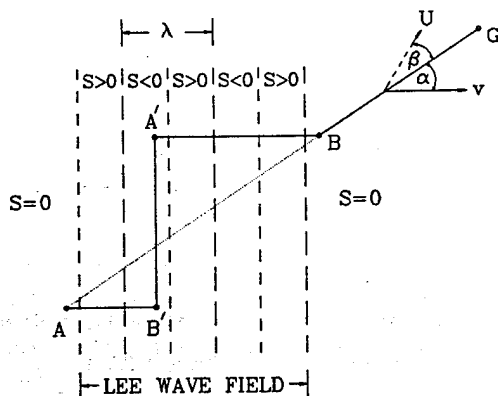


Fig. 1 Schematic of constant course strategies with lee waves.

Any optimal strategy for crossing a field of lee waves is given by one or more glides along constant course headings. This is because the lee wave field structures the air mass sink rates in parallel bands having high cross-stream coherence. Within the lee wave field, an orthogonal series of constant course glides yields the optimum flight path between any two points (A,B) that are separated by some streamwise excursion (see Fig. 1). It is clear from inspection of Eq. (2) that straight line glides with a direct tailwind, $\alpha = 0$, give the maximum possible L/D when entering the lee waves along (A,B') or when traversing the lee wave field along (A',B). These two glides can be joined by a direct crosswind glide at constant course heading, (B',A'), utilizing lee wave lift to achieve an infinite L/D when $S \rightarrow -w$. However, sufficiently long crosswind glides in uninterrupted lift such as (B',A') are not always possible. Variations in the alignment and width of wave generating mountains often destroy the necessary cross-stream coherence of the lee wave field. If the ultimate goal is significantly far downwind, say point G in Fig. 1, then skewed, constant course glides such as (B, G) will become an inevitable part of cross-country strategy.

Before proceeding to optimize any of the constant course glides set forth in Fig. 1, it is desirable to eliminate w from Eq. (2) in order to save labor. The vertical and horizontal components of the glide velocity relative to the air mass are related by the glide polar at sea level in still air. This relation can be posed from the usual assumption that the total drag is a linear combination of profile drag and induced drag:

$$C_D = C_{D,p} + C_{D,i} \quad (3)$$

Because of Reynolds number dependence, the profile drag coefficient is not constant but will vary with the glide velocity in still air at sea level \hat{u} according to

$$C_{D,p} = K_1 \hat{u}^{-\gamma} \quad (4)$$

where K_1 is a factor that varies with the kinematic viscosity and characteristic length scale and γ will depend on the relative proportion of the total wetted surface area that is subjected to laminar vs turbulent boundary layers. The induced drag coefficient on the other hand may be inferred from lifting line theory^{6,7} as

$$C_{D,i} = K_2 C_L^2 \quad (5)$$

where the factor K_2 is a function of wing aspect ratio, twist, taper, and aeroelasticity.

Based upon a drag formulation by Eqs. (3-5), the glide polar at sea level may be written as

$$\hat{w} = (C_D/C_L) \hat{u} = K_3 \hat{u}^{3-\gamma} + (K_4/\hat{u}) \quad (6a)$$

$$K_3 = (\hat{\rho} A_0 K_1)/(2m) \quad (6b)$$

$$K_4 = (2m K_2)/(\hat{\rho} A_0) \quad (6c)$$

If we expand Eqs. (6) in a Taylor series about some optimal speed-to-fly in still air, $\hat{u} = \hat{U}$, then the glide polar is quadratic to second order according to

$$K_3 \hat{u}^{3-\gamma} + (K_4/\hat{u}) - \hat{a} \hat{u}^2 + \hat{b} \hat{u} + \hat{c} \quad (7)$$

where

$$\hat{a} = (3-\gamma)(2-\gamma) K_3 \hat{U}^{1-\gamma} + (2K_4/\hat{U}^3)$$

$$\hat{b} = (3-\gamma) K_3 \hat{U}^{2-\gamma} - (K_4/\hat{U}) - 2\hat{U} \hat{a}$$

$$\hat{c} = K_3 \hat{U}^{3-\gamma} + (K_4/\hat{U}) + \hat{a} \hat{U}^2 - \hat{b} \hat{U}$$

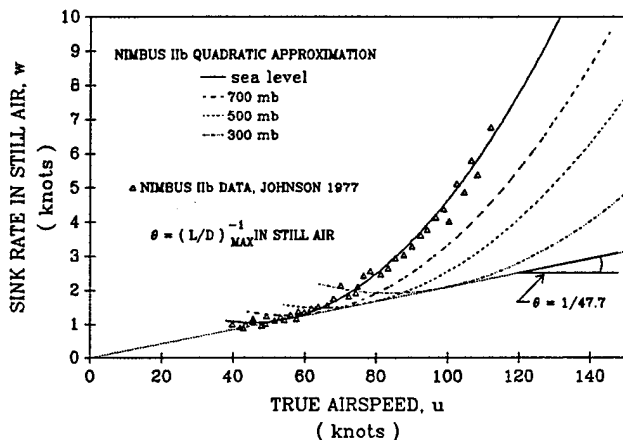


Fig. 2 Quadratic approximation to glide polar data at sea level and at altitude.

Here \hat{a} , \hat{b} , and \hat{c} are based on the air density at sea level. We may then correct the quadratic glide polar in Eq. (7) to any altitude where the air density is ρ by taking

$$w = au^2 + bu + c \quad (8a)$$

$$a = \hat{a} (\hat{\rho}/\rho)^{-1/2} \quad (8b)$$

$$b = \hat{b} \quad (8c)$$

$$c = \hat{c} (\hat{\rho}/\rho)^{1/2} \quad (8d)$$

A comparison is shown in Fig. 2 between the quadratic approximation according to Eq. (7) and measured glide polar data for the test aircraft, a Schempp-Hirth Nimbus IIb, taken from Johnson⁸ and corrected to sea level. The solid curve is a least-squares best fit of a quadratic to the data. The values for the sea level polar coefficients that result from this fit are

$$\hat{a} = 0.0012155 \text{ kt}^{-1} \quad (9a)$$

$$\hat{b} = -0.1106912 \quad (9b)$$

$$\hat{c} = 3.564157 \text{ kt} \quad (9c)$$

Corrected glide polars for the 700-, 500-, and 300-mb altitudes are also shown in Fig. 2 as dashed and dotted curves. Note that the maximum inverse glide slope of 47.7 remains unchanged with altitude for still air. The deformation of the polar at altitude is equivalent to increasing the wing loading by factors of 1.20, 1.42, and 1.84 for the 700-, 500-, and 300-mb levels, respectively.

With Eq. (2) expressed in terms of Eqs. (8), the inverse glide slope is reduced to dependence on four variables, u , v , α , S . Consequently, incremental changes in L/D are expressed as

$$d(L/D) = \frac{\partial(L/D)}{\partial u} du + \frac{\partial(L/D)}{\partial v} dv + \frac{\partial(L/D)}{\partial \alpha} d\alpha + \frac{\partial(L/D)}{\partial S} dS \quad (10)$$

Now, each of the variables in Eq. (10) changes with incremental changes in position along the flight path dx according to characteristic length scales. The air mass sink rates vary over distances comparable to the wave length, $\mathcal{O}(\lambda/2\pi)$, of the lee waves. The wind speed and direction vary over the lowest mode length scales of the upper level storms, typically the Rossby radius of deformation, $\mathcal{O}(R)$, as discussed in Ref. 5. On the other hand, the horizontal component of the glide velocity can vary over distances of only a few cord lengths,

$\mathcal{O}(nl)$, where $n \sim 5$ according to Ref. 9. Therefore, the relative sizes of the terms in Eq. (10) are:

$$\frac{\partial(L/D)}{\partial u} du = \frac{\partial(L/D)}{\partial u} \frac{\partial u}{\partial x} dx = \mathcal{O}\left(\frac{dx}{nl}\right) \quad (11a)$$

$$\frac{\partial(L/D)}{\partial v} dv = \frac{\partial(L/D)}{\partial v} \frac{\partial v}{\partial x} dx = \mathcal{O}\left(\frac{dx}{R}\right) \quad (11b)$$

$$\frac{\partial(L/D)}{\partial \alpha} d\alpha = \frac{\partial(L/D)}{\partial \alpha} \frac{\partial \alpha}{\partial x} dx = \mathcal{O}\left(\frac{dx}{R}\right) \quad (11c)$$

$$\frac{\partial(L/D)}{\partial S} dS = \frac{\partial(L/D)}{\partial S} \frac{\partial S}{\partial x} dx = \mathcal{O}\left(\frac{2\pi dx}{\lambda}\right) \quad (11d)$$

In the atmosphere, $R \sim \mathcal{O}(100 \text{ n.mi.})$, whereas $\lambda \sim \mathcal{O}(10 \text{ n.mi.})$ for hydrostatic lee waves or $\lambda \sim \mathcal{O}(1 \text{ n.mi.})$ for non-hydrostatic lee waves. These are immense compared to the wing cord. Therefore, changes in L/D with respect to wind speed, direction, and air mass sink rate are negligible compared to those with respect to changes in glide speed over any incremental distance dx . Hence, the speed-to-fly U , which maximizes the L/D over the ground, is given to $\mathcal{O}(2\pi nl/\lambda)$ accuracy by

$$\frac{\partial L}{\partial u} \frac{L}{D} = 0 \text{ at } u = U \quad (12)$$

Equation (12) yields the general speed-to-fly equation for glides skewed relative to the wind, which may be written as

$$\begin{aligned} & -aU^3 - 2avU \cos\alpha \sqrt{U^2 - v^2 \sin^2\alpha} \\ & + (c + S + 2av^2 \sin^2\alpha) U - vb \cos\alpha \sqrt{U^2 - v^2 \sin^2\alpha} \\ & + v^2 b \sin^2\alpha = 0 \end{aligned} \quad (13)$$

The transcendental nature of the general speed-to-fly equation [Eq. (13)] follows from the fact that speed-to-fly is a function of the crab angle by way of Eqs. (2) and (12), and crab angle is, in turn, a function of speed-to-fly as required by Eq. (1). Analytic solutions to Eq. (13) arise in the asymptotic limit of an indefinitely small crosswind component, $U^2 \gg v^2 \sin^2\alpha$, for which the speed-to-fly $u = U_0$ is given by

$$U_0^3 + p_0 U_0^2 + q_0 U_0 + r_0 = 0 \quad (14)$$

where

$$p_0 = 2v_0 \cos\alpha$$

$$q_0 = [-(c + S + 2av_0^2 \sin^2\alpha - v_0 b \cos\alpha)/a]$$

$$r_0 = (v_0^2 b \sin^2\alpha/a)$$

$$v_0 = v \ll \sqrt{U_0^2/\sin^2\alpha}$$

The speed-to-fly equation thus collapses to an ordinary cubic equation for weak crosswinds, yielding the following solution:

$$U_0 = \left[-\frac{d_0}{2} + \sqrt{\frac{d_0^2}{4} + \frac{f_0^3}{27}} \right]^{1/3} + \left[-\frac{d_0}{2} - \sqrt{\frac{d_0^2}{4} + \frac{f_0^3}{27}} \right]^{1/3} - \frac{2v_0 \cos\alpha}{3} \quad (15)$$

where

$$d_0 = (1/27)(2p_0^3 - 9p_0 q_0 + 27r_0)$$

$$f_0 = (1/3)(3q_0 - p_0^2)$$

The remaining two roots of Eq. (14) are less than zero (backwards flight) and are therefore not sensible. As a particular case of Eq. (15), the speed-to-fly solution in a direct headwind or tailwind ($\alpha = 0$), which corresponds to the graphical result by tangent plotting due to Kuettner,³ is found to be

$$U_0(\alpha = 0) = (1/2a)[4a^2v^2 + 4a(c + S - bv)]^{1/2} - v \quad (16)$$

For a general solution to Eq. (13), a seeded iteration is begun from the weak crosswind solution U_0 for some small wind speed $v = v_0$. With each iterative step n thereafter, the wind speed is stepped incrementally by $n\delta v$. The numerical computations for any given step n are based on a Taylor series expansion of $(U^2 - v^2 \sin^2 \alpha)^{1/2}$ about the speed-to-fly solution from the previous iteration, $U = U_{n-1}$. By this numerical scheme, the general speed-to-fly equation for the n th iteration is

$$U_n^3 + p_n U_n^2 + q_n U_n + r_n = 0 \quad (17a)$$

where

$$p_n = \frac{\{-vb \cos \alpha [(1/2)\eta^{-1/2} - (1/2)U_{n-1}^2 \eta^{-3/2}] - 2av \cos \alpha (U_{n-1}^3 \eta^{-3/2})\}}{\{-a - av \cos \alpha (\eta^{-1/2} - U_{n-1}^2 \eta^{-3/2})\}} \quad (17b)$$

$$q_n = \frac{\{c + S + 2av^2 \sin^2 \alpha - vb \cos \alpha U_{n-1}^3 \eta^{-3/2} - 2av \cos \alpha [\eta^{1/2} - (1/2)U_{n-1}^2 \eta^{-1/2} - (1/2)U_{n-1}^4 \eta^{-3/2}]\}}{\{-a - av \cos \alpha (\eta^{-1/2} - U_{n-1}^2 \eta^{-3/2})\}} \quad (17c)$$

$$r_n = \frac{\{v^2 b \sin^2 \alpha - vb \cos \alpha [\eta^{1/2} - (1/2)U_{n-1}^2 \eta^{-1/2} - (1/2)U_{n-1}^4 \eta^{-3/2}]\}}{\{-a - av \cos \alpha (\eta^{-1/2} - U_{n-1}^2 \eta^{-3/2})\}} \quad (17d)$$

where $n = 1, 2, 3, \dots$; $\eta = U_{n-1}^2 - v^2 \sin^2 \alpha$; $v = v_0 + n\delta v$. Hence, the general speed-to-fly solution for any given wind speed and arbitrary α is given by

$$U_n = \left[-\frac{d_n}{2} + \sqrt{\frac{d_n^2}{4} + \frac{f_n^3}{27}} \right]^{1/3} + \left[-\frac{d_n}{2} - \sqrt{\frac{d_n^2}{4} + \frac{f_n^3}{27}} \right]^{1/3} - \frac{2v \cos \alpha}{3} \quad (18)$$

where $d_n = (1/27)(2p_n^3 - 9p_n q_n + 27r_n)$; $f_n = (1/3)(3q_n - p_n^2)$; $n = 1, 2, 3, \dots$. Again, the two remaining roots to Eq. (17a) are less than zero and consequently have no physical significance.

Numerical Results

The general speed-to-fly solutions for arbitrary wind speed and direction were computed between the 700- and 300-mb levels by seeded iterations using Eqs. (14-18). The computations were based on an unballasted Nimbus IIb glide polar according to Eqs. (8) and (9). The computational sweeps were stepped in both the positive and negative wind directions using increments of $\delta v = 1.0$ kt. This procedure was selected in preference to some general iterative search routine because the speed-to-fly equation [Eq. (13)] has multiple roots and it was desirable to find cause and effect relationships between speed-to-fly, optimal crab angle, air mass movements, and altitude effects on the glide polar.

The speed-to-fly and optimal crab angle dependence on the wind speed and direction is computed in Fig. 3 for the 700-mb level and in Fig. 4 for the 300-mb level. These computations assume no net vertical motion in the atmosphere, $S = 0$, as would generally be the case during long glides in between wave generating mountains. Negative wind speeds correspond to headwinds, whereas positive values denote tailwinds. Positive crab angles denote deviations from the course line in the same sense as the wind vector (headwinds), whereas negative crab angles deviate from the course line against the wind angle (tailwinds). The fastest and slowest speeds-to-fly arise from glides directly against and with the wind ($\alpha = 0$), respectively. The speed-to-fly in a direct crosswind ($\alpha = 90$ deg) is a sym-

metric function about zero wind speed and is slower than all headwind cases and faster than all tailwind cases. All remaining possible crosswind solutions are intermediate between these two extremes, with small differences among skewed glides into the wind, but significantly faster speeds-to-fly for increasing crosswind components with the wind. When $0 < \alpha < 90$ deg, the maximum inverse glide slopes apparently result from keeping the crab angle small, $\beta < 0$ (45 deg). Hence, the speeds-to-fly during skewed glides with the wind increase with increasing crosswind component in order to maintain the course line without resorting to exceedingly large crab angles.

It is also interesting to note from Figs. 3 and 4 that the indicated speed to fly (based on pitot-static airspeed systems) varies with altitude for any given wind speed and direction. This effect was not considered by MacCready.^{1,2} Generally, slower indicated airspeeds are required at higher altitudes for any nonzero wind speed regardless of direction. Consequently, the indicated speeds-to-fly and crab angles for 60-kt winds at 700-mb are comparable to those required for 90-kt winds at the 300-mb level. The true speeds-to-fly increase with

increasing altitudes but by less than a constant factor $(\bar{p}/\rho)^{1/2}$. This results from the fact that the higher effective wing loading at altitude enables more efficient penetration into a headwind component but requires slower glides at a higher C_L with a tailwind component in order to minimize an already high relative sinking speed.

In Fig. 5, a comparison is made of the maximum possible inverse glide slopes between the 700- and 300-mb levels if exact

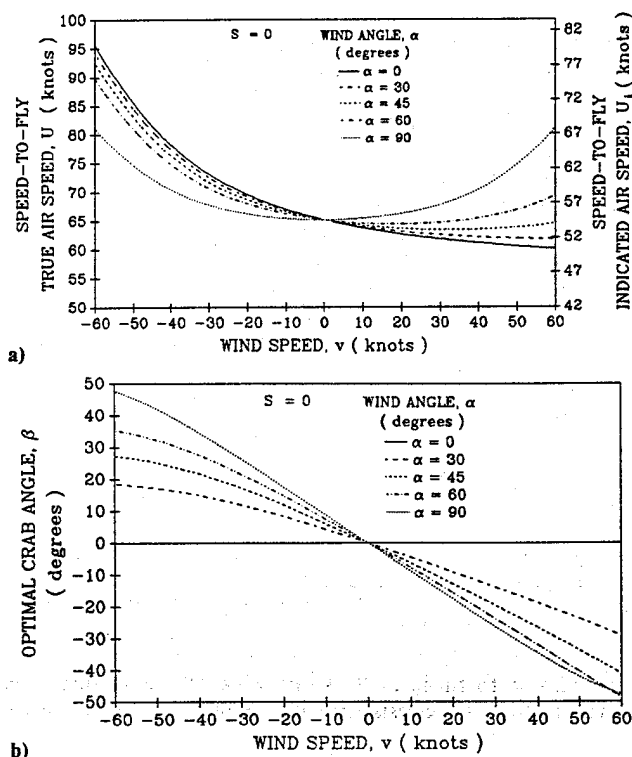


Fig. 3 Speed-to-fly and crab angle vs winds at 700 mb.

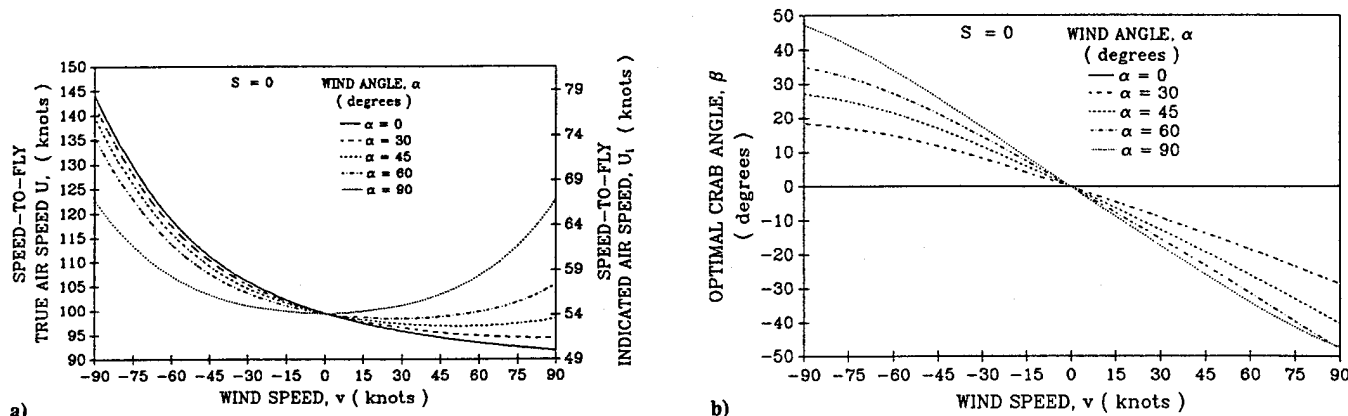


Fig. 4 Speed-to-fly and crab angle vs winds at 300 mb.

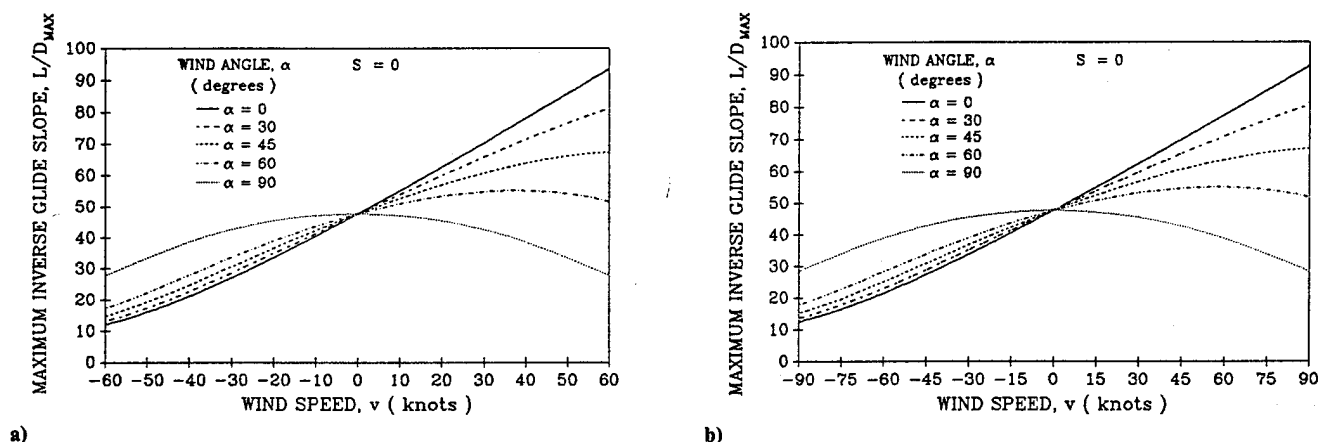


Fig. 5 Maximum inverse glide slopes vs winds at 700 and 300 mb.

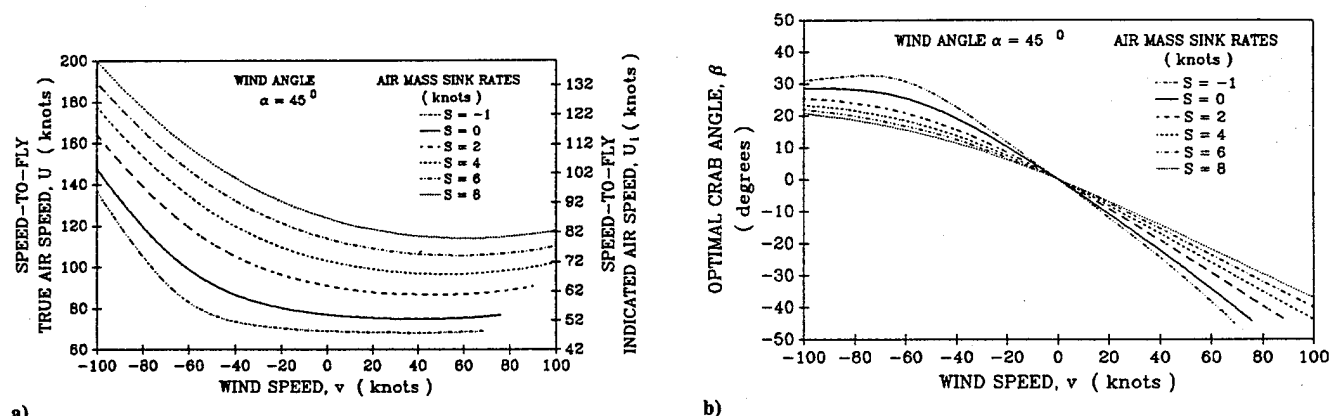


Fig. 6 Speed-to-fly and crab angle vs subsidence in quartering winds.

adherence to speed-to-fly and optimal crab angle is made according to Figs. 3 and 4. A higher L/D is possible into the wind at higher altitudes for any given headwind and direction. Nonetheless, strong headwind conditions clearly should be avoided, as the L/D falls catastrophically from 47.7 in still air to less than 15. Conversely, flatter glide slopes are achieved for any given tailwind and direction at lower altitudes. In a direct crosswind, $\alpha = 90$ deg, it is clearly advantageous to fly at a higher altitude for any given wind speed. Again, the inverse glide slopes for 60-kt winds at 700-mb are found to be comparable to those in 90 kt of wind at the 300-mb level. These features are consistent with the fact that a higher effective wing loading at higher altitudes is an advantage when penetrating into the wind or in strong crosswinds but a disadvantage when gliding slowly at minimum relative sinking

speeds with the wind. Even so, a 90-kt direct tailwind at 300 mb will improve the L/D from 47.7 in still air to 92.7. This value degrades to 65.0 if the 300-mb winds become quartering tailwinds, $\alpha = 45$ deg.

Figure 6 shows computations of speed-to-fly and optimal crab angles for the case of quartering headwinds and tailwinds at the 500-mb level when vertical air mass movements are encountered. Contour plots are shown for particular air mass sink rates of $-1.0 \leq S \leq 8.0$ kt, as would be typically encountered while traversing mountains in fields of lee waves. Computations for an air mass rising faster than the aircraft's minimum relative sinking speed are not possible because a state of perpetual motion is achieved at the start of the seeded iteration, $v = v_0$, for which the problem has not been correctly posed by Eq. (12). The problem in this case becomes one of

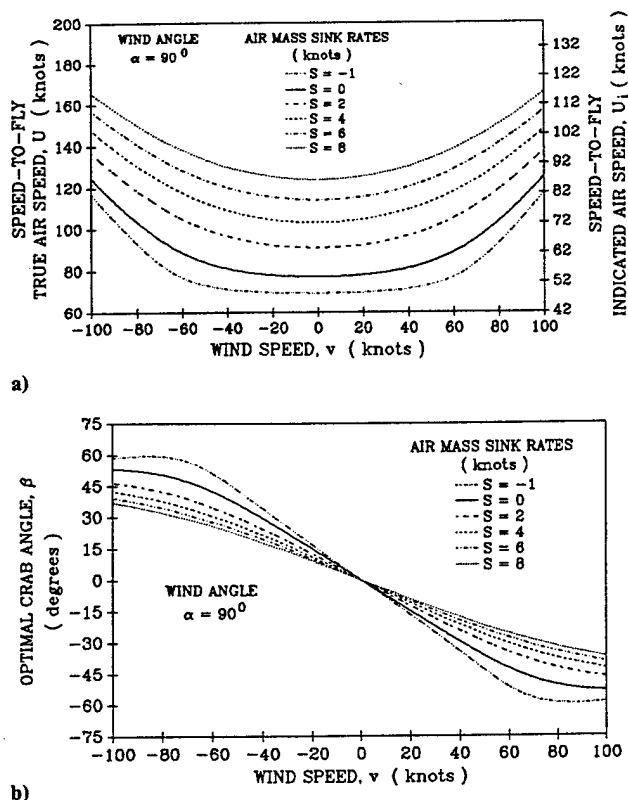


Fig. 7 Speed-to-fly and crab angle vs subsidence in direct crosswinds.

maximizing climb rate for which the speed to fly is $U - u_s$. Otherwise, the speed-to-fly solutions in Fig. 6 require one to speed up in sinking air and to slow down in rising air, similar to MacCready.^{1,2} However, unlike MacCready's original result, the speeds-to-fly for any given air mass sink rate are dependent upon the wind speed, requiring faster glides for a headwind component and slower glides with a tailwind component. Regardless of the air mass sink rate, speeds-to-fly in strong quartering tailwinds tend to increase slightly with increasing wind speed in order to prevent glide slope degradation resulting from large crab angles, $\beta > 0(45 \text{ deg})$. This result is a modification to Kuettner's original downwind strategy (see Ref. 3). In strong quartering headwinds with a rapidly sinking air mass, one finds in Figs. 6 that rather large speeds to fly, $0(200 \text{ kt})$, are required that exceed the structural load limits of the test aircraft. In 1-kt rising air with a quartering tailwind, the speed-to-fly is less than the best L/D speed for still air.

Figure 7 shows the effect of vertical air mass movements on speeds-to-fly and optimal crab angles in direct crosswinds at the 500-mb level. In strong wind with rapidly sinking air, the speeds-to-fly are significantly less than the corresponding quartering headwind cases in Fig. 6 but also significantly greater than the corresponding tailwind cases. For weak direct crosswinds ($v < 30 \text{ kt}$) there is little change in speed to fly with increasing or decreasing wind speed since most of the compensation is done with the crab angle. Unlike all other cases considered, the optimal crab angle for strong direct crosswinds ($v > 60 \text{ kt}$) does indeed exceed 45 deg in nonsinking air.

Figure 8 shows the maximum obtainable inverse glide slopes with vertical air mass motion in quartering headwinds and tailwinds and in direct crosswinds at the 500-mb level. The computations are based on exact adherence to speed to fly and optimal crab angle according to Figs. 6 and 7. One finds that slowly rising air, $S = -1.0 \text{ kt}$, yields impressive L/D for both strong quartering tailwinds ($L/D \approx 190$) as well as weak crosswinds ($L/D \approx 140$). However, strong quartering headwinds degrade the L/D to < 10 regardless of the vertical air mass motions. In fact, the inverse glide slope in this case is almost

as bad for 8 kt of air mass sink as it would be for nonsinking air. The degradation in L/D for strong direct crosswinds is only slightly less. For weak quartering headwinds/tailwinds and direct crosswinds, any rate of sinking of the air mass exerts a pronounced reduction in L/D compared to the case $S = 0$. Most of this performance loss occurs during the first few knots of air mass sink. Very little additional loss occurs for $S \geq 4.0 \text{ kt}$.

Experiment

To ascertain the accuracy of the speed-to-fly and optimal crab angle computations, a series of test flights were conducted with an unballasted Nimbus IIb. The test flights were performed using the active lee wave generating topography of the Laguna Mountains in Southern California. Wave entry was accomplished by aerotow to a point in the neighborhood of the Julian VORTAC. Upon release, climb was initiated to the 500-mb level according to visual flight rules, with additional climbs to the 300-mb level upon receipt of clearance from the Los Angeles Center. After reaching maximum permissible altitude, the test aircraft departed the wave generating region for a series of way points whose exact position was known. The altitude lost in gliding between the way points was recorded by means of a precision barograph and used together with the known distances between way points to calculate the inverse glide slope with respect to the ground. Passage over each way point was determined by visual recognition and annotated on the barograph by executing a rapid dive and recovery maneuver to produce a mark on the trace known as a "notch."

Wind data for the tests were derived from National Weather Service soundings at San Diego, California, and Blythe, Arizona. Test flights were conducted about the 700-, 500-, and 300-mb levels for which sounding data and forecast charts were available. Way points were selected with separations

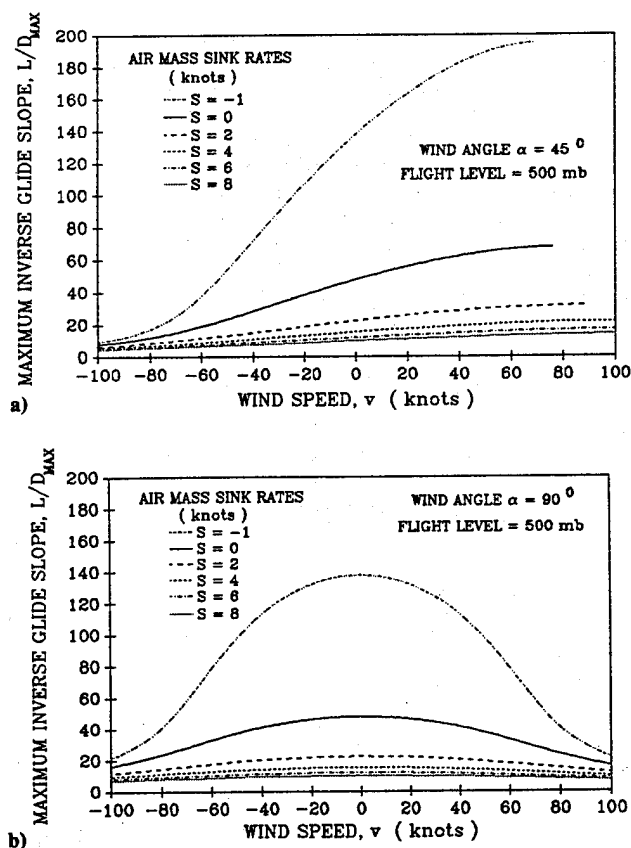


Fig. 8 Maximum inverse glide slopes vs subsidence in quartering and direct crosswinds.

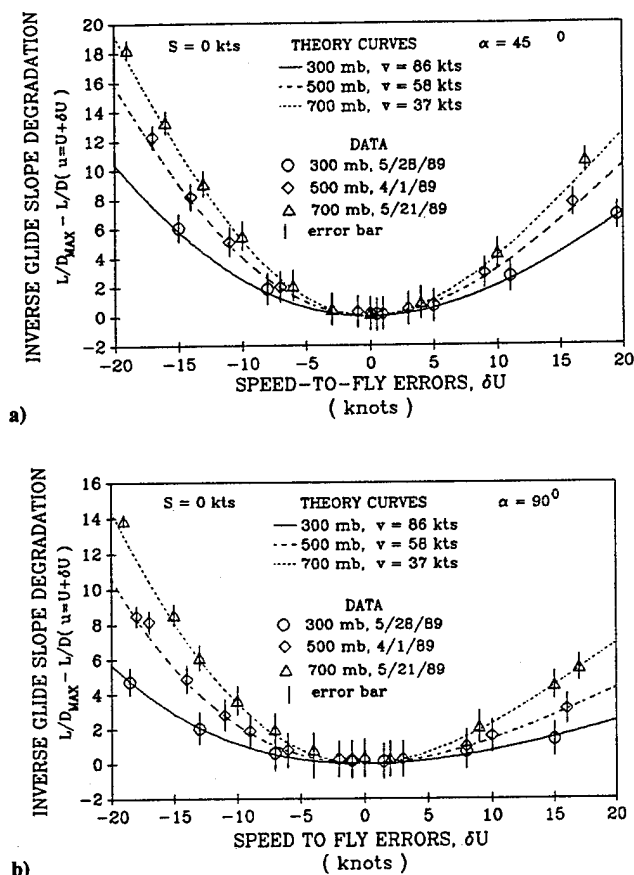


Fig. 9 Effects of speed-to-fly errors in quartering tailwinds and direct crosswinds.

ranging from 11.4 to 37.8 statute miles so that the maximum altitude variance about any one of these levels did not exceed ± 2000 ft. Since the test aircraft lacked accurate positioning equipment, no attempt was made to test speed-to-fly theories within the variable vertical velocities of the lee wave field. Instead, the way points were selected upwind of the wave generating topography to test the direct crosswind calculations and a considerable distance downwind of the wave generating topography for quartering tailwind tests. This arrangement was aided by the fact that the lee waves were generated over a broad tilted plateau and were, therefore, essentially hydrostatic in nature with vertically upward propagation and no secondary or tertiary phases downwind (see Ref. 5).

Figure 9 shows the results of these tests during which known speed-to-fly errors δU were flown to yield measured inverse glide slopes $L/D(u = U + \delta U)$. The speed-to-fly errors are corrected for the airspeed system errors measured by Johnson.⁸ In every case for which a nonzero speed-to-fly error was flown, the resulting inverse glide slopes are found to be less than the theoretical maximum L/D_{\max} when exact adherence to speed-to-fly and optimal crab angle is maintained. The curves in Fig. 9 are generated by a numerical search about either side of the speed-to-fly solutions computed from Eqs. (14-18) for the respective altitudes and winds. The particular wind speeds for those computations are selected in between

the San Diego and Blythe soundings based on a minimization of the variance between the data and resulting theory curves. A check of the L/D_{\max} values is provided by the data points gathered for zero speed-to-fly errors. The loss in L/D due to any given speed-to-fly error is greater at lower altitudes for both quartering tailwinds and direct crosswinds. Furthermore, flying too slowly produces a greater degradation in L/D than flying too fast. Speed-to-fly errors have a greater adverse impact in quartering tailwinds than in direct crosswinds. However, in either case, the speed-to-fly errors resulting from flying too slowly can diminish the clock on aerodynamic design back by as much as 50 years. In other words, pilotage must be considered a leading-order process.

Conclusions

- 1) Speed-to-fly during glides skewed relative to the wind by less than 90 deg requires flying faster through sinking air or into a headwind component and flying slower through rising air or with a tailwind component such that the crab angle does not become excessively large, $\beta < \Theta(45 \text{ deg})$.
- 2) Speed-to-fly in direct crosswinds requires flying faster through sinking air or with increasing wind speed and flying slower through rising air or with decreasing wind speed, using crab angles that may exceed 45 deg for the case of strong winds in a nonsinking air mass.
- 3) Maximum L/D with any given tailwind component is achieved at lower altitudes.
- 4) Maximum L/D with any given headwind component or any given direct crosswind is achieved at higher altitudes.
- 5) Speed-to-fly errors resulting from flying too slowly yield the greatest losses in L/D .
- 6) Losses in L/D for any given speed-to-fly error are greater at lower altitudes.

Acknowledgments

This work was partially supported by a grant from the Office of Naval Research, Code 1121. The authors are grateful for the thoughtful criticisms provided by the reviewers, which led to the formulation of Fig. 1.

References

- ¹MacCready, P. B., "Optimum Airspeed Selector," *Soaring*, Vol. 18, No. 2, 1954, pp. 16-21.
- ²MacCready, P. B., "Understanding Speed-to-Fly and the Speed Ring," *Soaring*, Vol. 47, No. 5, 1982, pp. 42-47.
- ³Kuettner, J. P., "The 2000 Kilometer Wave Flight-Part II," *Soaring*, Vol. 49, No. 3, 1985, pp. 22-27.
- ⁴Reichmann, H., *Cross-Country Soaring*, Thomson, Pacific Palisades, CA, 1978, p. 98.
- ⁵Gill, A. E., *Atmosphere—Ocean Dynamics*, Academic, Orlando, FL, 1982, pp. 274-294.
- ⁶Prandtl, L., *Abriss der Stromungslehre*, Vieweg, Braunschweig, FRG, 1931, p. 189.
- ⁷Van Dyke, M., "Lifting Line Theory as a Singular-Perturbation Problem," *Journal of Applied Mathematics and Mechanics*, Vol. 28, 1964, pp. 90-101.
- ⁸Johnson, R. H., "Flight Test Polar Measurements of Modern Sailplanes," *Technical Soaring*, Vol. 4, No. 4, 1977, pp. 13-27.
- ⁹Basu, B. C., and Hancock, G. J., "The Unsteady Motion of a Two-Dimensional Aerofoil in Incompressible Inviscid Flow," *Journal of Fluid Mechanics*, Vol. 87, No. 1, 1978, pp. 159-178.